

The Pennsylvania State University

The Graduate School

**BUBBLE TRAPPING IN TWO-PHASE WAKES FROM A LIQUID-GAS FLOW
AROUND A CYLINDER**

A Dissertation in
Mechanical Engineering

by

Dohwan Kim

© 2022 Dohwan Kim

Submitted in Partial Fulfillment
of the Requirements
for the Degree of

Doctor of Philosophy

December 2022

The dissertation of Dohwan Kim was reviewed and approved by the following:

Matthew J. Rau
Assistant Professor of Mechanical & Aerospace Engineering
The George Washington University
Dissertation Advisor
Chair of Committee

Stephen P. Lynch
Associate Professor of Mechanical Engineering

Alexander S. Rattner
Dorothy Quiggle Career Development Professor of Mechanical Engineering

Fan-Bill B. Cheung
George L. Guillet Professor of Mechanical Engineering

Ali Borhan
Professor of Chemical Engineering

Daniel C. Haworth
Associate Department Head for Graduate Programs
Department of Mechanical Engineering

ABSTRACT

Small tubes and fins have long been used as methods to increase surface area for convective heat transfer in single-phase flow applications. As demands for high heat transfer effectiveness have increased, implementing evaporative phase-change heat transfer in conjunction with these methods to increase surface area in advanced heat exchanger and heat sink designs has become increasingly attractive. However, the complex two-phase flow that results from these configurations is poorly understood, particularly in how the gas phase interacts with the flow structure of the wake created by these bluff bodies. This experimental research was conducted to understand the bubbles in a liquid-gas around a cylinder interact with the flow structure.

In Chapter 2, a vertical water channel was developed to conduct an experimental study of liquid-gas flow around the cylinder. The bubbly flow movement around the cylinder was visualized with a high-speed camera and varying liquid Reynolds numbers from $Re = 99$ and $Re = 2,956$ and air superficial velocities varied from $j_g = 0.06$ m/s to $j_g = 0.60$ m/s. The mean bubble diameter observed during the experiment varied from 0.5 mm to 3.5 mm. Time-averaged images were examined to calculate the local void fraction values in the two-phase wake. A liquid-phase region with characteristically low void fractions and a bubble-trapping region with characteristically high void fractions could be easily determined by calculating the ratio between local void fraction values in the wakes and the freestream void fraction values. The liquid-phase region occurred throughout the experimental investigations when the Reynolds number was varied from $Re = 99$ to $Re = 2,956$. The overall length of the liquid-phase region decreased with increasing Reynolds number as the bubble-trapping region appeared when the Reynolds number was greater than 2,000. However, the bubble-trapping region also occurred at a lower Reynolds number of $Re = 1,182$ when the mean bubble diameter was reduced from 3.5 mm to 0.5 mm.

In Chapter 3, a force balance model was developed to explain the occurrence of the bubble-trapping region. The high-speed images collected from the experimental facility were processed to detect the air bubbles and calculate their trajectories using particle tracking velocimetry and particle image velocimetry algorithms. In addition to the bubble velocities, the liquid velocities were also calculated by tracking the movement of bubbles and neutrally-buoyant flow tracers from the high-speed images using particle image shadow velocimetry. The phase-resolved velocities confirmed the formation of the bubble-trapping region behind the cylinder, where air bubbles were concentrated in the cylinder wake. To explain the bubble movement in the two-phase wakes, a time-averaged force balance equation was derived. The force balance equation and the phase-resolved velocity results revealed that strong inertial and lift forces were present when the Reynolds number was greater than 2,000. In addition, the reduced-order force balance analysis suggested that the bubble-trapping occurred at a lower Reynolds number of $Re = 1,182$ with a mean diameter of 0.5 mm due to a strong lift force acting on the small air bubbles despite the relatively weak inertial forces.

In Chapter 4, further visualization of bubbly flow movement with the flow tracers was conducted by focusing Reynolds number from $Re = 493$ to $Re = 2,463$ at an air superficial velocity of $j_g = 0.36$ m/s to explain the importance of the lift force on the bubble-trapping region at a transitional Reynolds number. The result from the flow measurements revealed that the bubble-trapping forces are composed in horizontal and vertical directions. The horizontal component of the inertial and lift forces attracted bubbles toward the centerline of the water channel; the vertical component of the inertial and lift forces pulled the air bubbles downward to hold them in the bubble-trapping region. The analysis discovered that the bubble-trapping forces act in two distinct locations based on their direction. Bubbles traveling around the cylinder faced strong horizontal forces at a downstream location of $y/D = 1.0$, which induced the bubble movement towards the centerline. Then, the bubbles faced strong vertical forces at a downstream

location of $y/D = 1.5$, slowing down their vertical velocity and remaining them in the bubble-trapping region momentarily. In addition, the force balance analysis showed that lift forces also played a significant role in the formation of the bubble-trapping region. The lift force on the bubbles was also present in the horizontal and vertical directions; however, it was more important for explaining the bubble motion in the horizontal direction. Additionally, the comparison of liquid velocities in the two-phase and single-phase crossflows was made at $Re = 2,946$ to determine the effects of air bubbles in the flow. The transient analysis showed that the flow around the cylinder could be periodic; however, the velocity measurements are suitable for the time-average force balance analysis. It also revealed that the injection of air bubbles increased the mean and fluctuating liquid velocities in the wakes.

TABLE OF CONTENTS

LIST OF FIGURES	viii
LIST OF TABLES.....	xi
ACKNOWLEDGEMENTS.....	xii
1. Introduction.....	1
1.1 Background	1
1.2 Bluff Bodies in a Single-Phase Crossflow	5
1.3 Bluff Bodies in a Two-Phase Crossflow	9
1.3.1 Bubble-Trapping Region.....	10
1.3.2 Preferential Concentration.....	14
1.3.3 Bubble Trapping Forces	16
2. Characterization of Two-Phase Wakes in an Upward Liquid-Gas Flow around a Cylinder.....	19
2.1 Method	20
2.1.1 Experimental Apparatus	20
2.1.2 Experimental Conditions.....	21
2.1.3 Image Acquisition and Processing	23
2.2 Result	28
2.2.1 Shadow Fraction and Void Fraction.....	28
2.2.2 Liquid-Phase Region	31
2.2.3 Bubble-Trapping Region.....	34
2.3 Discussion and conclusion	38
3. Explaining the Physics of the Bubble-Trapping Region.....	40
3.1 Method	41
3.1.1 Image Acquisition and Processing	41
3.2 Result	49
3.2.1 Void Fraction Ratio.....	49
3.2.2 Air Velocities in the Wakes	51
3.2.3 Liquid Velocities in the Wakes	54
3.3 Discussion	56
3.3.1 Force Balance Equation	56
3.3.2 Analysis of Bubble Trapping	59
3.3.3 Bubble Trapping Parameter	61
3.4 Conclusion	64

4. Transitional Behavior of the Bubble-Trapping Region and Transient Analysis on the Two-Phase Wakes.....	65
4.1 Method	66
4.2 Result	68
4.2.1 Void Fraction Ratio	68
4.2.2 Air Velocities in the Wakes	70
4.2.3 Liquid Velocities in the Wakes	72
4.3 Discussion	74
4.3.1 Bubble-Trapping Forces.....	74
4.3.2 Transient Analysis on Wakes.....	81
4.4 Conclusion	84
5. Conclusions and Recommendations	86
Bibliography	91

LIST OF FIGURES

Figure 1-1. Boundary layer formation and separation of flow on a single-phase flow around a cylinder. [3].....	5
Figure 1-2. Photographs of upward two-phase wakes around a cylinder, where $\overline{U_{0,TP}}$ is the mean flow velocity, d is the cylinder diameter, and $\overline{\alpha_0}$ is the mean void fraction [29]. In these photographs, liquid is bright and the bubbles and cylinders appear dark.	8
Figure 1-3. An example of static pressure distributions for single-phase flow (left) and two-phase flow (right) [29].	11
Figure 1-4. A sketch of a two-stream planer mixing layer for simulating bubble trapping. [49].....	16
Figure 2-1: Illustration of experimental facility: (a) flow chart, (b) test section and its field of view.	19
Figure 2-2: Raw photographs of the wake around the cylinder ($Re = 1,182, j_g = 0.06$ m/s) for (a) the 3.5 mm bubbles and (b) the 0.53 mm bubbles.	23
Figure 2-3: Shadow fraction images for $j_g = 0.36$ m/s with the 3.5 mm bubbles at liquid Reynolds numbers of (a) $Re = 99$ (b) $Re = 197$ (c) $Re = 1,182$ (d) $Re = 2,069$ (e) $Re = 2,956$ and for $j_g = 0.06$ m/s with the 0.53 mm bubbles at liquid Reynolds numbers of (f) $Re = 296$ (g) $Re = 591$ (h) $Re = 1,182$ (i) $Re = 2,069$ and (j) $Re = 2,956$	24
Figure 2-4: Freestream values of (a) shadow fraction and (b) void fraction after applying the correlation, plotted as a function of air superficial velocity and liquid Reynolds number.	26
Figure 2-5: Contour plots of void fraction ratio (α/α_∞) at $j_g = 0.36$ m/s for the 3.5 mm bubbles at liquid Reynolds numbers of (a) $Re = 99$ (b) $Re = 197$ (c) $Re = 1,182$ (d) $Re = 2,069$ and (e) $Re = 2,956$ and at $j_g = 0.06$ m/s for the 0.53 mm bubbles at liquid Reynolds numbers of (f) $Re = 296$ (g) $Re = 591$ (h) $Re = 1,182$ (i) $Re = 2,069$ and (j) $Re = 2,956$	29
Figure 2-6: Liquid-phase region contours behind the cylinder with the 3.5 mm bubbles for (a) $j_g = 0.06$ m/s, (b) $j_g = 0.18$ m/s, (c) $j_g = 0.36$ m/s, (d) $j_g = 0.60$ m/s; (e) with the 0.53 mm bubbles for $j_g = 0.06$ m/s, and (f) with the 0.48 mm bubbles for $j_g = 0.06$ m/s.....	31
Figure 2-7: Length of the liquid-phase region as a function of Reynolds number for all air superficial velocities and bubble sizes.	32

Figure 2-8: Contours showing the bubble trapping region behind the cylinder for the 3.5 mm bubbles and (a) $j_g = 0.06$ m/s, (b) $j_g = 0.18$ m/s, (c) $j_g = 0.36$ m/s, (d) $j_g = 0.60$ m/s, (e) the 0.53 mm bubbles and $j_g = 0.06$ m/s, and (f) the 0.48 mm bubbles and $j_g = 0.06$ m/s.....	33
Figure 2-9: The downstream location of a maximum void fraction within the bubble-trapping region as a function of Reynolds number for all air superficial velocities and bubble sizes.	35
Figure 2-10: Void fraction ratio at a downstream location of $y/D = 1.5$ for the 3.5 mm bubbles and (a) $j_g = 0.06$ m/s, (b) $j_g = 0.18$ m/s, (c) $j_g = 0.36$ m/s, (d) $j_g = 0.60$ m/s, (e) the 0.53 mm bubbles and $j_g = 0.06$ m/s, and (f) the 0.48 mm bubbles and $j_g = 0.06$ m/s.....	36
Figure 3-1: Representation of imaging process: (a) raw images, (b) pre-processed images with background removal, (c) solitary bubble images, (d) cluster bubble images, (e) processed images, and (f) watershed transformation for cluster bubble images.....	41
Figure 3-2: Bubble size distribution of images for air bubbles in solitary (Figure 3-1(c)), cluster (Figure 3-1(d)), and watershed (Figure 3-1(f)) when $Re = 99$ and $j_g = 0.18$ m/s.....	44
Figure 3-3: Image processing procedure for PIV measurements to determine small bubble velocities.	45
Figure 3-4: Contour plots of the void fraction ratio behind the cylinder at $j_g = 0.36$ m/s with the 3.5 mm bubbles for (a) $Re = 99$ (b) $Re = 197$ (c) $Re = 1,182$ (d) $Re = 2,069$ and (e) $Re = 2,956$ and at $j_g = 0.06$ m/s with the 0.53 mm bubbles for (f) $Re = 296$ (g) $Re = 591$ (h) $Re = 1182$ (i) $Re = 2069$ and (j) $Re = 2956$	48
Figure 3-5: Horizontal and streamwise velocity ratio for the 3.5 mm bubble cases at $j_g = 0.36$ m/s and at $y/D = 1.0$ (a-b), $y/D = 1.5$ (c-d), and $y/D = 2.0$ (e-f).	50
Figure 3-6: Horizontal velocity ratios (a,c,e) and vertical velocity ratios (b,d,f) for the 0.53 mm bubble cases at $y/D = 1.0$ (a-b), $y/D = 1.5$ (c-d), and $y/D = 2.0$ (e-f).	52
Figure 3-7: Liquid velocity ratio from the PSIV analysis at $Re = 2,956$ in (a) horizontal direction and (b) vertical direction.	54
Figure 3-8: Time-averaged net force acting on bubbles in (a) horizontal direction and (b) vertical direction.	59
Figure 3-9: Time-averaged force balance on air bubbles behind a cylinder at $y/D = 1.5$ (a) in x direction and (b) in y direction.....	60
Figure 3-10: Comparison of lift-to-drag ratio to inertia-to-drag ratio and the maximum void fraction ratio in the wake ($0 < y/D < 5$).....	62
Figure 4-1: Contour plots of the void fraction ratio behind the cylinder at $j_g = 0.36$ m/s (a) $Re = 493$ (b) $Re = 1,478$, and (c) $Re = 2,463$ (d) $Re = 2,069$	67

Figure 4-2: Horizontal (left) and vertical (right) velocity ratios for the air bubbles at $y/D = 1.0$ (a-b), $y/D = 1.5$ (c-d), and $y/D = 2.0$ (e-f).....	69
Figure 4-3: Horizontal (left) and vertical (right) velocity ratios for water at $y/D = 1.0$ (a-b), $y/D = 1.5$ (c-d), and $y/D = 2.0$ (e-f).....	71
Figure 4-4: Time-averaged net force acting on bubbles in (a) the horizontal direction at $Re = 493$, (b) the vertical direction at $Re = 493$, (c) the horizontal direction at $Re = 1,478$, (d) the vertical direction at $Re = 1,478$, (e) the horizontal direction at $Re = 2,463$, and (f) the vertical direction at $Re = 2,463$	73
Figure 4-5: Time-averaged force balance on air bubbles behind a cylinder: (a,c,e) in x direction at $y/D = 1.0$ and (b,d,f) in y direction at $y/D = 1.5$	75
Figure 4-6: Vector plots of the time-averaged net force acting on bubbles at (a) $Re = 493$, (b) $Re = 1,478$, and (c) $Re = 2,463$. (Note, the magnitude of the vectors is scaled independently).....	76
Figure 4-7: Horizontal (left) and vertical (right) mean liquid velocity ratios at $y/D = 1.5$ (a-b) and $y/D = 2.5$ (c-d) for the two-phase and single-phase crossflows at $Re = 2,956$	79
Figure 4-8: Horizontal (left) and vertical (right) fluctuating liquid velocity ratios at $y/D = 1.5$ (a-b) and $y/D = 2.5$ (c-d) for the two-phase and single-phase crossflows at $Re = 2,956$	80

LIST OF TABLES

Table 1-1: Classification of a two-phase flow [7].....	2
Table 2-1: Experimental flow conditions.....	21
Table 4-1: Experimental flow conditions.....	65

ACKNOWLEDGEMENTS

I sincerely appreciate my advisor, Dr. Matthew J. Rau, for his guidance and mentorship during my academic journey. As an experimental researcher, my job was not simply solving the complex physics of fluid mechanics. It also included an engineering design process of defining research ideas, ideating and prototyping experimental equipment, creating testing procedures, collecting and processing data, etc. I am thankful for his assistance in providing me with an environment where I could explore and develop my skills as an experimental researcher. I would also like to express my gratitude towards my dissertation committee members, Dr. Stephen P Lynch, Dr. Alexander S. Rattner, Dr. Fan-Bill B. Cheung, and Dr. Ali Borhan, for their advice and review of my achievements.

I am also grateful to my friends, classmates, and the university communities who were part of my academic journey and shared important memories. In particular, I appreciate Yixuan Song for his support as a friend and colleague. Most importantly, I deeply thank my parents, Jigyeong Kim and Oklim Park, who have unconditionally supported my journey in life.

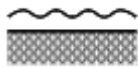
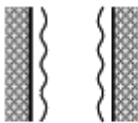
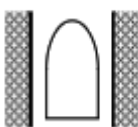
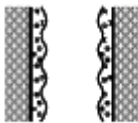
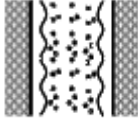
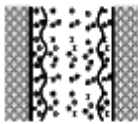
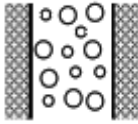
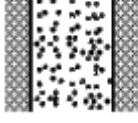
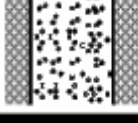
1. Introduction

1.1 Background

Flow boiling inside a two-phase heat exchanger can be a highly efficient heat-exchanging mechanism due to enhanced heat transfer through evaporation [1,2]. However, two-phase heat exchanger performance can be limited if the critical heat flux (CHF) is achieved when the vapor phase covers the heated surface and surface dryout occurs. This event, where liquid cannot continually rewet the heated surface is called the boiling crisis, where the surface temperature drastically increases [3]. Understanding how to design and operate two-phase heat exchangers to prevent the early occurrence of boiling crisis and minimize gas holdup on or near the heat exchange surfaces will be important for further advances in these technologies.

For the advancement in two-phase heat exchanger design, it is important to properly understand the physics of a two-phase flow. However, understanding a multiphase flow system is more challenging compared to those with a single-phase flow due to its complex environment of multicomponent physics. Multiphase flow occurs when there are more than two thermodynamic phases – solid, liquid, and gas – in a system. A multiphase mixture can be easily found in natural systems, such as rain, snow, and air pollutants, and can be found in modern industries, such as process and transport systems, energy generation, and environmental controls [4]. Unlike a single-phase flow, a multiphase flow has interfaces between two or more phases. In most particle flows, such as a liquid-solid or gas-solid flow, surface deformation on the phase interfaces is not significant [5]. However, significant surface deformation occurs in a liquid-gas system [6], which increases the complexity of the multiphase flow behavior. For example, Serizawa and Kataoka showed that energy exchange occurred between liquid turbulence and air bubble interfaces

Table 1-1: Classification of a two-phase flow [7].

Class	Typical regimes	Geometry	Configuration	Examples
Separated flows	Film flow		Liquid film in gas Gas film in liquid	Film condensation Film boiling
	Annular flow		Liquid core and gas film Gas core and liquid film	Film boiling Boilers
	Jet flow		Liquid jet in gas Gas jet in liquid	Atomization Jet condenser
Mixed or Transitional flows	Cap, Slug or Churn-turbulent flow		Gas pocket in liquid	Sodium boiling in forced convection
	Bubbly annular flow		Gas bubbles in liquid film with gas core	Evaporators with wall nucleation
	Droplet annular flow		Gas core with droplets and liquid film	Steam generator
	Bubbly droplet annular flow		Gas core with droplets and liquid film with gas bubbles	Boiling nuclear reactor channel
Dispersed flows	Bubbly flow		Gas bubbles in liquid	Chemical reactors
	Droplet flow		Liquid droplets in gas	Spray cooling
	Particulate flow		Solid particles in gas or liquid	Transportation of powder

through surface deformation and fragmentation of turbulence eddies as the geometry of the interface varied [6]. In addition to this two-way coupling, the complexity of multiphase flows stems from their many possible flow regimes. Based on the interfacial structure and the individual kinetic energies of the liquid and the gas phases, a liquid-gas flow can be classified as a bubbly, slug, churn, annular, or film flow [7]. Ishii and Hibiki [7] classified a two-phase flow based on the interfacial regimes, as shown in Table 1-1.

Compared to natural and forced convection heat transfer, it is known that boiling heat transfer is more effective at carrying energy away from a heated surface [8]. However, CHF should be carefully understood for designing and operating a two-phase heat exchanger to prevent a boiling crisis. Several researchers showed the practicality of two-phase heat exchangers [9–12]; however, Ribatski and Thome concluded that the general design of a two-phase heat exchanger is not yet well-defined [10]. In addition, investigations on jet impingement boiling with heat sinks revealed that it is important to efficiently remove vapor bubbles from the heated surface to increase CHF [13,14]. An array of pin-fin structures augmented two-phase heat transfer; however, the heat transfer enhancement was maximized with an active bubble removal from the surface [15]. Consequently, understanding how bubbles can easily escape from within arrays of boiling surfaces, fins, and tubes will be important to the future design of two-phase heat exchangers.

In this research, fundamental studies of two-phase flow and its interactions with flow structures relevant to the design of two-phase heat exchangers or heat sinks are pursued. Traditionally, fins and tubes are popular structures for designing a single-phase heat exchanger due to the creation of large heat exchanging surfaces and disturbance of flow generated from bluff bodies. However, such structures may cause a delay in bubble removal and affect the performance of a two-phase heat exchanger. In Chapter 1.2, this thesis reviews the fundamental characteristics of single-phase flow structures around a cylinder. In Chapter 1.3, two-phase wakes

around a cylinder are reviewed to understand how they differ from the wakes with a single-phase flow structure.

1.2 Bluff Bodies in a Single-Phase Crossflow

A crossflow around a bluff body, such as a cylindrical tube or fin, is commonly used in heat exchanger design due to its simplicity and practicality [16]. Numerous empirical correlations are available to characterize single-phase heat transfer across a circular cylinder [3]. Bergman *et al.* [3] stated that heat transfer performance is strongly related to a boundary layer development on the surface of the cylinder. The boundary layer is a thin layer of fluid where large velocity gradients and shear stresses exist, as shown in Figure 1-1. The boundary layer occurs when fluid near the surface has little momentum to overcome the pressure gradient [3,17].

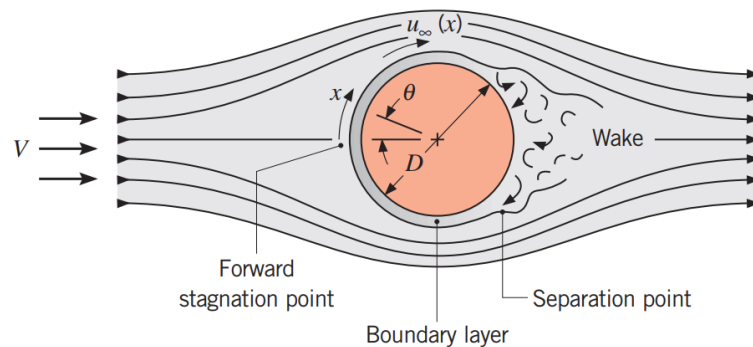


Figure 1-1. Boundary layer formation and separation of flow on a single-phase flow around a cylinder. [3]

For the past several decades, numerous researchers have experimentally and numerically investigated wakes caused by a single-phase flow around a circular cylinder as flow separation and vortex shedding occur [18,19]. It was discovered that a hydrodynamic instability in the developing velocity profile near the cylinder causes the growth of flow separation and vortices [20]. In addition, the cylinder Reynolds number (Re) fully parameterizes the characteristics of the developing boundary layers and the cylinder wake, defined as

$$\text{Re} = \frac{\rho V D}{\mu}, \quad (1-1)$$

where ρ is the fluid density, V is the freestream fluid velocity, D is the cylinder diameter, and μ is the dynamic viscosity of the fluid. From a macroscopic viewpoint, there are three flow regimes: laminar, transitional, and turbulent. The laminar state of flow is in the range of $0 < \text{Re} < 350-400$. Transition to a turbulent state starts in the range of $180-200 < \text{Re} < 350-400$ and becomes fully turbulent when $\text{Re} > 3.5 \times 10^6$ [19,21]. The transitional regime is met when the Reynolds number is between the laminar and turbulent regimes.

Zdravkovich [19] reported transitional wakes in free shear layers when the Reynolds number is in the range of $350-400 < \text{Re} < 1,000-2,000$ and eddies in transition to turbulence in the free shear layer when the Reynolds number is in the range of $1,000-2,000 < \text{Re} < 20,000-40,000$. The author described this group of Reynolds numbers as being in a state of transition in the free shear layers. It is also called a subcritical state where boundary layers remain laminar, but shear layers become turbulent. Generated from spanwise contraction and stretching of the large-scale Kármán vortices, small-scale Kelvin-Helmholtz vortices become a distinct feature of the near-wake structure when $\text{Re} > 5,000$ [22–24].

Kelvin-Helmholtz instabilities from these vortices can increase the Nusselt number [25], the ratio of convective and conductive heat transfer in a boundary layer. The Nusselt number is defined as

$$Nu_D = \frac{hD}{k}, \quad (1-2)$$

where h is the convective heat transfer coefficient and k is the conductive heat transfer coefficient. This investigation revealed the average Nusselt number suddenly increased because of alternating reattachment of the boundary layers at the rear of a cylinder when the Reynolds number was greater than 5,000. Also, the average Nusselt number increased as the Reynolds

number increased from $Re = 3,000$ to $15,000$. In other words, the literature suggests the convective heat transfer becomes very effective around the transitional range of the Reynolds number.

However, the specific subcritical Reynolds number, when the transition to turbulence in the wakes occurs, is not universal in the literature. Norberg and Prasad & Williamson reported the subcritical Reynolds number is $5,000$ [23,24]. Nakamura and Igarashi reported a range of subcritical Reynolds numbers between $5,000 < Re < 8,000$ [25]. Other researchers focused on higher subcritical Reynolds numbers up to $Re = 50,000$ [26]. One of the possible explanations for these inconsistencies is the effect of the bluff body aspect ratio. An experimental investigation revealed that cylinders with aspect ratios as large as $L/D = 60 - 70$ required $Re = 4,000 - 10,000$ to reach the subcritical regime, while cylinders with aspect ratios as small as $L/D = 10 - 30$ only required $Re = 350 - 4,000$ [27]. This variation was due to the end conditions where cylinders were connected to the wall. A study of numerical analysis also confirmed that the wakes around the cylinders are influenced by the aspect ratios [28]. This study also categorized wakes based on the dimensionless downstream distance, y/D , where very-near wakes were defined as $y/D < 3$ and near wakes were defined as $3 < y/D < 10$. The author reported that very-near wakes were dominated by the shear layer, which was sensitive to disturbances generated from the cylinders and the aspect ratios.

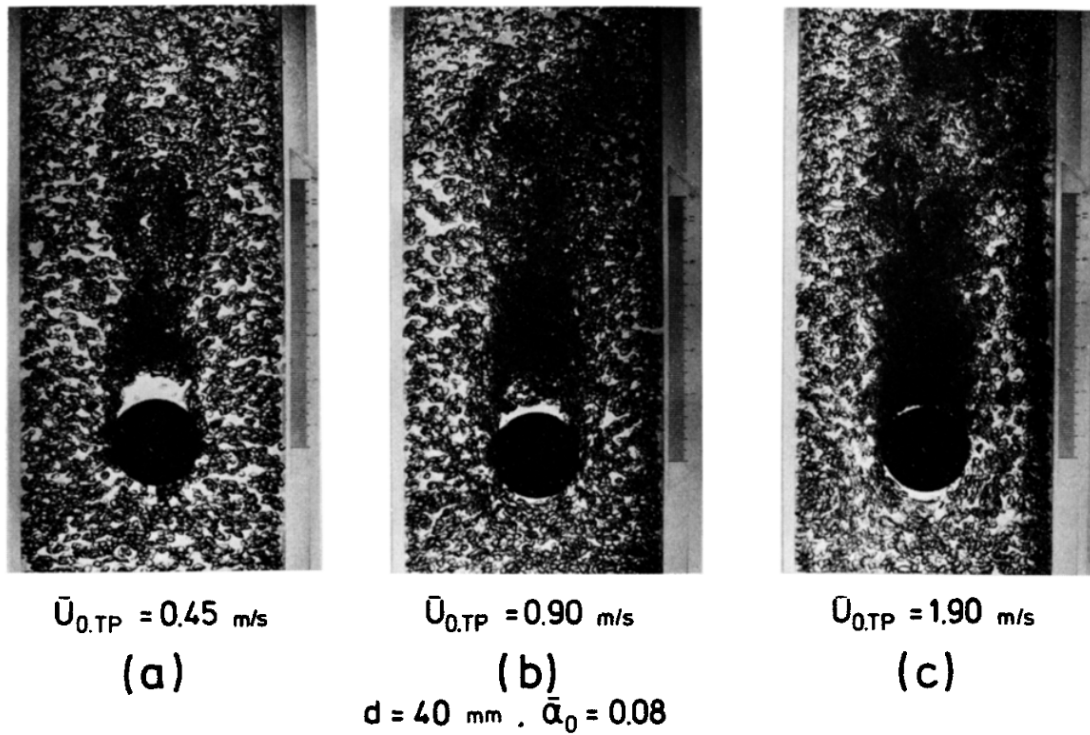


Figure 1-2. Photographs of upward two-phase wakes around a cylinder, where $\bar{U}_{0,TP}$ is the mean flow velocity, d is the cylinder diameter, and $\bar{\alpha}_0$ is the mean void fraction [29]. In these photographs, liquid is bright and the bubbles and cylinders appear dark.

1.3 Bluff Bodies in a Two-Phase Crossflow

There have been some attempts to understand wakes from bluff bodies in two-phase crossflow. Similar to the single-phase wakes from bluff bodies, the wakes are impacted by the Reynolds number and the separation of boundary layers. However, there are still many inconsistencies in the literature that show that two-phase crossflow is not well-understood. In particular, Magnaudet and Eames [30] summarized the main challenges in describing the behavior of bubbly two-phase flows: (1) a slip boundary condition exists on the interfacial area, (2) the liquid phase dominates inertia-induced hydrodynamic forces due to the low density of gases, and (3) the shape of the bubbles constantly change. These and other characteristics lead to the unique behavior of bubbly wakes in two-phase crossflow, which are summarized in the following sections.

Similar to the single-phase flow, the hydrodynamics of bubbles and bubbly flows can be discussed in terms of the Reynolds number [30]. Focusing on the bubbles, the Reynolds number can be defined as $Re_b = \rho d|U|/\mu$, where ρ and μ are the density and the dynamic viscosity of the liquid and U is the relative velocity of the bubble [30–32]. However, there is inconsistency in defining the Reynolds number for the two-phase crossflow. Inoue *et al.* [29] focused on the bulk velocity of the two-phase flow to define a Reynolds number. They derived a two-phase-averaged velocity as $U_{TP} = \sqrt{2\Delta p / (\rho_L(1-\alpha) + \rho_G\alpha)}$, where Δp is dynamic pressure, α is the void fraction, and ρ_L and ρ_G are liquid and gas densities, from deriving the Bernoulli's equation in a two-phase flow. By using the two-phase velocity, the two-phase Reynolds number can be defined as $Re_{TP} = \rho dU_{TP}/\mu$. Even though they categorized the bulk movement of the liquid-gas flow in terms of a Reynolds number, they did not explain the non-uniform distribution of bubbles around a circular cylinder in terms of the two-phase Reynolds number. Sugiyama *et al.* [33] used the bubble Reynolds number, Re_b , to calculate the drag coefficient of bubbles; however, the

researchers characterized the wakes around a circular cylinder in terms of the liquid Reynolds number and cylinder diameter, as shown in Eq. 1-1. In a recent study, Lee and Park [34] investigated a bubbly flow around a circular cylinder in stagnant water. The researchers used the bubble Reynolds number as a key dimensionless parameter for their experimental investigation. However, they used the liquid Reynolds number to characterize the size of wakes around the cylinder.

This article uses the liquid Reynolds numbers to describe the flow conditions. In Chapter 2.1, the void fraction measurement concluded that the maximum freestream void fraction of the experimental conditions was approximately 2%. As the freestream void fraction was less than 3%, the two-phase flow is treated as a bubbly flow [9]. The mixture viscosity of a bubbly flow can be found as $\mu_m = \mu_l / (1 - \alpha)$, where μ_l is the liquid viscosity and α is the void fraction [7]. In addition, the mixture density for the bubble flow can be defined as $\rho_m = \rho_l(1 - \alpha) + \rho_g\alpha$, where ρ_l is the liquid density and ρ_g is the gas density [7]. As the liquid density is much greater than the gas density ($\rho_l \gg \rho_g$), the mixture density can be approximated as $\rho_m \approx \rho_l(1 - \alpha)$. At the maximum void fraction of 2%, the liquid Reynolds number was only off by 4% from Reynolds number based on mixture density and viscosity. As the mixture Reynolds numbers are not far from the liquid Reynolds number, the Reynolds numbers are calculated by the liquid density and viscosity.

1.3.1 Bubble-Trapping Region

One distinct characteristic of a two-phase crossflow is a liquid-phase wake region where a liquid-rich layer is formed at the rear of the cylinder [29]. In addition, a bubble-trapping wake region is formed further downstream from the cylinder, where bubbles accumulate in higher concentrations compared to the freestream. Along with vortices generated from the flow

separation around the cylinder, a significant change in pressure and liquid velocity distribution around the bluff body can distort the void fraction distribution and cause strong bubble densification or dispersion [29,35,36]. Due to the distortion, strong entrainment of the liquid flow directly downstream of the cylinder creates a region where the air bubbles cannot penetrate, as shown in Figure 1-2. Note, the liquid appears light compared to the dark bubbles in this figure.

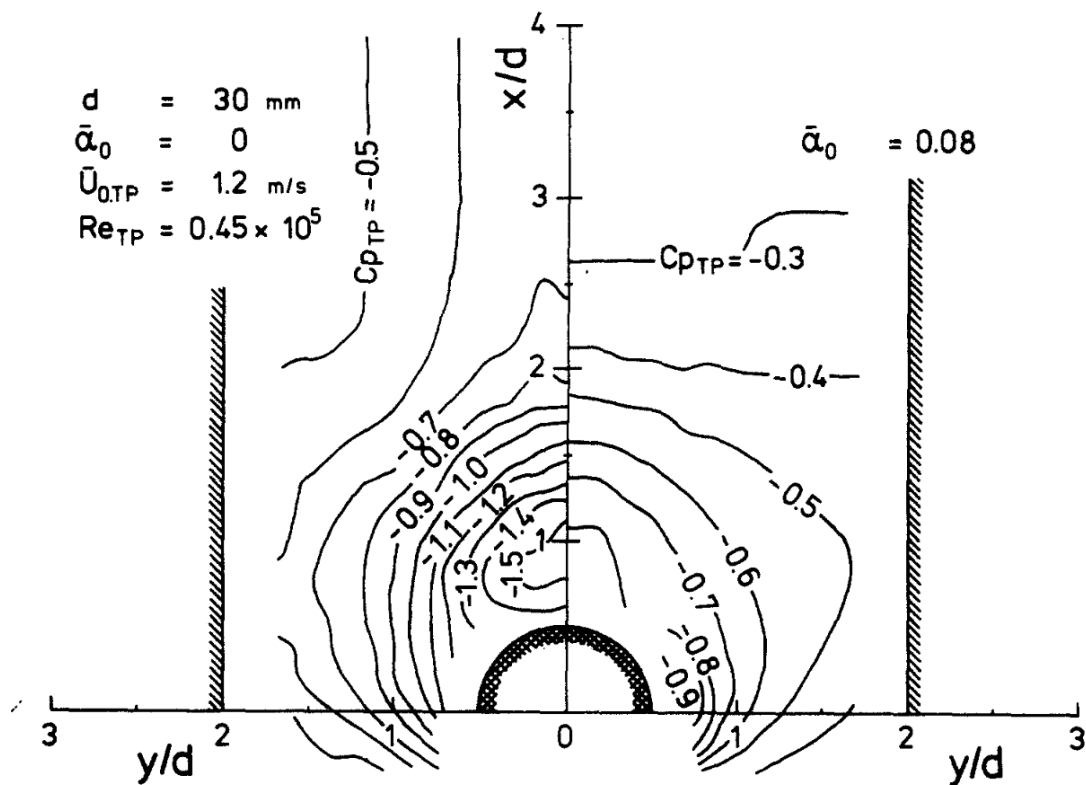


Figure 1-3. An example of static pressure distributions for single-phase flow (left) and two-phase flow (right) [29].

Vortex emission, which contributes to the void fraction patterns described above, can be altered from their single-phase characteristics due to the presence of the second phase in a two-phase crossflow [37]. The experimental investigation by Hulin *et al.* [37] reported that a bubbly flow with void fraction values up to 0.1 generated stable vortices from the bluff bodies at the

liquid Reynolds number up to $Re = 7,000$. Uniformly injected air bubbles with a mean bubble size of 2-4 mm were drawn into the vortices and concentrated at the vortex cores. The investigation concluded that the gas bubbles were trapped inside the vortex core, where its velocity and static pressure were low. When the void fraction value was greater than 0.1, vortex formation was more erratic with low spatial coherence.

Compared to wakes from a single-phase crossflow, the wakes in a two-phase crossflow have a smaller width due to a faster recovery of mean velocity [29,35,36]. From their series of publications [29,35,36], the Inoue *et al.* research team concluded that buoyancy forces of the air bubbles in the region of high void fraction made the wakes narrower compared to the single-phase flow case. Also, compared to a single-phase flow, the overall static pressure distribution was lower for the two-phase flow, as shown in Figure 1-3. The authors described that the lower static pressure distribution in Figure 1-3 caused the liquid-phase region in Figure 1-2, as the pressure gradient near the cylinder prevented bubble movement into the liquid-phase region. As the mean velocity of the two-phase flow increased, the liquid-phase wake region became thinner. In addition, the authors reported the formation of an additional liquid-phase wake region in front of the cylinder due to the static pressure gradient when the mean velocity increased. Although a decrease in the local static pressure of the two-phase flow was not as strong as in the single-phase flow, the literature suggested that the static pressure distortion around the cylinder was sufficient to decrease the buoyancy forces on the bubbles relative to the freestream. At the same time, the authors mentioned that a slip velocity ratio, a ratio between air and liquid velocities, decreased with increasing bubble drag coefficient. Bubble densification occurred in the direction normal to the flow due to a lift force, which was induced by the liquid velocity gradient.

The complex wake dynamics in a liquid-gas crossflow have also been shown to cause higher drag coefficients on a single tube than in a single-phase flow [38]. Varying Reynolds numbers from 430 to 21,900 and void fraction from 0.25 to 0.4, Joo and Dhir [38] compared the

magnitude of the two-phase drag coefficient and single-phase drag coefficient. At low Re , they discovered the two-phase drag coefficient increases dramatically, for instance about 600 times at $Re = 717$. However, there was a relatively smaller gain in drag coefficient at high Re , for instance about four times at $Re = 8,200$. The authors commented that it was hard to distinguish if the pressure drop behind the cylinder was mainly caused by the acceleration of flow or viscous dissipation. However, the authors explained that the velocity difference between liquid and gas phases caused additional viscous dissipation. Consequently, it is expected the effect of void on the viscous dissipation decreases when Reynolds number or liquid inertia increases. If the two-phase flow is mostly dominated by the inertial effect of the liquid phase, viscous dissipation generated from the voids will diminish.

A numerical investigation of a bubbly flow around a circular cylinder also confirmed the accumulation of bubbles into shedding vortices behind the cylinder [33]. By evaluating different bubble sizes, the numerical analysis concluded that there was a conditional occurrence of the bubble-trapping wake region. At $Re = 3,000$, the accumulation occurred when larger bubbles, $d/D = 0.03$, were used; however, no accumulation occurred when small bubbles, $d/D = 0.01$, were analyzed (d represents mean bubble diameter and D is the cylinder diameter). The results suggested the relaxation time of bubble motion, or bubble response time, may be important for the occurrence of bubble trapping as stronger vortex shedding occurs with greater inertial effects and bubbles become more responsive to a local pressure gradient. In Chapter 1.3.2, a review of the relaxation time of a bubble and preferential concentration is available.

A recent experiment on the bubble-induced liquid-air movement around a circular cylinder confirmed that bubble trapping occurs at Reynolds numbers between 2,000 and 5,000 [34]. By comparing their results to their previous single-phase flow experiments [39], their results suggested that enhanced mixing of the flow occurred by introducing air bubbles into the liquid flow. The two studies compared the distance between the center of the cylinder and a point of

zero mean streamwise velocity on the centerline behind the cylinder. The comparison showed the distance (y/D) decreased from $\sim 1.9-2.0$ to 0.7 as air bubbles were injected [34]. The authors could not provide a clear answer to the analysis; however, they argued that preferential migration of the bubbles behind the cylinder, or the phenomenon of bubble trapping, was responsible for the reduced size of recirculation wakes. Consequently, they believed the enhanced mixing also occurred behind the cylinder with an injection of air bubbles. However, this result was only verified for a void fraction of 0.011 and other results were inconclusive.

1.3.2 Preferential Concentration

Preferential concentration, where a dispersed phase in a flow tends to gather preferentially within a region due to turbulence in the continuous surrounding fluid, might also be related to the occurrence of bubble trapping. The Stokes number (St), a dimensionless parameter that compares a characteristic timescale of the dispersed phase to a characteristic timescale of the continuous flow, can indicate when preferential concentration becomes important. The Stokes number is defined as

$$St = \frac{\tau_b}{\tau_f}, \quad (1-3)$$

where the characteristic time of the particles or bubbles is τ_b and the characteristic time of the liquid flow is τ_f . The ratio between the two characteristic timescales represents the inertial difference between bubbles and the fluid flow. It is commonly known that a Stokes number significantly smaller than one indicates that the dispersed phase is easily influenced by the continuous phase and largely follows the flow as it has a larger inertia. However, when the Stokes number is significantly larger than one, fluid motions, including turbulence, have less effect on

the dispersed phase as the bubbles have more significant inertia [40]. Maximum preferential concentration occurs at $St \approx 1$ when turbulent eddies attract particles and form clusters [41].

The preferential concentration effects have been shown to influence the distribution of the dispersed phase in two-phase crossflows with inertial particles [42,43]; however, this has not been shown as distinctly for gas bubble interaction with bluff body wakes in two-phase crossflows. An experimental study with large bubbles, $d = 5$ mm, confirmed the presence of preferential concentration effects in turbulent bubbly flows [44]. However, the phenomenon of preferential accumulation of bubbles may not be valid for a fluid flow with very small bubbles in low Reynolds numbers with homogeneous, isotropic, and decaying turbulence [45]. In this study, small bubbles were defined as air bubbles with their mean diameter and their response time smaller than the Kolmogorov length and time scales. This numerical analysis showed the preferential accumulation of the small bubbles only occurred in the centers of intense vortices, which corresponds to the centers of intense vortices, but the preferential concentration was weak because of the small size of the bubbles. However, other experiments have observed strong preferential concentration by injecting small bubbles in a horizontal water channel with a homogeneous isotropic decaying turbulent flow at a high Reynolds number [46]. Comparing the experimental rise velocities to theoretical rise velocities of small air bubbles, $d = 0.1 - 0.5$ mm, Aliseda and Lasheras [46] observed a significant reduction of bubble rise velocity due to preferential concentration with Stokes numbers of order unity. In addition, other studies also reported preferential concentration occurred in regions with high vorticity [47,48]. A numerical investigation of a bubbly flow around a circular cylinder concluded that a large characteristic time of the bubbles was needed for bubble accumulation behind the cylinder [33]. However, Sugiyama *et al.* [33] did not conclude the bubble accumulation in Stokes number as they excluded the effects of the characteristic times of the fluid.

1.3.3 Bubble Trapping Forces

Specific to two-phase flow around a cylinder, there is no direct literature that explains the flow conditions that result in bubble trapping behind the cylinder. So far, it has been known that the velocity of the two-phase flow, cylinder diameter, and bubble diameter affect the occurrence of the bubble-trapping wake region, but no relationships predicting its occurrence or severity yet exist. One study, which focused on bubble trapping by modeling a liquid-air mixture as a two-stream planar mixing layer, as shown in Figure 1-4, explained that bubble clusters traveled under the influence of inertial, drag, buoyancy, and lift forces [49]. Assuming an air bubble is a sphere for which generalized equations describing the net forces in a fluid have been developed [50,51], Sene et al. [49] reconstructed the generalized force law to include lift forces and added mass forces of a spherical bubble and estimated the order of magnitudes of the forces on the bubble.

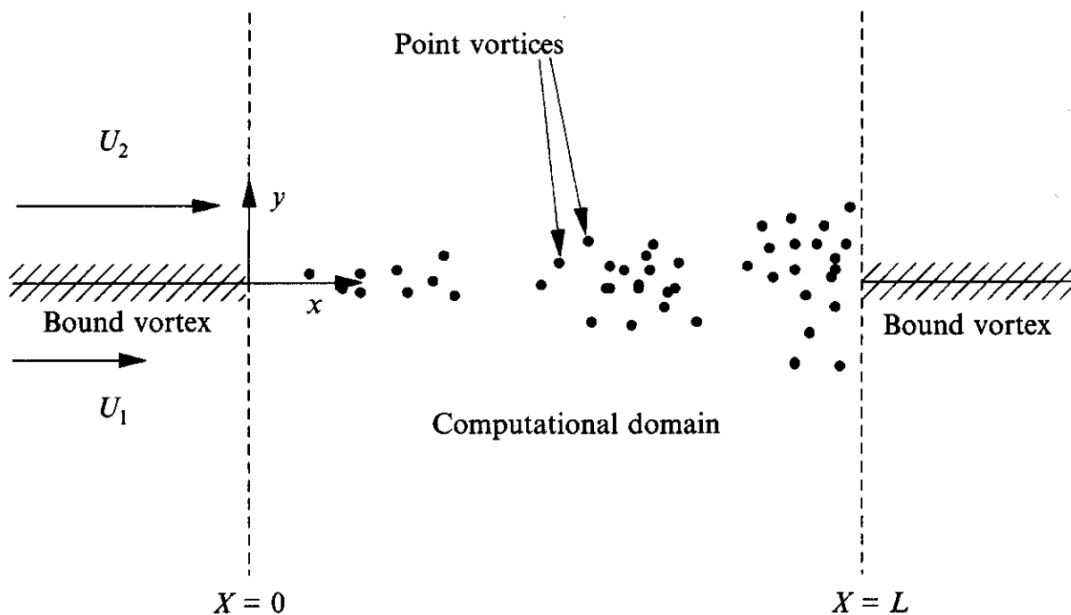


Figure 1-4. A sketch of a two-stream planer mixing layer for simulating bubble trapping. [49]

This allowed, Sene *et al.* [49] to introduce an inertia-to-buoyancy ratio, Π , and a bubble trapping parameter, Γ , to characterize the relative effects of the flow mixture. The ratio of these two parameters, Π/Γ , characterizes the ratio of lift-to-drag forces acting on the bubbles in the flow. By applying the characteristic length and velocities of the two-phase flow around a cylinder, the two parameters can be defined as follows,

$$\Pi = u_{l,\infty}^2 / 2gD, \quad (1-1)$$

$$\Gamma = u_{l,\infty} / (u_{g,\infty} - u_{l,\infty}). \quad (1-2)$$

High values of Π and Γ are needed to trap air bubbles in vortices. The authors explained that as vortices become stronger, they can attract air bubbles when the inertial forces due to the vortex motion become greater relative to bubble buoyancy or gravity forces. Besides, they noted a large value of Γ , which describes a relatively greater freestream liquid velocity compared to the bubble slip velocity or the air terminal velocity, is needed so that air bubbles can easily enter the coherent structures. In other words, it explained that a faster freestream liquid velocity results in a strong shear as Γ becomes larger, making the lift force on a bubble comparable with the inertial force. Also, the study reported critical values of Π and Γ , which vary depending on the flow conditions. In the case of the planar mixing layer, the critical value of Γ is about 10 when $\Pi \rightarrow 0$ and Γ is about 3 when $\Pi \approx 0.5$.

Sugiyama *et al.* [33] used the Froude number (Fr), a similar nondimensional parameter to Π , to numerically analyze a bubbly flow around a cylinder. The Froude number is a dimensionless number defined as the ratio of inertial forces to gravity as follows,

$$Fr = \sqrt{u_{l,\infty} / gD}. \quad (1-3)$$

However, their usage of the Froude number was limited to comparing two-phase wakes at a specific flow condition with or without the gravity or buoyancy force. At $Re = 2000$, their results showed bubble trapping occurred without gravity ($Fr = \infty$). They also showed the bubble trapping

occurred with gravity ($Fr = 1$); however, the bubble trapping was weaker due to buoyancy moving bubbles downstream.

Based on the literature above, the bubble-trapping around a circular cylinder seems related to the inertial forces. When the liquid velocity is fast, it will result in a high value of the inertia-to-buoyancy ratio, as shown in Eq. 1-4, or the Froude number, as shown in Eq. 1-6. These equations provide hints about the bubble-trapping phenomenon; however, they do not provide thorough information about when and how the bubble trapping occurs. In addition, Sene *et al.* [49] also suggested that lift forces induced by the velocity difference between the liquid and gas phases may play an important role in explaining the bubble-trapping phenomenon. However, this has not been experimentally or numerically proven for a two-phase flow around a bluff body. It is unclear how the bubble trapping in two-phase wakes around a cylinder is related to the inertial and lift forces.

2. Characterization of Two-Phase Wakes in an Upward Liquid-Gas Flow around a Cylinder

This chapter reports an experimental investigation to characterize two-phase wakes around a cylinder. A vertical water channel facility was designed to inject a mixture of liquid and gas fluids in the upward direction. A circular cylinder was installed across the water channel in the test section. Also, in the test section, a high-speed camera observed the movement of the bubbles around the cylinder. The two-phase wakes around the cylinder were characterized by a void fraction ratio, which is defined as the ratio of the local void fraction to its freestream value. The time-averaged high-speed images of the two-phase flow revealed that liquid-phase and bubble-trapping regions could be formed around the cylinder based on the flow conditions. The material in this chapter is also available in published articles [52,53].

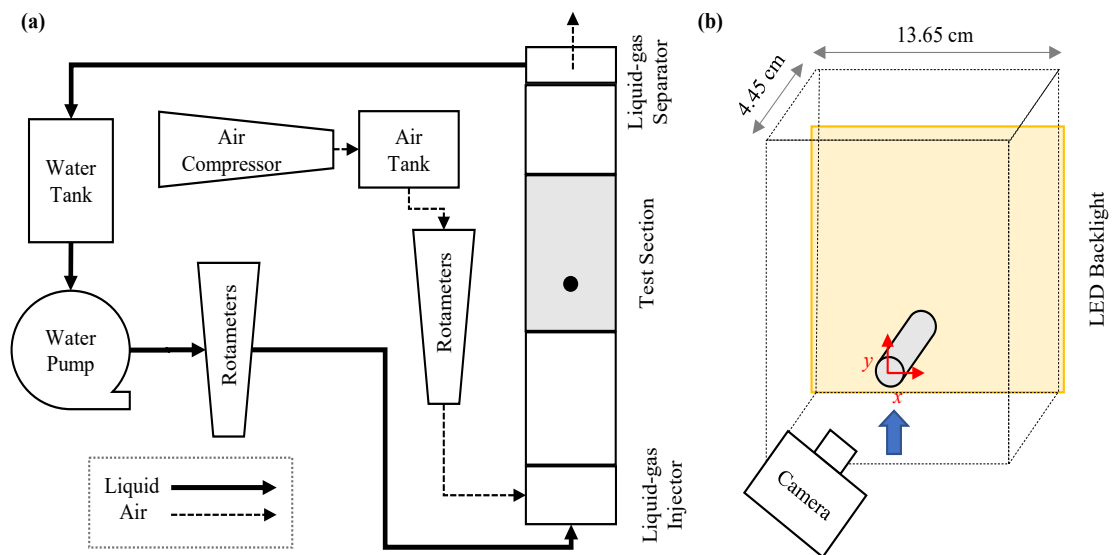


Figure 2-1: Illustration of experimental facility: (a) flow chart, (b) test section and its field of view.

2.1 Method

2.1.1 Experimental Apparatus

The flow loop designed for an upward liquid-gas flow across a cylinder in a channel is shown in Figure 2-1. The setup includes a test section with a rectangular cross-sectional channel ($13.65 \times 4.45 \text{ cm}^2$) and a circular cylinder (diameter $D = 9.5 \text{ mm}$, length $L = 4.42 \text{ cm}$) installed horizontally across the channel. The aspect ratio (L/D) of the cylinder was 4.7. For visualization purposes, the facility was built using clear cast acrylic. At the bottom of the channel, three cylindrical air spargers, each with 10-micron pores, were installed in a 1×3 configuration for uniform injection of air bubbles across the channel. The circular cylinder was located 1.0 m from the bottom of the channel where the liquid-gas injector was located. From the center of the cylinder, coordinates of horizontal and streamwise directions are denoted as x and y , respectively. The coordinates and the field of view (FOV) are shown in Figure 2-1(b).

During the experiment, 1500 liters of tap water or a mixture of water and isopropanol solution of 0.016% v/v or 0.032% (v/v) were circulated through the water channel with a 10-HP centrifugal pump. A variable frequency controller regulated the frequency of pump rotation and the overall liquid circulation rate. The facility was maintained at room temperature of 20 °C and atmospheric pressure. A series of liquid rotameters (Dwyer, VFC) controlled liquid flow rates with 5% full scale (FS) accuracy. An air compressor (Quincy, QGB15V) delivered dry air at a controlled pressure of 138 kPa. A series of air rotameters (Dwyer, RMB) regulated air flow rates with 5% FS accuracy. Each time a change was made in the liquid flow rate or air flow rate, the liquid-air mixture was circulated for at least 25 minutes to reach a steady state. A high-speed camera (Photron FASTCAM SA) with a LED light panel (Forvitec StudioPRO) captured the movements of air bubbles in the test section.

Table 2-1: Experimental flow conditions.

Case	Re	j_g (m/s)	d (mm)	Re	j_g (m/s)	d (mm)
3.5 mm	99	0.06	3.0 ± 1.8	1,182	0.48	3.7 ± 2.5
	99	0.18	3.9 ± 2.8	1,182	0.60	3.8 ± 2.7
	99	0.36	4.3 ± 3.0	2,069	0.06	3.5 ± 2.3
	99	0.48	4.4 ± 3.2	2,069	0.18	3.4 ± 2.1
	99	0.60	5.0 ± 2.9	2,069	0.36	3.2 ± 2.0
	197	0.06	4.7 ± 2.8	2,069	0.48	3.0 ± 1.7
	197	0.18	4.2 ± 2.8	2,069	0.60	2.8 ± 1.7
	197	0.36	3.7 ± 2.5	2,956	0.06	2.7 ± 2.0
	197	0.60	2.9 ± 1.6	2,956	0.18	3.0 ± 1.9
	1,182	0.06	2.7 ± 1.5	2,956	0.36	3.3 ± 2.2
	1,182	0.18	2.9 ± 1.8	2,956	0.48	3.6 ± 2.3
	1,182	0.36	3.4 ± 2.2	2,956	0.60	3.8 ± 2.4
0.53 mm	296	0.06	0.53 ± 0.27	2,069	0.06	0.53 ± 0.28
	591	0.06	0.53 ± 0.27	2,956	0.06	0.52 ± 0.28
	1,182	0.06	0.54 ± 0.29			
0.48 mm	296	0.06	0.48 ± 0.25	2,069	0.06	0.48 ± 0.24
	591	0.06	0.49 ± 0.24	2,956	0.06	0.46 ± 0.22
	1,182	0.06	0.50 ± 0.24			

2.1.2 Experimental Conditions

The experimental flow conditions are presented in Table 2-1. A total of 36 cases are presented in this study. Liquid Reynolds number was varied from $Re = 99$ to 2,956 and the air superficial velocity was varied from $j_g = 0.061$ m/s to 0.614 m/s. The liquid Reynolds number based on the cylinder diameter was defined as shown in Equation 1-1. Due to the low void fraction of the experimental flow conditions, the two-phase Reynolds numbers, based on the two-phase mixture quantities, were not significantly off from the liquid Reynolds number. As mentioned in Chapter 1.1, the liquid Reynolds numbers are used to describe the flow conditions. The water-air experiments had mean air bubble diameters between 2.7 mm and 5.0 mm. These conditions are collectively presented as the 3.5 mm bubble cases in the subsequent sections. To

create smaller air bubbles, isopropanol was added to the water at a concentration of 0.016% (v/v) and 0.032% (v/v). Introducing a small amount of isopropanol reduced the surface tension of the water [54], which reduced the mean diameters of the injected air bubbles to ~0.53 mm and ~0.48 mm, respectively. These conditions are collectively presented as the 0.5 mm bubble cases in the subsequent sections. It was found that a large number of very small bubbles created during the experiments with the 0.5 mm bubbles quickly obscured the camera view at high rates of air injection. As a result, an air superficial velocity greater than 0.06 m/s in the water/isopropanol mixture could not be studied in the current experimental configuration for this small bubble size. The variation in bubble sizes for each experimental case is presented as standard deviations from the mean bubble size in Table 2-1.

The mean bubble diameter of 3.5 mm is comparable to other investigations where the bubbles were injected into the facility [34,55]. However, the bubble size in two-phase exchangers would be much smaller as the bubbles are generated from boiling heat transfer. A typical range of the bubble lift-off diameter is between 0.15 mm and 0.61 mm in a forced convective subcooled boiling flow [56]. As the current experimental facility does not generate bubbles from the subcooled boiling conditions, the slight modification of surface tension allowed the bubble injection with the typical bubble size in two-phase heat exchangers.

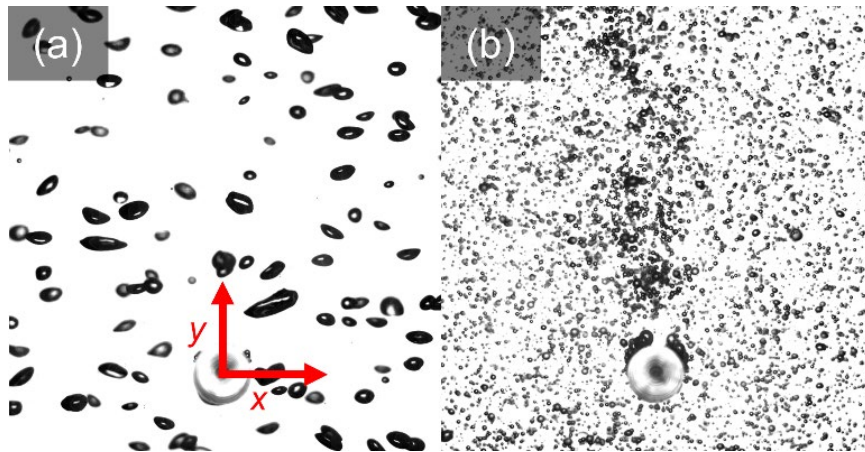


Figure 2-2: Raw photographs of the wake around the cylinder ($Re = 1,182$, $j_g = 0.06$ m/s) for (a) the 3.5 mm bubbles and (b) the 0.53 mm bubbles.

2.1.3 Image Acquisition and Processing

Shadow Fraction

The liquid-air flow movement of each experimental case was captured by the high-speed camera at 10,000 fps for 3.142 s. Figure 2-2 shows raw images from the experiment at a Reynolds number of $Re = 1,146$ and air superficial velocity of $j_g = 0.06$ m/s for the 3.5 mm bubbles (Figure 2(a)) and the 0.53 mm bubbles (Figure 2-2(b)). To quantify these bubble distributions, a shadow fraction image [57–60] was calculated from the sets of raw images to visualize the time-averaged wake profile for each case. In the channel, the bubbles blocked light from reaching the camera, where dark regions in the image indicated the presence of an air bubble and bright regions indicated regions of water. To calculate the shadow fraction, the raw images were first saved as 8-bit images with grayscale values between 0 and 255. After subtracting the background noise, which was calculated from a minimum grayscale intensity at each pixel location of an average of

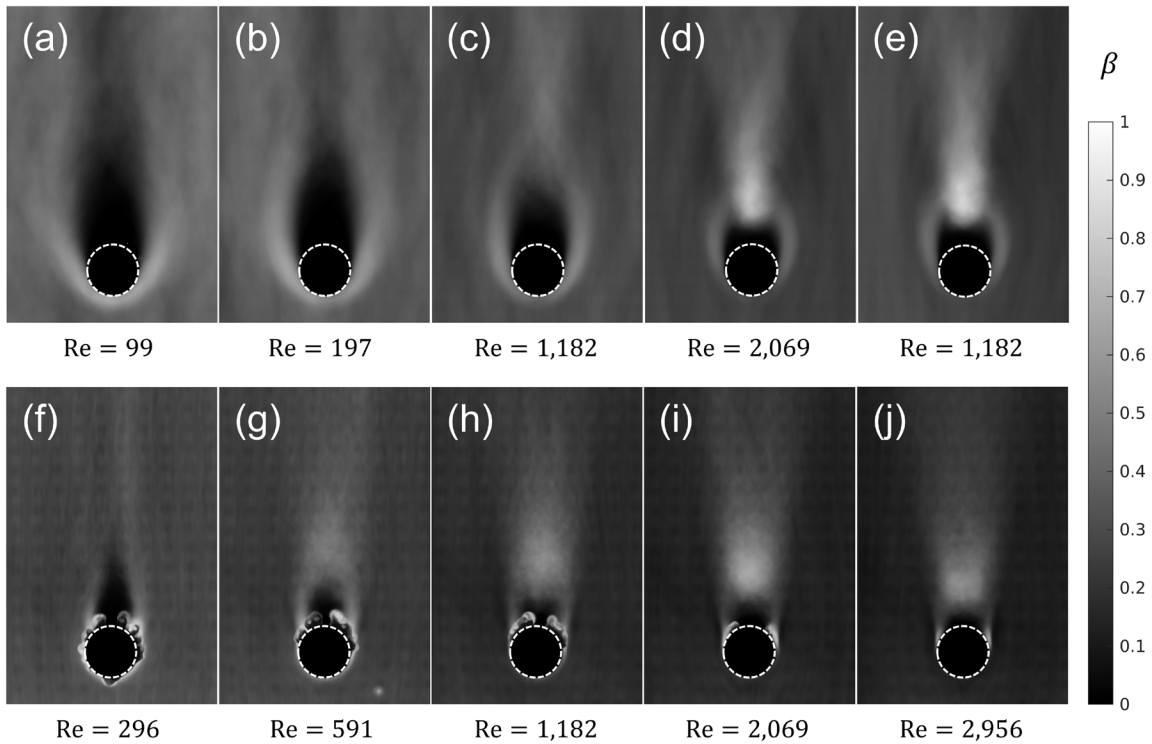


Figure 2-3: Shadow fraction images for $j_g = 0.36$ m/s with the 3.5 mm bubbles at liquid Reynolds numbers of (a) Re = 99 (b) Re = 197 (c) Re = 1,182 (d) Re = 2,069 (e) Re = 2,956 and for $j_g = 0.06$ m/s with the 0.53 mm bubbles at liquid Reynolds numbers of (f) Re = 296 (g) Re = 591 (h) Re = 1,182 (i) Re = 2,069 and (j) Re = 2,956.

3142 images, the grayscale intensity was inverted so that air bubbles were bright and liquid appeared dark. The inverse images were then binarized using a global threshold [61] for air bubble identification and sizing. As part of this binarization step, any remaining holes in the bright region produced due to light diffraction through the original bubble image were also filled. After all of the individual images were processed, the binary images were summed as integers to calculate a composite two-dimensional matrix of the two-phase flow over the time recorded. From this composite image, the shadow fraction was calculated as,

$$\beta = \frac{\text{Total count of bubble presence at a given pixel}}{\text{Total number of images}}. \quad (2-1)$$

The scale of the resulting shadow fraction was from zero to one, where zero indicated no bubble was detected and one indicated bubbles were present at that location in every image. Example shadow fraction images are shown in Figure 2-3(a-e) for the 3.5 mm bubbles and Figure 2-3(f-j) for the 0.53 mm bubbles across a range of liquid Reynolds numbers.

Void Fraction Correlation

While the shadow fraction is useful for observing time-averaged flow features, it is fundamentally a qualitative tool since it will be sensitive to the channel depth and bubble concentration. Each high-speed image is a simple 2-D projection, so overlapping bubble images can occur based on the depth of the water channel. A shadow fraction can be converted to an actual void fraction so long as additional information about the phase velocities and bubble overlap are known [57,58]. The overlapping probability of bubbles in a bubble plume was investigated by Murai *et al.* [58], and a method to correlate void fraction from shadow fraction was presented. In a subsequent study, an empirical expression to relate the void fraction and shadow fraction was proposed by Murai and coworkers [57] as,

$$\alpha = -\ln(1 - \beta) / C, \quad (2-2)$$

where the coefficient C included the probability of overlap within the shadow projection across a channel, which was determined through an empirical fit. The coefficient C for the present study was determined based on freestream bubble velocities measured in a separate study [62]. In this separate study, the freestream velocities of air bubbles (u_g) were measured using Particle Tracking Velocimetry at the flow conditions described in the current paper. The freestream void fraction was then determined by calculating the ratio between the air superficial velocity and actual air bubble velocities ($\alpha = j_g/u_g$). For this calculation, the freestream values of void fraction and shadow fraction were obtained upstream of the cylinder (at $y/D = -1.0$) to avoid the wake

effects of the cylinder. By conducting a least-squares fit between the void fraction and shadow fraction. The value of C was then determined through a least-squares fit between the void fraction and shadow fraction using the functional form of Eq. (2-2). The coefficient values were 33.5 ± 1.6 for the 3.5 mm bubbles, 97.6 ± 7.3 for the 0.53 mm bubbles, and 178.2 ± 5.6 for the 0.48 mm bubbles. As the concentration of isopropanol increased, the values of the coefficient C increased as expected due to the greater number of bubbles and greater overlap potential within the projected images [58].

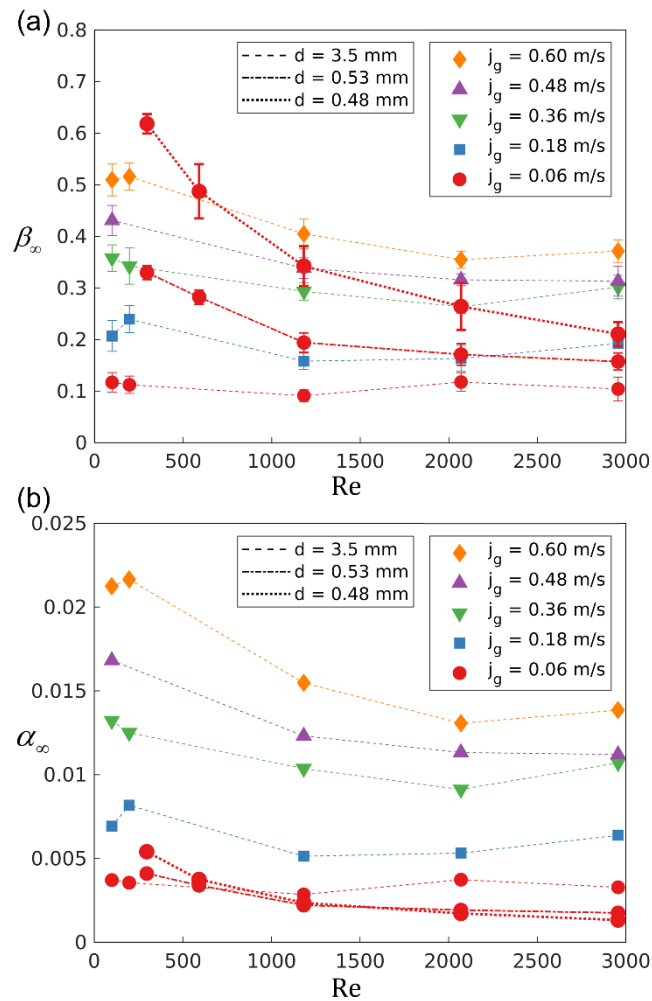


Figure 2-4: Freestream values of (a) shadow fraction and (b) void fraction after applying the correlation, plotted as a function of air superficial velocity and liquid Reynolds number.

Uncertainty of Correlation

The void fraction calculation described above is an indirect method to measure the local void fraction as a function of the observed shadow fraction. An estimate of the resulting uncertainty of this method was obtained from the uncertainty in the coefficient C along with the variation in the freestream conditions. The freestream shadow fraction values measured at $y/D = -1.0$ are shown in Figure 2-4(a). The uniformity of the freestream phase distribution is reflected by the errorbars, which are plotted as plus or minus one standard deviation of the variation of the shadow fraction across the channel width. Even though air bubbles were uniformly injected by the three spargers at the bottom of the water channel, standard deviations of the freestream shadow fraction varied from 4% to 22% of its mean value across the channel width, depending on the flow conditions. The median standard deviation of freestream shadow fraction measurements was 8%.

The uncertainty of the local void fraction was, thus, defined as,

$$\delta\alpha = \sqrt{\left(\frac{1}{C - \beta C} \cdot \delta\beta\right)^2 + \left(\frac{\ln(1 - \beta)}{C^2} \cdot \delta C\right)^2}. \quad (2-3)$$

Using a 95% confidence interval, the resulting uncertainty in the void fraction measurement ranged from 12% to 48%, with a median uncertainty of 20%. The overall uncertainty was relatively high; however, it included the spatial variation of bubble observations across the flow channel and experimental uncertainties of bubble visualization in the two-dimensional projections due to bubble overlap. These uncertainty estimates reflect some of the limitations of using two-dimensional visualization for void fraction measurements, where high-resolution measurement and pattern visualization are prioritized over absolute accuracy in the measurement value.

2.2 Result

2.2.1 Shadow Fraction and Void Fraction

The shadow fraction images for an air superficial velocity of $j_g = 0.36$ m/s are shown in Figure 2-3 for the 3.5 mm bubbles (Figure 2-3(a-e)) and the 0.53 mm bubbles (Figure 2-3(f-j)). In this figure, the cylinder is denoted as a dashed white line. Downstream of the cylinder, two distinct regions are discernable in the shadowgraph patterns. One is the liquid-phase wake directly downstream of the cylinder, where the value of the shadow fraction was close to zero. The second is the bubble-trapping wake region, where air bubbles were concentrated. From Figure 3(a-e), it can be seen that the liquid-phase region occurred across all Reynolds numbers for the 3.5 mm bubbles. However, the figure qualitatively shows that bubble-trapping is most evident at Reynolds numbers at and above 2,069. Similarly, Figure 2-3(f-j) qualitatively shows the occurrence of the liquid-phase region and the bubble-trapping region for the smaller bubble sizes. However, the length of the liquid-phase region appears significantly smaller compared to that of the larger bubble cases shown in Figure 2-3(a-e). Bright areas in the wake of the cylinder suggest bubble trapping occurred at a lower Reynolds number of 1,182 compared to the larger bubble cases.

The freestream conditions across the experimental flow parameters are summarized in Figure 2-4(a). As described above, freestream shadow fraction values were determined as the average across the channel width at a position of $y/D = -1.0$. The variation of shadow fraction values, one standard deviation of the mean values, is indicated by the errorbars in this plot. For the 3.5 mm bubble cases, values of the freestream shadow fraction increased with increasing air superficial velocity from $j_g = 0.06$ m/s to $j_g = 0.60$ m/s. Overall, the shadow fraction decreased as the liquid Reynolds number increased, which is expected given that the higher liquid flow rate

should cause a decrease in void fraction for a constant air flow rate. For the 0.53 mm bubbles, the freestream shadow fraction was much higher than the 3.5 mm bubbles at the same air superficial velocity of 0.06 m/s. Their shadow fraction values were greater as the bubble concentrations for these cases were much higher.

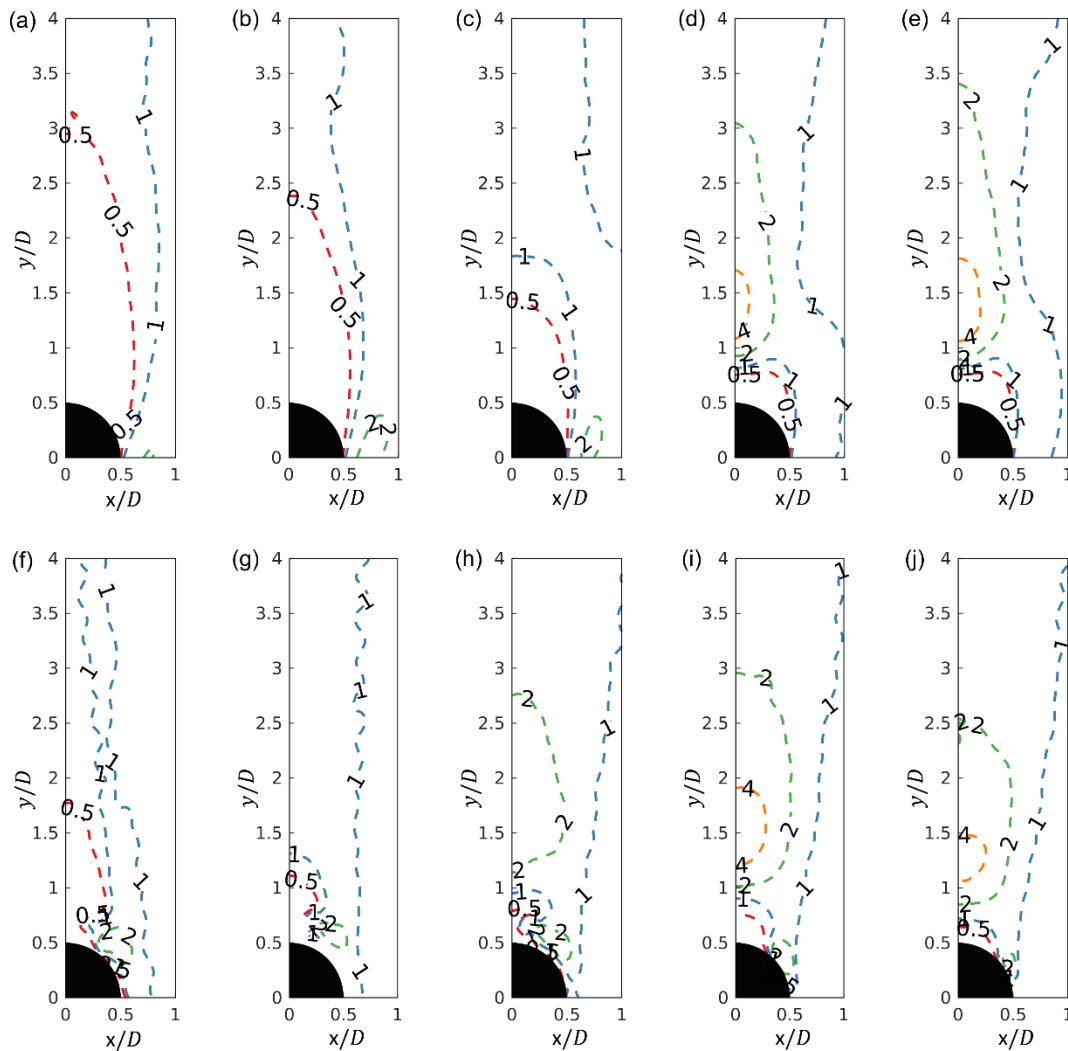


Figure 2-5: Contour plots of void fraction ratio (α/α_∞) at $j_g = 0.36$ m/s for the 3.5 mm bubbles at liquid Reynolds numbers of (a) $Re = 99$ (b) $Re = 197$ (c) $Re = 1,182$ (d) $Re = 2,069$ and (e) $Re = 2,956$ and at $j_g = 0.06$ m/s for the 0.53 mm bubbles at liquid Reynolds numbers of (f) $Re = 296$ (g) $Re = 591$ (h) $Re = 1,182$ (i) $Re = 2,069$ and (j) $Re = 2,956$.

The same data in shown in Figure 2-4(a) but corrected to freestream void fraction values are plotted as a function of superficial air velocity and the liquid Reynolds numbers in Figure 2-4(b). The overall trend of the data was similar to that of the freestream shadow fraction, where the void fraction increased with increasing air superficial velocity and decreased with the Reynolds number. However, the freestream void fractions for the 0.5 mm bubbles are now shown to be similar to those for the 3.5 mm bubbles at the same air superficial velocity ($j_g = 0.06$ m/s). This result gives some credibility to the correlation procedure, as these experimental cases should have similar void fractions.

The same void distributions presented in Figure 2-3 are shown in Figure 2-5 as contour plots of the void fraction. Here the void fraction was normalized by its freestream value (α/α_∞), which enables the comparison of void fractions across the different flow conditions. Void fraction distributions for $\alpha/\alpha_\infty = 0.5, 1, 2,$ and 4 for the 3.5 mm bubble cases with an air superficial velocity of $j_g = 0.36$ m/s are shown in Figure 2-5(a-e). As the Reynolds number increases, the region where the void fraction was less than half of the freestream decreases in size. At the highest Reynolds numbers tested ($Re = 2,069$ and $2,956$), a strong accumulation of bubbles occurred, and the void fraction exceeded four times the freestream value. Similarly, void fraction distributions for the 0.53 mm air bubbles with an air superficial velocity of $j_g = 0.06$ m/s are shown in Figure 2-5(f-j). The strongest accumulation of bubbles also occurred at $Re = 2,069$ and $2,956$; however, there was also a region of bubble accumulation at $Re = 1,182$ where the void fraction ratio exceeded two, as shown in Figure 2-5(h).

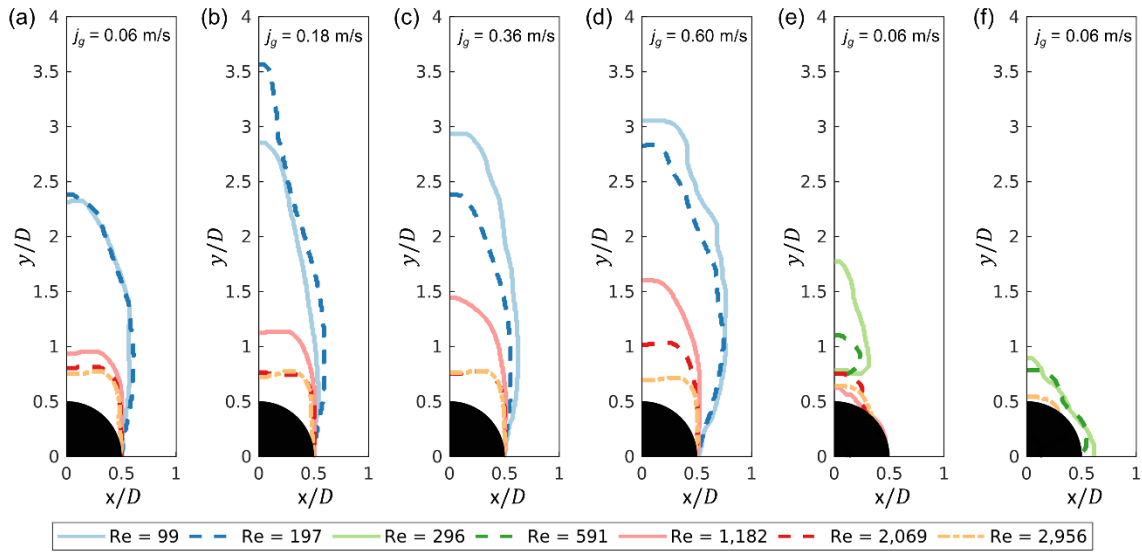


Figure 2-6: Liquid-phase region contours behind the cylinder with the 3.5 mm bubbles for (a) $j_g = 0.06$ m/s, (b) $j_g = 0.18$ m/s, (c) $j_g = 0.36$ m/s, (d) $j_g = 0.60$ m/s; (e) with the 0.53 mm bubbles for $j_g = 0.06$ m/s, and (f) with the 0.48 mm bubbles for $j_g = 0.06$ m/s.

2.2.2 Liquid-Phase Region

Isocontours in the cylinder wake where the void fraction was one-half of the freestream value ($\alpha/\alpha_\infty = 1/2$) are shown in Figure 2-6, plotted at different Reynolds numbers for different bubble sizes and air superficial velocities. Regions within the plotted isocontours have depleted bubble concentration and are representative of the liquid-phase wake region. The liquid-phase wake regions for the 3.5 mm bubbles at various air superficial velocities are shown in Figure 2-6(a-d), whereas Figure 2-6(e) and 2-6(f) show the liquid-phase wake region for the 0.53 mm and 0.48 mm bubbles with $j_g = 0.06$ m/s. Overall, the length of the liquid-phase wake decreased as the Reynolds number increased regardless of the air superficial velocity. At the superficial velocity of $j_g = 0.18$ m/s and Reynolds numbers of 99 and 197 (Figure 2-6(b)), the apparent increase in liquid-phase region length was due to a small increase in freestream shadow fraction values, which can also be seen in Figure 2-4(a). This was likely due to a slight non-uniformity in the

bubble injection conditions for this test case, though this difference was within the margins of uncertainty (Figure 2-4(a)). It is noticeable that the size of the liquid-phase region for $Re \leq 1,182$ consistently increased as the air superficial velocity increased, except for the discrepancy described above for $Re = 197$. In contrast, the size of the liquid-phase region at $Re = 2,069$ or $Re = 2,956$ remained largely independent of air superficial velocity except at $j_g = 0.60$ m/s (Figure 2-6(d)), where a slightly larger region is observed at $Re = 2,069$. At these higher Reynolds numbers, the liquid region existed primarily as a thin layer directly downstream of the cylinder.

Bubble size had a significant effect on the liquid-phase region, where the length was much shorter at all Reynolds numbers for the 0.53 and 0.48 mm bubble cases, as shown in Figure 2-6(e) and 2-6(f). Increasing the Reynolds number for these cases from $Re = 296$ to $Re = 591$ caused a decrease in the length of the liquid-phase region, consistent with the 3.5 mm bubble cases; however, the liquid-phase region became so thin that it was largely undetectable for Reynolds numbers above 1,182 (Figure 2-6(e-f)).

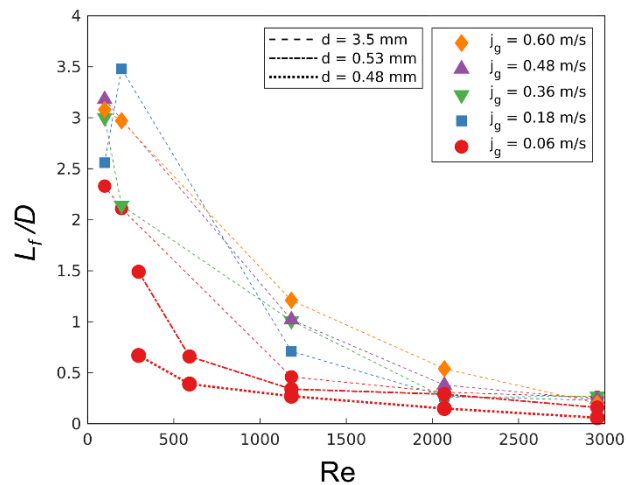


Figure 2-7: Length of the liquid-phase region as a function of Reynolds number for all air superficial velocities and bubble sizes.

The length of the liquid-phase region as a function of the Reynolds number is plotted in Figure 2-7. For all cases except the exception described above for $j_g = 0.18$ m/s, the length of the liquid-phase wake decreased with increasing Reynolds number. For the 3.5 mm bubble cases, the length of the liquid-phase region ranged from $L_f/D = 0.3 - 3.5$, depending on the Reynolds number. For the 0.53 mm and 0.48 mm bubble cases, the length of the liquid-phase region had a maximum of $L_f/D = 1.5$ and $L_f/D = 0.7$, respectively. These maximum lengths occurred at the lowest Reynolds number tested ($Re = 296$). At higher Reynolds numbers, the length for both of the small bubble cases rapidly decreased. At a Reynolds number of $Re = 2,956$, the length of the liquid-phase region for all bubble sizes and air superficial velocities was consistently less than 0.3 cylinder diameters, which suggests that the liquid-phase region remains thin at high Reynolds numbers where it is largely insensitive to bubble size. The thinnest liquid-phase wake observed during the experiments was approximately $L_f/D = 0.1$, observed for a Reynolds number of 2,956 with the 0.48 mm bubbles. Regardless of bubble size, superficial air velocity, or liquid Reynolds number, the start of the liquid-phase wake was fixed to the cylinder surface.

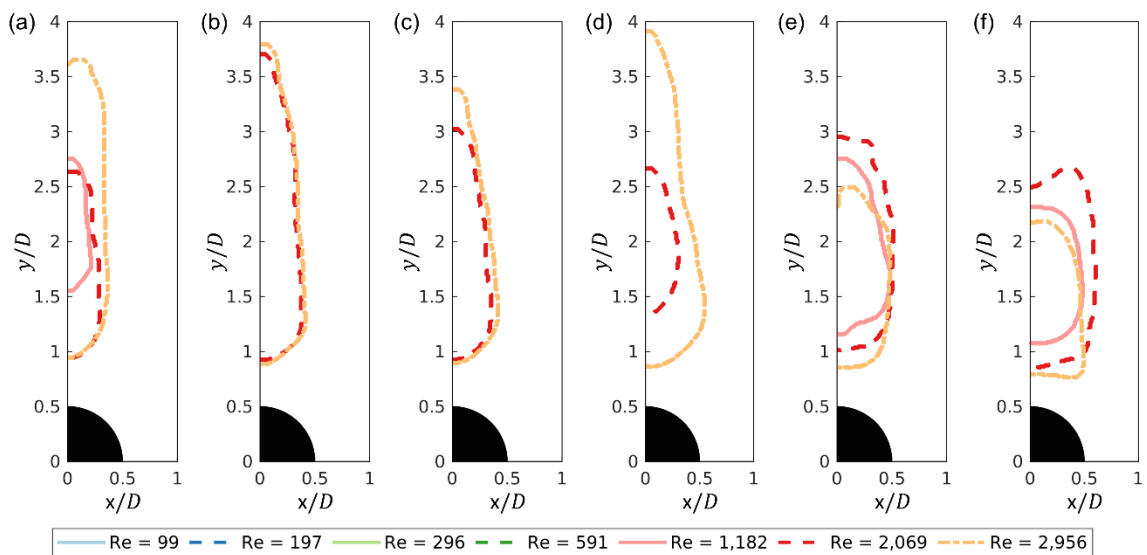


Figure 2-8: Contours showing the bubble trapping region behind the cylinder for the 3.5 mm bubbles and (a) $j_g = 0.06$ m/s, (b) $j_g = 0.18$ m/s, (c) $j_g = 0.36$ m/s, (d) $j_g = 0.60$ m/s, (e) the 0.53 mm bubbles and $j_g = 0.06$ m/s, and (f) the 0.48 mm bubbles and $j_g = 0.06$ m/s.

2.2.3 Bubble-Trapping Region

For discussion, the bubble trapping region was defined as the area where the void fraction was concentrated by more than a factor of two ($\alpha/\alpha_\infty > 2$). The bubble-trapping regions are plotted using isocontours in Figure 2-8. For the 3.5 mm bubbles shown in Figure 2-8(a-d), the bubble trapping region occurred when the Reynolds number was greater than 2,069, regardless of the air superficial velocity. For this and higher Reynolds numbers ($Re = 2,069$ and $2,956$), the bubble trapping region primarily began at $y/D = 1$, except for the $Re = 2,069$ and $j_g = 0.60$ m/s (Figure 2-8(d)) where the liquid-phase region extended further downstream (see Figure 2-6(d)). For the air superficial velocity of $j_g = 0.06$ m/s, the bubble-trapping region was also observed at a Reynolds number of 1,182. Consequently, these flow conditions may represent a transition in the occurrence of the bubble-trapping region when the bubble diameter is ~ 3.5 mm. Overall, the bubble-trapping region started at $y/D \approx 0.9 - 1.5$ and extended to $y/D \approx 2.5 - 4.0$ for the 3.5 mm bubbles, depending on the flow conditions. For the 0.53 mm bubbles and 0.48 mm bubbles in Figure 2-8(e,f), the bubble trapping wake was consistently observed at $Re = 1,182$, as well as the higher Reynolds numbers. The small bubble diameters resulted in a bubble-trapping region that was similar in size and shape across all flow conditions, where the bubble-trapping wake began at $y/D \approx 0.8 - 1.1$ and extended to $y/D \approx 2.2 - 3.0$.

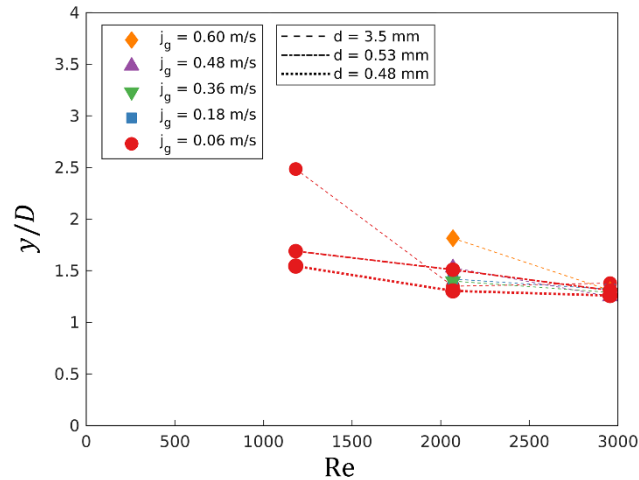


Figure 2-9: The downstream location of a maximum void fraction within the bubble-trapping region as a function of Reynolds number for all air superficial velocities and bubble sizes.

The location of the maximum bubble concentration as a function of the Reynolds number is shown in Figure 2-9. At the highest Reynolds number of 2,956, the maximum bubble concentration was located between $y/D \approx 1.3 - 1.5$, regardless of bubble size or air superficial velocity. At lower Reynolds numbers, the location of maximum bubble concentration was more dependent on flow conditions, ranging from $y/D \approx 1.3 - 2.0$ for all cases investigated except for the transitional case of $Re = 1,182$ and $j_g = 0.06$ m/s, where its location was $y/D \approx 2.5$. Considering the transitional case also had a smaller bubble-trapping region (Figure 2-8(a)), the bubble-trapping at $Re = 1,182$ and $j_g = 0.06$ m/s for the 3.5 mm bubbles was likely not as strong as the trapping that occurred at the higher Reynolds numbers and air superficial velocities.

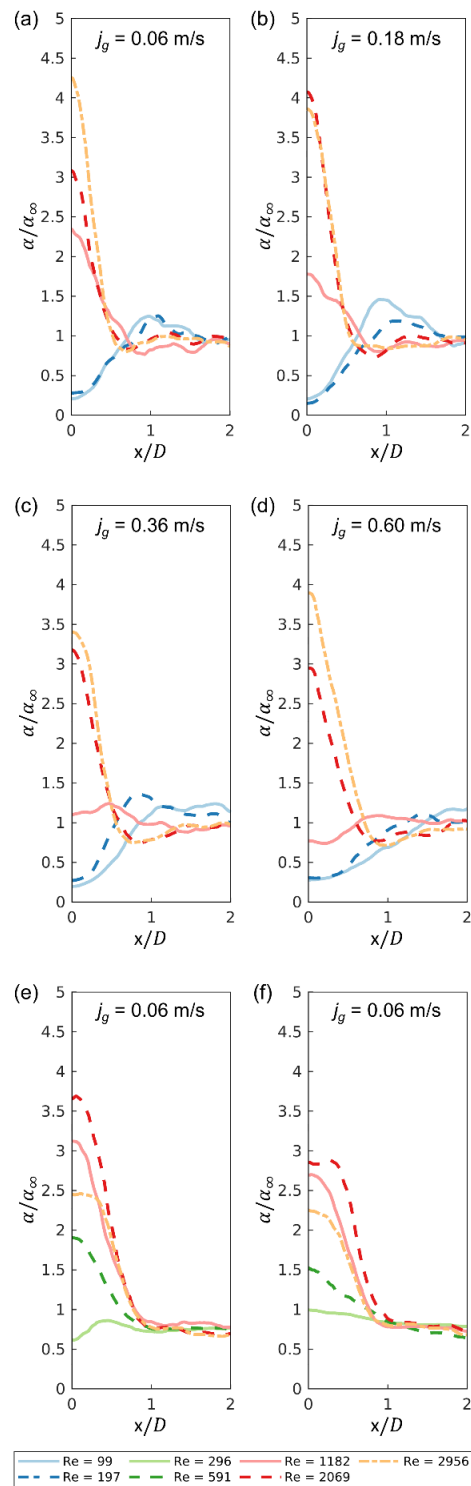


Figure 2-10: Void fraction ratio at a downstream location of $y/D = 1.5$ for the 3.5 mm bubbles and (a) $j_g = 0.06$ m/s, (b) $j_g = 0.18$ m/s, (c) $j_g = 0.36$ m/s, (d) $j_g = 0.60$ m/s, (e) the 0.53 mm bubbles and $j_g = 0.06$ m/s, and (f) the 0.48 mm bubbles and $j_g = 0.06$ m/s.

The void fraction ratio (α/α_∞) at $y/D = 1.5$ plotted from $x/D = 0$ to $x/D = 2.0$ is shown in Figure 2-10. The location of $y/D = 1.5$ was selected as it was close to the maximum void fraction ratios for the majority of the experimental cases (Figure 2-9). When the Reynolds number was greater than 2,069 for the 3.5 mm bubble cases (Figure 2-10(a-d)), the void fraction ratio had a peak greater than 3.0 at all air superficial velocities, which suggests a strong and consistent accumulation of bubbles. In contrast, for the Reynolds number of 1,182, the peak of the void fraction ratio started above 2.0 and decreased to 0.8 as the air superficial velocity increased. However, when the Reynolds number was smaller than 1,182, the void fraction ratio behind the cylinder was less than 0.5, suggesting that $y/D = 1.5$ was within the liquid-phase region. In Figure 2-10(e,f), the peak of the void fraction ratio for the 0.53 and 0.48 mm bubbles was greater than 2 for all conditions where the Reynolds number was greater than 1,182, indicating that significant bubble accumulation occurred at $y/D = 1.5$. For the Reynolds number of 591, the void fraction ratio peak was slightly less than 2.0 but greater than 1.5 for both cases. This accumulation was not as concentrated compared to the accumulation detected at higher Reynolds numbers; however, this result further confirms that the smaller bubbles started to accumulate at lower Reynolds numbers compared to the 3.5 mm bubbles.

2.3 Discussion and conclusion

An experimental investigation was conducted to characterize the wake and void fraction distribution around a cylinder in a two-phase bubbly crossflow. The flow was characterized across a range of flow conditions, including liquid Reynolds numbers from 99 to 2,956, air superficial velocities from 0.06 to 0.60 m/s, and average bubble sizes of 0.48 mm, 0.53 mm, and 3.5 mm. The spatial variation of void fraction was determined through high-speed imaging and calibrated shadow fraction measurements.

Across all flow parameters investigated, a liquid-phase wake occurred directly downstream of the cylinder regardless of the Reynolds number, air superficial velocity, and bubble diameter. The length of the liquid-phase wake decreased with increasing Reynolds number. However, the length of the wake increased with the air superficial velocity for Reynolds below 2,069. The length and shape of the liquid-phase wake were significantly affected by the mean bubble diameter, with smaller bubbles resulting in smaller liquid-phase wakes.

A bubble-trapping region occurred downstream of the liquid-phase wake for Reynolds numbers above 1,182 for the 0.48 mm and 0.53 mm bubbles and above 2,069 for the 3.5 mm bubbles. The investigation with the small bubble size provides important evidence that the bubble-trapping region in the environment of a two-phase heat exchanger could potentially occur at a lower Reynolds number as its typical bubble size is less than 0.61 mm. The Reynolds number of 1,182 exhibited transitional behavior as bubble trapping was observed for the 3.5 mm bubbles at this Reynolds number for air superficial velocities of $j_g = 0.06$ m/s but not at higher air flowrates. Based on the location of its maximum void fraction values, the center of the bubble-trapping region reached a consistent downstream location of $y/D \approx 1.5$ as the Reynolds number increased for all bubble sizes. The transition from a non-trapping wake to a bubble-trapping region was indicated by a peak in a void fraction that became more concentrated and located at

$y/D = 1.5$ as the Reynolds number increased. Further investigation is needed to explain why bubble trapping occurred at Reynolds numbers of 2,069 and above regardless of the mean bubble diameter and air flow rate, whereas the bubble trapping occurred only at lower Reynolds numbers for small bubbles and low air superficial velocities.

3. Explaining the Physics of the Bubble-Trapping Region

The previous chapter reported the existence of the liquid-phase region and the bubble-trapping region for an upward liquid-gas flow behind a cylinder. In this chapter, the formation of the bubble-trapping wake region downstream of a cylinder in an upwards liquid-gas crossflow was studied experimentally to identify the forces leading to the bubble-trapping region. High-speed images of the two-phase flow were used to characterize the liquid-phase wake region and the bubble-trapping wake region as a function of liquid cylinder Reynolds number, bubble size, bubble velocity, liquid velocity, and void fraction ratio. For the measurement of time-averaged bubble trajectories, Particle Tracking Velocimetry (PTV) and Particle Image Velocimetry (PIV) algorithms were implemented. In addition, the time-averaged velocity of the continuous liquid phase and discrete bubbles were captured simultaneously using PTV and Particle Shadow Image Velocimetry (PSIV), which enabled the calculation of hydrodynamic forces acting on the bubbles in the flow. In the following chapter, the forces that lead to trapping are discussed in detail, and the conditions necessary for the occurrence of bubble trapping are defined. The research material in this chapter is available in the publication [62].

3.1 Method

The same experimental facility was used for the time-averaged PTV and PIV measurements for the experimental conditions mentioned in Table 2-1. For the PSIV analysis, neutrally-buoyant flow tracers were injected at $Re = 2,956$ and $j_g = 0.06$ m/s. More details about the PTV, PIV, and PSIV analyses are available in the following sections.

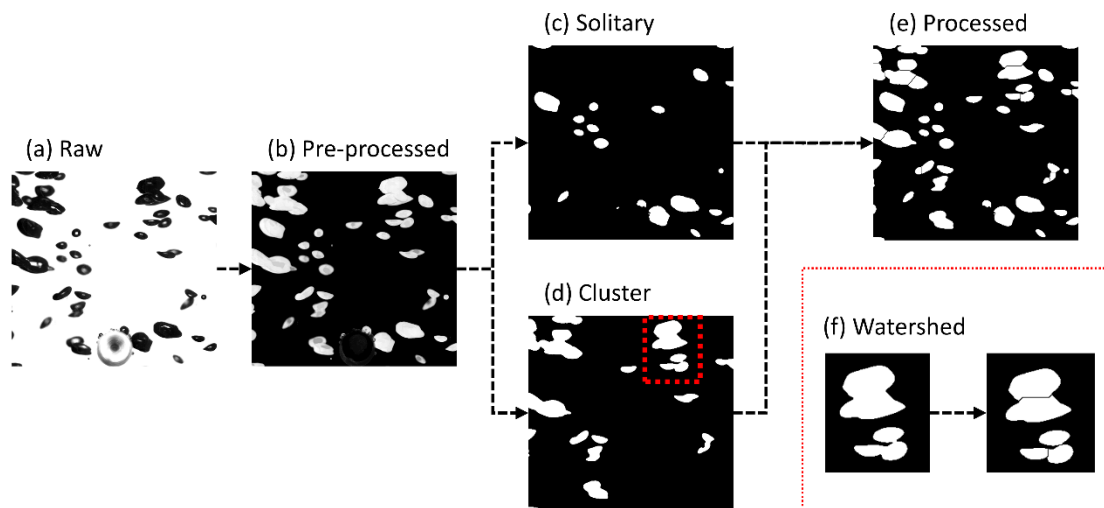


Figure 3-1: Representation of imaging process: (a) raw images, (b) pre-processed images with background removal, (c) solitary bubble images, (d) cluster bubble images, (e) processed images, and (f) watershed transformation for cluster bubble images

3.1.1 Image Acquisition and Processing

The high-speed camera captured the movement of the liquid-gas flow around the cylinder for 3.142 s at a frame rate of 10,000 fps for each case listed in Table 2-1. The raw high-speed images (e.g. Figure 3-1(a)) were pre-processed as 8-bit greyscale images with inverted intensity. This intensity inversion created bright bubble images on dark backgrounds, which assisted in the pre-processing and bubble tracking algorithms. The background was then removed by subtracting the

minimum grayscale intensity at each pixel (calculated from the entire video time series). After this step, the pre-processing code detected holes in the grayscale images by finding regions of dark pixels surrounded by light pixels within the circular bubble shapes. These holes were replaced with grayscale values with an average of the neighboring grayscale values in the horizontal, vertical, and diagonal directions. Once completed, this procedure resulted in the pre-processed image, as shown in Figure 3-1(b).

Particle Tracking Velocimetry

Figure 3-1(b) shows a representative pre-processed image of the bubbly flows obtained in this experiment. Little to no bubble coalescence occurred in the test section, but the images of many bubbles did overlap due to the non-negligible depth of the flow channel. To accurately track individual air bubbles and calculate bubble size distributions, it was necessary to segregate overlapping bubble projections into smaller individual air bubbles. From the pre-processed images, solitary and cluster air bubbles were distinguished and binarized based on an automatic global image threshold [61]. Lau *et al.* [63] classified bubbles into solitary bubbles and cluster bubbles by using roundness, which is defined as

$$Ro = \frac{S}{\sqrt{4\pi A}}, \quad (3-1)$$

where S is the bubble perimeter and A is the bubble projected area. Lau *et al.* [63] found solitary bubbles to have roundness values of less than $Ro < 1.25$ based on their empirical analysis.

Similarly, trial and error on the acquired high-speed images for the current study indicated that the same criterion could distinguish the two groups of air bubbles. An example of segregation is shown in Figure 3-1(c) (solitary bubbles) and Figure 3-1(d) (cluster bubbles).

Once the air bubbles in clusters were distinguished, a watershed transformation, based on the flooding algorithm created by Meyer [64] and used by others to break up clusters of air bubbles [34,63], was applied to determine the dividing line between individual bubbles and bubbles in a cluster. Along with the watershed transformation, the extended-minima transformation [65] was applied to prevent over-segmentation of the cluster bubbles. The watershed transformation uses surface topography to find the center of individual air bubbles. However, the watershed transformation tends to over segment a cluster bubble into many non-physical fine bubbles if multiple points of minimum intensity exist in the cluster bubble image. Instead, the extended-minima transformation filters out the minimum peaks and creates a mask of distinct minima [65]. An example of the resulting segmentation is shown in Figure 3-1(f). After the watershed transformation with the extended-minima transformation was applied, images of solitary bubbles and segmented cluster bubbles were combined to restore the entire image, as shown in Figure 3-1(e). Once this procedure was completed, the processed images were used to calculate bubble size distribution and perform the PTV.

An open-source MATLAB program for PTV and PIV, PRANA [66], was used to calculate the moving trajectories of air bubbles from high-speed images. PTV was used to track the large bubbles, which were adequately dispersed from one another in the flow. First, bubbles were identified using a single-value threshold binarization [67]. Bubble size was then determined based on the geometric information of these binary projections. With the knowledge of the location and size of the bubbles, tracking was conducted by matching bubbles from two consecutive images based on the initial location, estimated location, greyscale intensity, and bubble size. The equivalent bubble diameter was defined as, $d = \sqrt{4A/\pi}$, where A was the area of the bubble image projection.

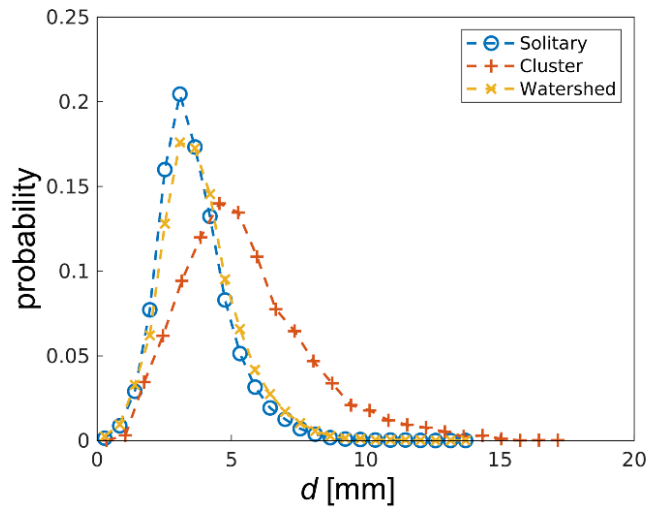


Figure 3-2: Bubble size distribution of images for air bubbles in solitary (Figure 3-1(c)), cluster (Figure 3-1(d)), and watershed (Figure 3-1(f)) when $Re = 99$ and $j_g = 0.18$ m/s.

Figure 3-2 shows representative bubble size distributions of solitary bubbles (Figure 3-1(c)), the cluster bubbles before the watershed segmentation (Figure 3-1(d)), and the cluster bubbles after segmentation (Figure 3-1(f)) for experimental flow conditions of $Re = 99$ and $j_g = 0.18$ m/s. While the bubble size distribution of the solitary bubbles and the cluster bubbles before segmentation have a clear distinction, the segmentation process largely recovers the size distribution of the solitary bubbles. In this study, the mean of equivalent bubble diameter in freestream, d_∞ , was calculated based on the bubble size distribution of the solitary bubbles upstream of the cylinder. The record of d_∞ in all experiments is available in Table 2-1.

Time-averaged bubble velocities were analyzed on a fixed grid throughout the FOV using zonal statistics. For consistency with the PIV procedure, described in the following section, velocities were defined on a 24 by 24 pixel grid, which corresponded to a 32 by 32-pixel sub-windows with 25% overlap centered over each grid point. The time-averaged bubble velocity at each grid point was determined by averaging the velocity of all bubbles that traveled through the corresponding sub-window during the data acquisition period. To achieve a 95% confidence

interval and a 5% margin of error on the average bubble velocity, a zone with fewer than 384 bubble observations was discarded due to low uncertainty in the average bubble velocity. The threshold was determined based on the total number of pixels in each sub-window and the total number of images. This step ensured that bubble velocities were not reported where there was little or no bubble movement in the flow. Despite the use of 30,142 images, there were some locations (*e.g.*, in the liquid-phase wake directly behind the cylinder) where bubble velocities were undefined.

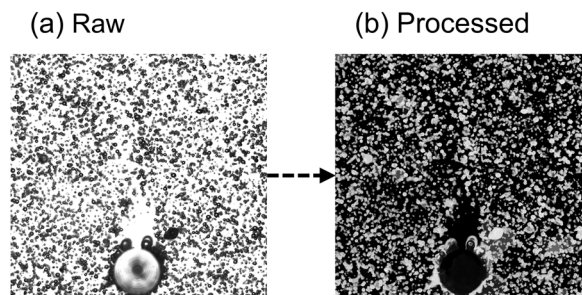


Figure 3-3: Image processing procedure for PIV measurements to determine small bubble velocities.

Particle Image Velocimetry

The bubbles that formed with the isopropanol solutions were much smaller and more numerous than the pure water cases (*e.g.*, Figure 3-3(a)) and were not dispersed sufficiently to track each individual bubble. Instead, the small bubble cases were analyzed using a PIV approach, where the average bubble velocity at a location was determined by cross-correlating bubble motion in sub-windows rather than by tracking individual bubbles. The grayscale inversion and background subtraction steps of the pre-processing algorithm were first applied (Figure 3-3(b)), then a two-pass cross-correlation with a second-order discrete window offset was

used to compute the ensemble velocity field over the entire set of images [66,68,69]. The first pass was applied to a grid of 128 pixels by 128 pixels with 25% window overlap and the second pass used a sub-window size of 32 pixels by 32 pixels with 25% overlap for consistency with the PTV analysis described above. Throughout the PIV analysis, a static processing mask around the acrylic cylinder was applied to exclude the cylinder body from the analysis.

Particle Shadow Image Velocimetry

To measure the liquid velocity in a subset of the large bubble experiments, neutrally buoyant flow tracers (White Polyethylene Microspheres, 1.00g/cc, 250-300 μm , Cospheric) were injected into the bubbly flow. Their velocity was then determined using Particle Shadow Image Velocimetry (PSIV). PSIV differs from PIV in that particle shadows from backlighting, rather than bright particle images from scattered laser light, are used to track a fluid flow [70–73]. Even though PIV measurements in bubbly flows are possible to determine liquid velocities [74], the implementation of PSIV with the current bubble visualization setup was less complicated and complementary to the bubble shadowgraph tracking methods described above. One drawback of PSIV compared to PIV, which typically employs a thin laser sheet for illumination, is that the shadows of all particles within the imaging depth are visualized. Particles within a narrow plane can be isolated for improved two-dimensional fluid measurements if a narrow depth of field (DOF) is used [70,73]. The DOF for the current configuration was measured by calculating the clarity index [75] to be less than 4 mm, which is suitable for PSIV in a bubbly flow [72]. In addition, in-focus particles were identified by comparing gradients of the first Gaussian kernel between particles [75]. As the PIV algorithm is sensitive to a slight change in image intensity due to Fast-Fourier-Transformation (FFT), out-of-focus particles with low clarity index values were removed to improve the overall PSIV correlation.

The imaging process required a separate flow process but not too far from the previous cases (Figure 3-1 and Figure 3-3). As the images contain both air bubbles and flow tracers, images with air bubbles and images with flow tracers were separated during the pre-processing (Figure 3-1(b)). The bubble detection algorithm was modified to filter out the flow tracers when a diameter of the detected particle, a bubble or a flow tracer, is within the range of the flow tracer diameter. The image with air bubbles followed the rest of the imaging process method, as shown in Figure 3-1(b-e) for the PTV application. The images with flow tracers followed the process of out-of-focus particle removal. During the PSIV analysis, a grid of 48 pixels by 48 pixels with 50% window overlap was applied for the first pass. For the second pass, a sub-window size of 24 pixels by 24 pixels with 50% overlap was used. As used in the other PIV analysis, the static processing mask excluded the area around the acrylic cylinder.

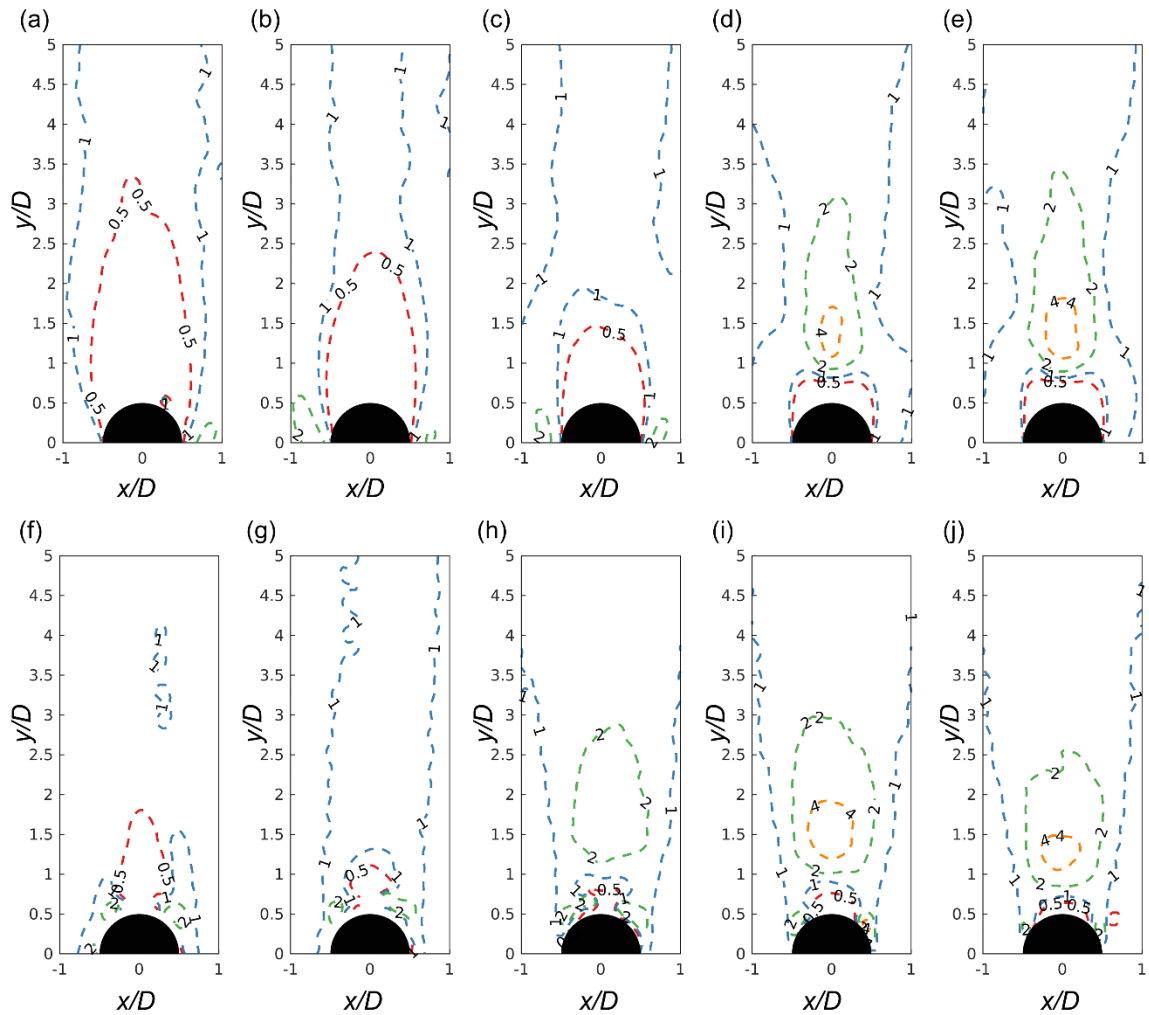


Figure 3-4: Contour plots of the void fraction ratio behind the cylinder at $j_g = 0.36$ m/s with the 3.5 mm bubbles for (a) $Re = 99$ (b) $Re = 197$ (c) $Re = 1,182$ (d) $Re = 2,069$ and (e) $Re = 2,956$ and at $j_g = 0.06$ m/s with the 0.53 mm bubbles for (f) $Re = 296$ (g) $Re = 591$ (h) $Re = 1182$ (i) $Re = 2069$ and (j) $Re = 2956$.

3.2 Result

3.2.1 Void Fraction Ratio

The patterns in void fraction ratio (α/α_∞) resulting from the large bubbles at a range of Reynolds numbers and an overall air flow rate of $j_g = 0.36$ m/s are shown in Figure 3-4(a-e). The flow patterns from the small bubbles at a range of Reynolds numbers and an air flow rate of $j_g = 0.06$ m/s are shown in Figure 3-4(f-j). In the following discussion, the liquid-phase region is the region where $\alpha/\alpha_\infty < 0.5$ and the bubble-trapping region is the region where $\alpha/\alpha_\infty > 2.0$. This definition is consistent with that used by the authors previously [53]

When the bubbles were large (~ 3.5 mm) and Reynolds numbers were less than 1,200 (Figure 3-4(a-c)), the liquid-phase region extended downstream more than one cylinder diameter. However, the size of this liquid-phase layer decreased with increasing Reynolds number. Once Reynolds numbers became greater than 2,000 (Figure 3-4(d-e)), only a very thin liquid-phase region existed just downstream of the cylinder, followed by an intense concentration of air bubbles characteristic of the bubble-trapping region. Based on the contour plots of the void fraction ratio in Figure 3-4(d-e), the center of this bubble-trapping region was around $y/D = 1.3-1.6$ [53].

For the 0.53 mm bubbles (Figure 3-4(f-j)), the liquid-phase region was smaller and extended downstream for more than one cylinder diameter only at the lowest Reynolds number (Figure 3-4(f)). The liquid-phase region became very small for Reynolds numbers at and above 1,182, where the first appearance of the bubble-trapping region occurred. The bubble-trapping region at $Re = 2,069$ (Figure 3-4(i)) and $Re = 2,956$ (Figure 3-4(j)) had a core with a void fraction ratio greater than 4.0. Even though the void fraction ratio did not reach 4.0 at $Re = 1,182$ (Figure 3-4(h)), the bubble-trapping region can be easily detected as an area with $\alpha/\alpha_\infty > 2.0$. Similar to

the large bubble cases, the region with the strongest bubble concentration was centered around $y/D = 1.3-1.6$ [53].

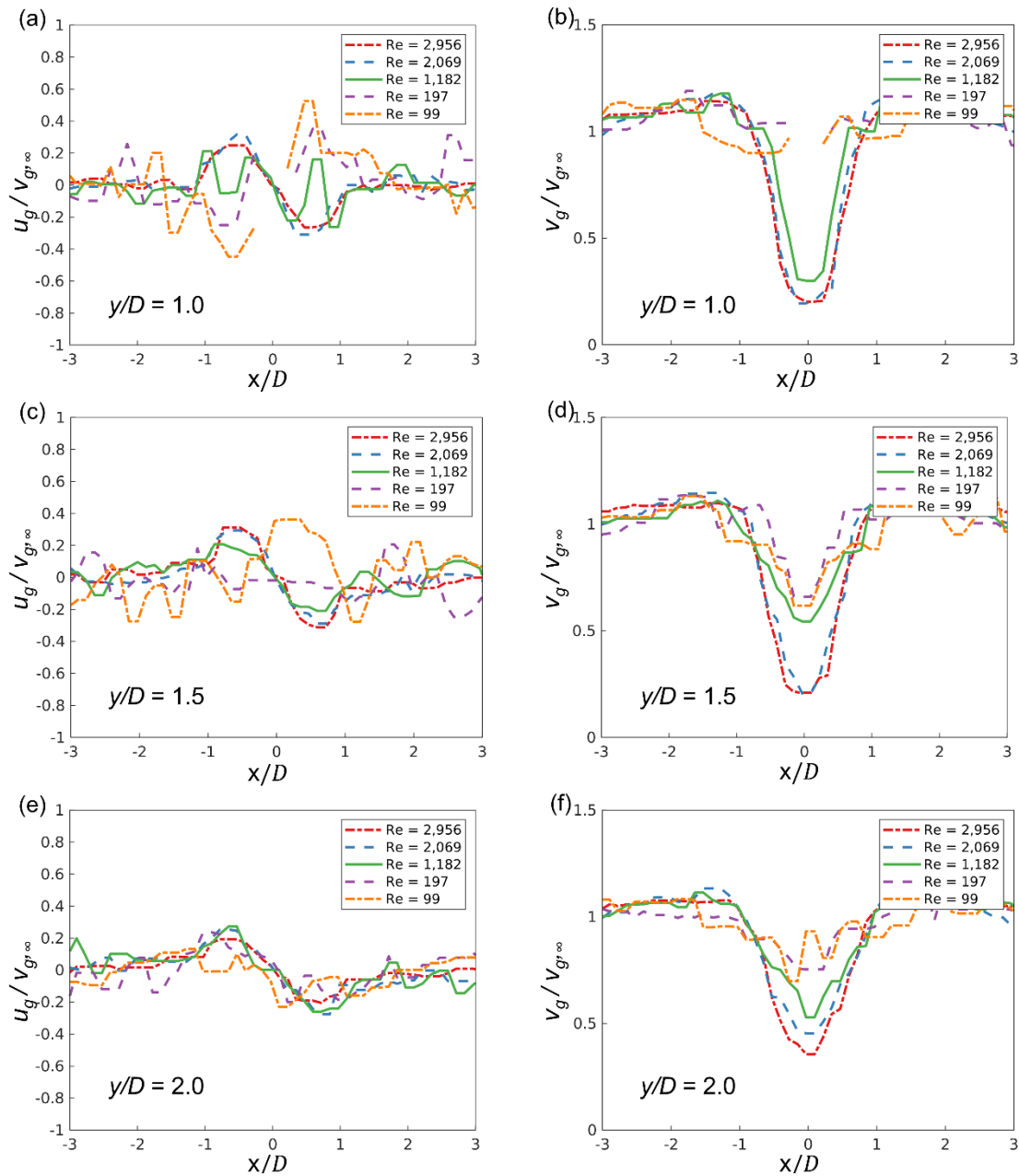


Figure 3-5: Horizontal and streamwise velocity ratio for the 3.5 mm bubble cases at $j_g = 0.36$ m/s and at $y/D = 1.0$ (a-b), $y/D = 1.5$ (c-d), and $y/D = 2.0$ (e-f).

3.2.2 Air Velocities in the Wakes

The horizontal and vertical velocity ratio, defined as $u_g/v_{g,\infty}$ and $v_g/v_{g,\infty}$, of the large bubbles at $y/D = 1.0, 1.5,$ and 2.0 are shown in Figure 3-5 for an air superficial velocity of $j_g = 0.36$ m/s. These ratios compare the time-averaged local horizontal and vertical bubble velocity, u_g and v_g , to that of the freestream vertical bubble velocity, $v_{g,\infty}$.

In general, the horizontal velocity ratio had a variation of $\pm 20\%$ of the freestream vertical bubble velocity, as shown in Figure 3-5(a,c,e). Because the origin was defined at the cylinder center, positive velocities to the left of the cylinder ($x/D < 0$) and negative velocities to the right of the cylinder ($x/D > 0$) both indicate bubble movement towards the centerline. This inward motion of the bubbles is clear at $y/D = 2.0$ (Figure 7e), where inward bubble velocities peaked at $x/D \approx \pm 0.7-0.8$. This inward bubble motion also occurred consistently at Reynolds numbers of 1,182, 2,069 and 2,956 at $y/D = 1.5$ (Figure 7c), and for Reynolds numbers of 2,069 and 2,956 at $y/D = 1.0$. At flow velocities below these Reynolds numbers, the bubble motion tends to be more random due to the weak motion of surrounding fluid from the low liquid velocities. Comparing these results to the void fraction distributions shown in Figure 3-4, it can be observed that the inward bubble motion occurs downstream of the liquid-phase region, which gets closer to the cylinder as the Reynolds number increases.

In Figure 3-5(b,d,f), the plots of the vertical velocity ratio show that there was a large decrease in the vertical velocity of air bubbles directly behind the cylinder. In Figure 3-5(b), there are some missing data for the cases of $Re = 99$ or 197 near $x/D = 0$ because of a lack of bubble observations at the given location. At $y/D = 1.0$ (Figure 3-5(b)), the bubble velocity was reduced to only about 20% of the freestream bubble velocity for $Re = 1,182; 2,069;$ or $2,956$. In addition, this largest reduction in velocity also occurred at the Reynolds numbers of 2,069 or 2,956 at $y/D = 1.5$, indicating that the bubble holdup at these locations for these conditions were similar.

However, the velocity reduction was smaller for the Reynolds numbers of 1,182, 197, and 99 at $y/D = 1.5$ and when measured further downstream at $y/D = 2.0$ for all Reynolds numbers. It seems the strongest velocity reduction in vertical direction occurred at a downstream location between $y/D = 1.0$ and $y/D = 1.5$ at the higher Reynolds numbers investigated.

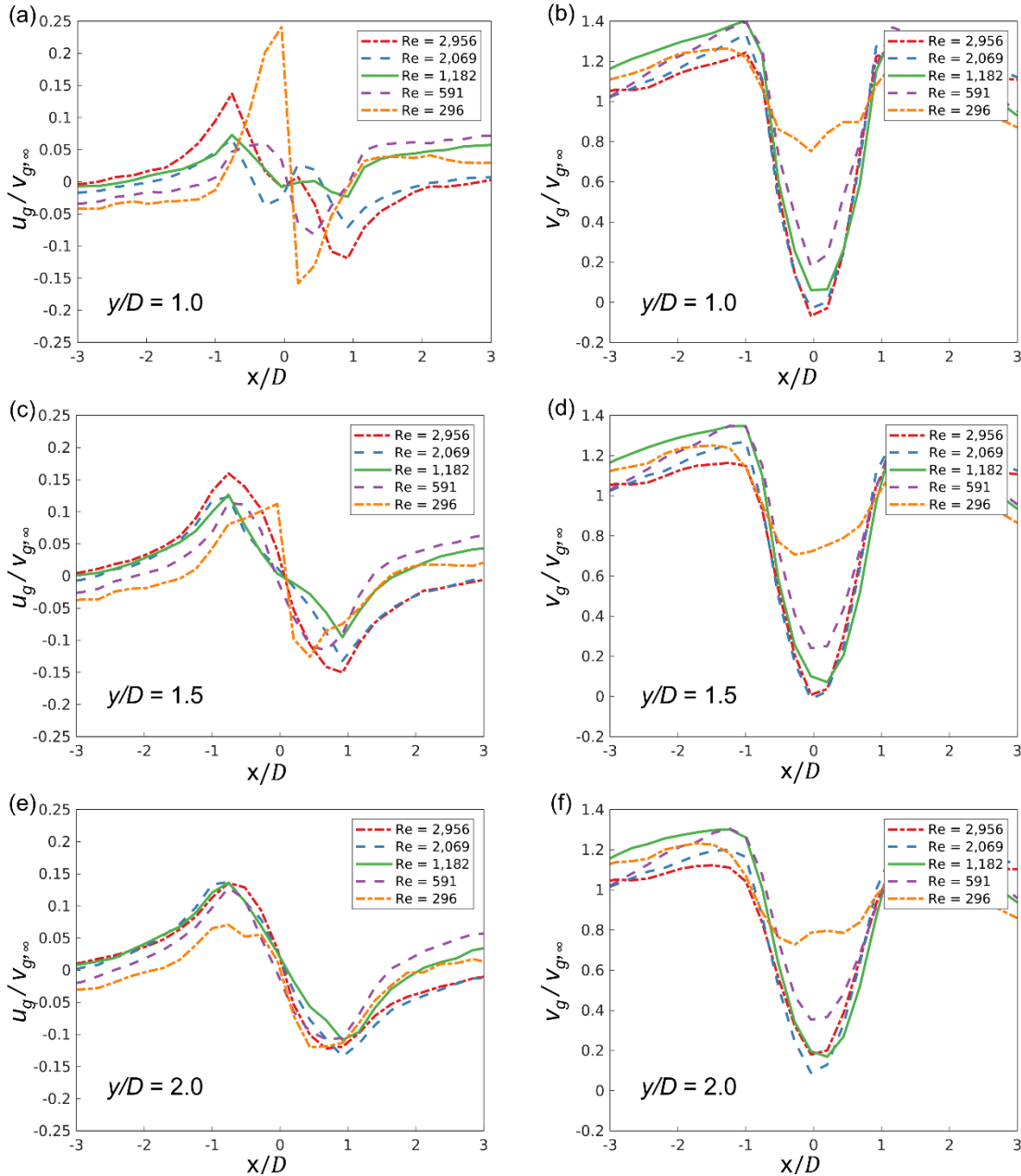


Figure 3-6: Horizontal velocity ratios (a,c,e) and vertical velocity ratios (b,d,f) for the 0.53 mm bubble cases at $y/D = 1.0$ (a-b), $y/D = 1.5$ (c-d), and $y/D = 2.0$ (e-f).

The horizontal and vertical velocity ratios at $y/D = 1.0, 1.5,$ and 2.0 are shown in Figure 3-6 for the 0.53 mm bubble cases for an air superficial velocity of $j_g = 0.06$ m/s. In general, the horizontal velocity ratio of the small bubbles in the cylinder wake had a variation of $\pm 15\%$ to its freestream vertical velocity, as shown in Figure 3-6(a,c,e). Regardless of the Reynolds number and the downstream location, the figure suggests that bubbles moved towards the centerline ($x/D = 0$) at the three downstream locations plotted ($y/D = 1.0, 1.5,$ and 2.0). Peak horizontal velocities occurred at $x/D \approx \pm 0.8-0.9$ and ranged between $\sim 5\%$ and 15% of the freestream bubble velocity at all three downstream locations, with particularly high velocities observed for the $Re = 296$ at $y/D = 1.0$ (Figure 3-6(a)). For this case, the peak horizontal bubble velocities reached $\sim 25\%$ of the freestream and were located close to the cylinder centerline at $\sim x/D = \pm 0.1$.

The small bubble vertical velocity profiles are shown in Figure 3-6(b,d,f). When the Reynolds number was low ($Re = 296$), the bubble velocities at $x/D = 0$ were reduced to $\sim 80\%$ of their freestream velocity. This result was consistent across all y/D locations plotted. However, vertical bubble velocities behind the cylinder decreased as the Reynolds number increased. In particular, the three highest Reynolds numbers investigated ($1,182, 2,069,$ and $2,956$) showed similarly small bubble velocities, indicating that the bubble trapping conditions at these locations and Reynolds numbers were similar. These cases showed bubble velocities that approached (*e.g.*, at $y/D = 1.5$) or were below zero (*e.g.*, at $y/D = 1.0$), indicating stagnant or slight downward bubble motion. For all Reynolds numbers, the bubble velocity reduction at $y/D = 2.0$ was smaller in magnitude compared to the velocities at $y/D = 1.0$ and 1.5 . Comparing results for the small bubbles to those of the larger bubbles shown in Figure 3-5, it seems that the reduction in bubble velocity was strongest at similar downstream locations (*e.g.*, between $y/D = 1.0$ and 1.5) but that this bubble holdup occurred at much lower Reynolds numbers ($Re > 521$ compared to $1,182$ for the large bubble cases).

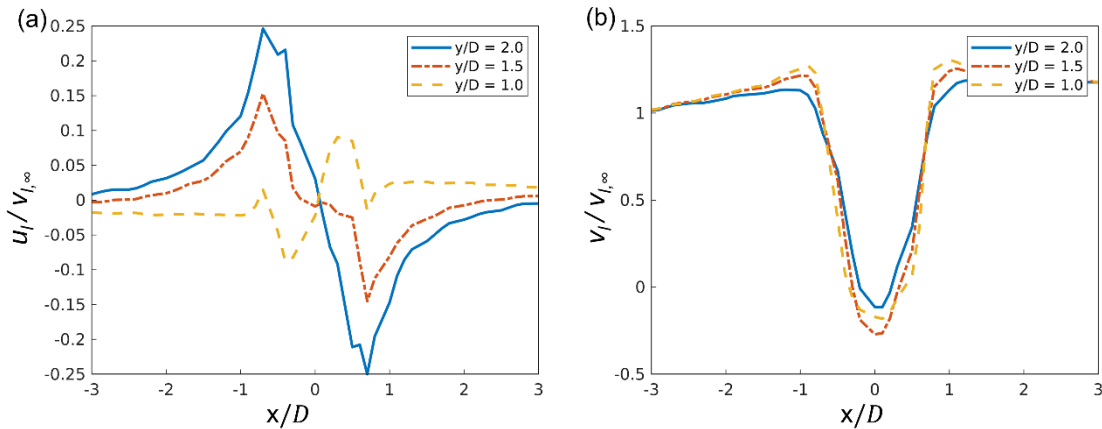


Figure 3-7: Liquid velocity ratio from the PSIV analysis at $Re = 2,956$ in (a) horizontal direction and (b) vertical direction.

3.2.3 Liquid Velocities in the Wakes

Liquid velocities measured using PSIV for the 3.5 mm bubble at $Re = 2,956$ are presented in Figure 3-7, presented as the horizontal velocity ratio ($u_l / v_{l,\infty}$) and vertical velocity ratio ($v_l / v_{l,\infty}$) at $y/D = 1.0, 1.5,$ and 2.0 . These measurements were performed at a Reynolds number of 2,956 since the strongest bubble trapping was observed for these conditions. The largest horizontal liquid velocities towards the centerline occurred at $y/D = 2.0$, as shown in Figure 3-7(a). However, the negative liquid velocities where $x/D < 0$ and positive velocities where $x/D > 0$ in the figure show that the liquid flow traveled in away from the centerline at $y/D = 1.0$. On the other hand, Figure 3-7(b) shows that there was a strong reduction of vertical liquid velocity at all downstream locations. At $x/D = 0$, all downstream locations also showed the existence of negative (*i.e.*, downward) vertical liquid velocities. Both the horizontal and vertical velocity components in Figure 3-7(a) and (b) suggest the existence of a counter-rotating vortex pair, which drew liquid inward at $y/D \gtrsim 1.5$, downward along $x/D = 0$, and then outward very near the cylinder at $y/D \approx 1.0$. In contrast to this motion, the large and small bubbles at this

Reynolds number moved only inward towards the centerline, regardless of the downstream location (see Figure 3-5(a,c,e) and Figure 3-6(a,c,e)). Subsequent force analysis of this two-phase flow is presented in the following section to describe the reason for this bubble motion.

3.3 Discussion

In this chapter, force analysis of the bubbles in the flow is used to present a bubble-trapping parameter, which can be used to predict the occurrence of bubble trapping behind a bluff body in a liquid-gas flow.

3.3.1 Force Balance Equation

The forces acting on each bubble as it moved around the cylinder were evaluated to better describe the bubble-trapping phenomenon. The governing equation of bubble motion was constructed in terms of the added-mass (**A**), pressure gradient (**P**), lift (**L**), drag (**D**), and buoyancy (**B**) forces [30,31,76]. Using the Lagrangian method, the force balance equation on an individual bubble is written as,

$$\vec{F} = \vec{F}_A + \vec{F}_p + \vec{F}_L + \vec{F}_D + \vec{F}_B . \quad (3-2)$$

The five force components in Eq. (3-2) are defined as [30,31,76]:

$$\vec{F}_A = C_A \rho_l V \frac{D\vec{u}_l}{Dt} , \quad (3-3)$$

$$\vec{F}_p = \rho_l V \frac{D\vec{u}_l}{Dt} , \quad (3-4)$$

$$\vec{F}_L = C_L \rho_l V (\vec{u}_l - \vec{u}_g) \times (\nabla \times \vec{u}_l) , \quad (3-5)$$

$$\vec{F}_D = \frac{3C_D}{4d} \rho_l V |\vec{u}_l - \vec{u}_g| (\vec{u}_l - \vec{u}_g) , \quad (3-6)$$

$$\overline{F}_B = (\rho_g - \rho_l)V\overline{g}, \quad (3-7)$$

where $D\overline{u}_l / Dt$ is the material derivative of the liquid velocities. In addition, ρ_l and ρ_g are the density of liquid and gas phases, \overline{u}_l and \overline{u}_g are the local velocity of liquid and gas phases, V is the volume of the bubble, d is the bubble diameter, and C_A , C_L , and C_D are the coefficients of added-mass, lift, and drag, respectively. After applying the ensemble average of the equation, the time-averaged force balance equation becomes

$$\begin{aligned} \overline{\overline{F}} = & C_A \rho_l V \overline{u}_l \cdot \nabla \overline{u}_l + \rho_l V \overline{u}_l \cdot \nabla \overline{u}_l + C_L \rho_l V (\overline{u}_l - \overline{u}_g) \times (\nabla \times \overline{u}_l) + \\ & \frac{3C_D}{4d} \rho_l V |\overline{u}_l - \overline{u}_g| (\overline{u}_l - \overline{u}_g) + (\rho_g - \rho_l)V\overline{g} \end{aligned} \quad (3-8)$$

The added-mass force, the first term on the right-hand side (RHS) of Eq. (8), is induced by the acceleration of the liquid around the bubble. The inertial force of the bubbles was approximated by the added-mass force, given that the air bubbles had negligible mass relative to the surrounding liquid water [77]. An added-mass coefficient of $C_A = 0.5$ is commonly used for the spherical air bubbles [50]. For ellipsoidal air bubbles, the added-mass coefficient can be calculated as $C_A = (E \cos^{-1} E - \sqrt{1 - E^2}) / (E^2 \sqrt{1 - E^2} - E \cos^{-1} E)$ for oblate spheroids ($E < 1$) and $C_A = (E \ln(E + \sqrt{E^2 - 1}) - \sqrt{E^2 - 1}) / (E^2 \sqrt{E^2 - 1} - E \ln(E + \sqrt{E^2 - 1}))$ for prolate spheroids ($E > 1$) where E represents the aspect ratio of the air bubbles [78]. Based on the aspect ratio measurements from the high-speed images, the added-mass coefficient was approximated as $C_A = 0.6$. The pressure gradient force, the second term on the RHS, is obtained from the pressure gradient by approximating the Navier-Stokes equation for an inviscid flow [77,79]. The lift force, the third term on the RHS, is introduced due to the velocity difference across the surface of a bubble. The lift coefficient was approximated as $C_L = 0.78$ for $EO < 0.5$ and

$C_L = 1.453 - 0.9\sqrt{Eo}$ for $0.5 < Eo < 4$ [31]. The drag coefficient, used in the fourth term on the RHS, was calculated using the following,

$$C_D = \max \left\{ \min \left(\frac{24}{Re} (1 + 0.15 Re^{0.678}), \frac{72}{Re} \right), \frac{24}{Re} (1 + 0.15 Re^{0.687}) \frac{Re^{0.55} Eo^{0.95} We^{-1.10}}{12.6} \right\}. \quad (3-9)$$

This equation was first presented by Yan *et al.* (2017) and covers a wide range of bubble sizes and spherical and non-spherical bubbles in the water.

Literature has also reported that wall lubrication force can be a significant interfacial force acting on bubbles in a two-phase flow [81–85]. The lubrication force can act in two ways in the present two-phase flow: close to solid surfaces and between interacting bubbles. Air bubbles around a solid surface get pushed away from the surface due to the liquid velocity gradient of the wall surface as the wall lubrication force. The wall lubrication force can be defined as $\overrightarrow{F_{WL}} = C_{WL} \rho_L (\overrightarrow{u_g} - \overrightarrow{u_l})^2 \vec{n} / d$, where C_{WL} is the wall lubrication coefficient and \vec{n} is the unit normal away from the wall [82,84]. Even though the wall lubrication force and its coefficient can be defined differently, depending on the flow and structure conditions [81–84], C_{WL} becomes negligible once the distance between the solid surface and the bubble is about its mean diameter [82,84]. In addition, the lubrication force which acted among the bubbles could have prevented the immediate bubble coalescence. During the experiments, the bubble coalescence rarely occurred as a thin film of liquid between the two bubble surfaces could have resulted in a repelling force against the air bubbles. The lubrication force could have affected the bubble coalescence, breakage rates, and bubble induced turbulence [85]. However, the lubrication force is neglected in the analysis due to the low void fraction (less than 1%). In addition, the accurate measurement of velocity gradients around the cylinder surface was restricted due to the image resolution of the imaging acquisition configuration. As the current force balance analysis focuses

on the wakes around the cylinder not on the surface around the cylinder, the wall lubrication force shall be minimum.

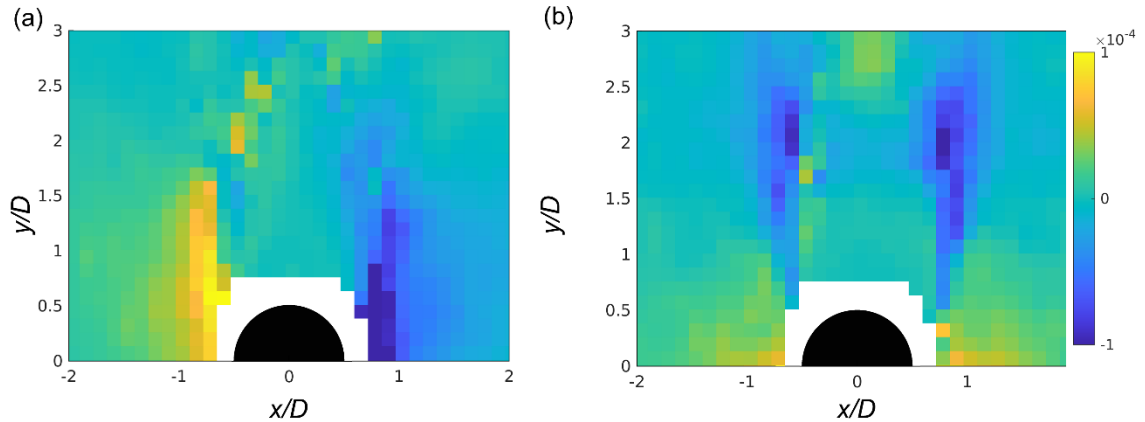


Figure 3-8: Time-averaged net force acting on bubbles in (a) horizontal direction and (b) vertical direction.

3.3.2 Analysis of Bubble Trapping

To analyze the bubble dynamics using Eq. 3-8, measurements of both liquid and bubble velocities were measured following the methods described in Chapter 2.3 at $Re = 2,956$ and $j_g = 0.06$ m/s. These conditions were chosen to allow optical resolution of flow tracers in between bubbles in the flow.

Heat maps of the time-averaged net horizontal and vertical forces acting on the large bubbles as they move around the cylinder are shown in Figure 3-8. The figure shows a region of negative horizontal forces to the right of the cylinder (Figure 3-8(a)), the strongest of which are located where $0.5 < x/D < 1$ and $0 < y/D < 1.5$. Similarly, there is a region of positive horizontal forces to the left of the cylinder (Figure 3-8(a)), concentrated especially where $-1 < x/D < 0.5$ and $0 < y/D < 1.5$. The bubbles in these regions experience a strong horizontal force attracting them towards

the centerline. This color map of the net horizontal forces suggests that there were strong net horizontal forces acting on bubbles around $x/D = \pm 0.8-1$, but that this trapping force quickly diminished downstream, being much lower at $y/D = 1.5$ and 2 . In contrast, the strongest vertical forces are located further downstream where $1.5 < y/D < 2.5$ (Figure 3-8(b)). The negative values indicate a net downward force in this region, which act against bubbles moving upwards to leave the cylinder wake. In addition, a large force in the downward direction occurs at $x/D \approx \pm 0.9$ and $1.8 < y/D < 2.5$. This color map shows that bubble-trapping occurs in two steps. Firstly, the net horizontal force near the cylinder attracts the bubbles towards the centerline as they pass around the cylinder. Secondly, the vertical force in the near wake ($1.5 < y/D < 2.5$) decelerates bubbles as they pass through the wake.

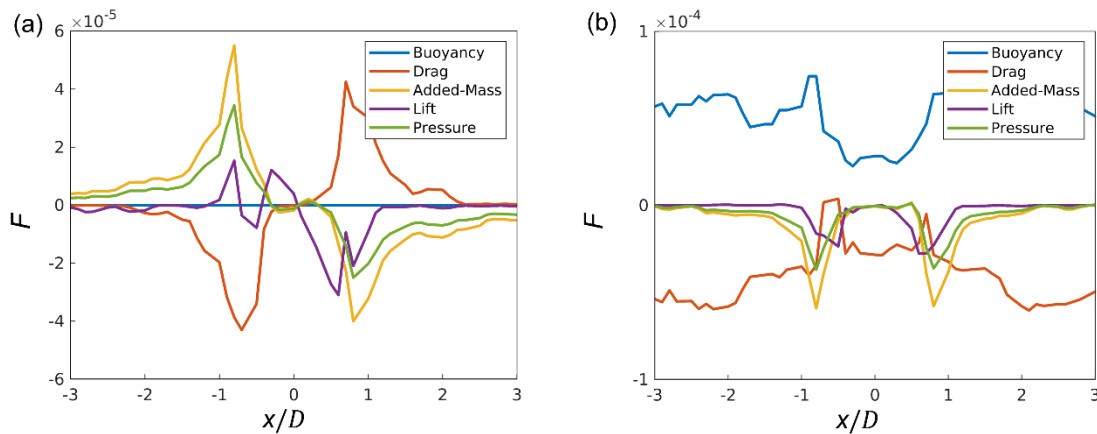


Figure 3-9: Time-averaged force balance on air bubbles behind a cylinder at $y/D = 1.5$ (a) in x direction and (b) in y direction

Figure 3-9 shows the details of the force balance components in the x and y direction at $y/D = 1.5$. The time-averaged results show that added-mass, pressure gradient, and lift forces were strong enough to create a net inward force at $x/D \approx \pm 0.8$, contributing to bubble trapping. In the horizontal direction, the drag force opposed bubble trapping. In the vertical direction, bubble

buoyancy and drag largely canceled since the flow was fully developed; however, the added-mass, pressure gradient, and lift terms show peaks in the downward direction at $x/D \approx 0.7-0.8$. Thus, added-mass, pressure, and lift forces were the primary components that contributed to bubble trapping by both moving bubbles inwards and slowing their ascent within the cylinder wake. A noteworthy feature shown in Figure 3-9(b) is that the buoyancy forces for $0.8 < x/D < 0.8$ appear lower than in the freestream. This is a result of smaller bubbles being preferentially captured in the wake, where the resulting calculated buoyancy force was smaller due to the smaller bubble sizes. In the freestream, the average bubble equivalent diameter was about 3.5 mm. However, the bubbles inside the bubble-trapping wake region at $y/D = 1.0$ were approximately 1.5 mm.

3.3.3 Bubble Trapping Parameter

The results presented in the previous section revealed that added-mass, pressure gradient, and lift forces contributed to bubble trapping while drag forces acted against the phenomena. Based on the force balance equations, non-dimensional parameters, $(F_A + F_P) / F_D$ and F_L / F_D , are proposed to characterize the bubble trapping behavior. The bubble forces can be simplified by applying order of magnitude analysis and eliminating the common fluid density and bubble volume terms from Eq. (6) through (9). The force components then simplify to $F_A \approx C_A |v_{l,\infty}|^2 / D$, $F_P \approx |v_{l,\infty}|^2 / D$, $F_L \approx C_L |(v_{l,\infty} - v_{g,\infty})v_{l,\infty}| / d$, and $F_D \approx C_D |v_{l,\infty} - v_{g,\infty}|^2 / d$. In this approximation, the material derivatives $(D\vec{u}_i / Dt = \partial\vec{u}_i / \partial t + \vec{u}_i \cdot \nabla\vec{u}_i)$ in the \vec{F}_A and \vec{F}_P terms were simplified as $v_{l,\infty}^2 / D$ since the freestream liquid velocity and the cylinder diameter will determine the maximum velocity difference experienced in the cylinder wake. Similarly, the bubble diameter was used to approximate the lift forces and the drag forces acting on the bubbles. These simplified

relationships were then used to compare the forces contributing to trapping (inertial and lift) to the opposing drag. These ratios are given as

$$\frac{\text{Inertia}}{\text{Drag}} = \frac{\text{Added-Mass+Pressure}}{\text{Drag}} \approx \frac{(C_A + 1)}{C_D} \left| \frac{v_{l,\infty}}{v_{l,\infty} - v_{g,\infty}} \right|^2 \frac{d}{D}, \quad (3-10)$$

and,

$$\frac{\text{Lift}}{\text{Drag}} \approx \frac{C_L}{C_D} \left| \frac{v_{l,\infty}}{v_{l,\infty} - v_{g,\infty}} \right|. \quad (3-11)$$

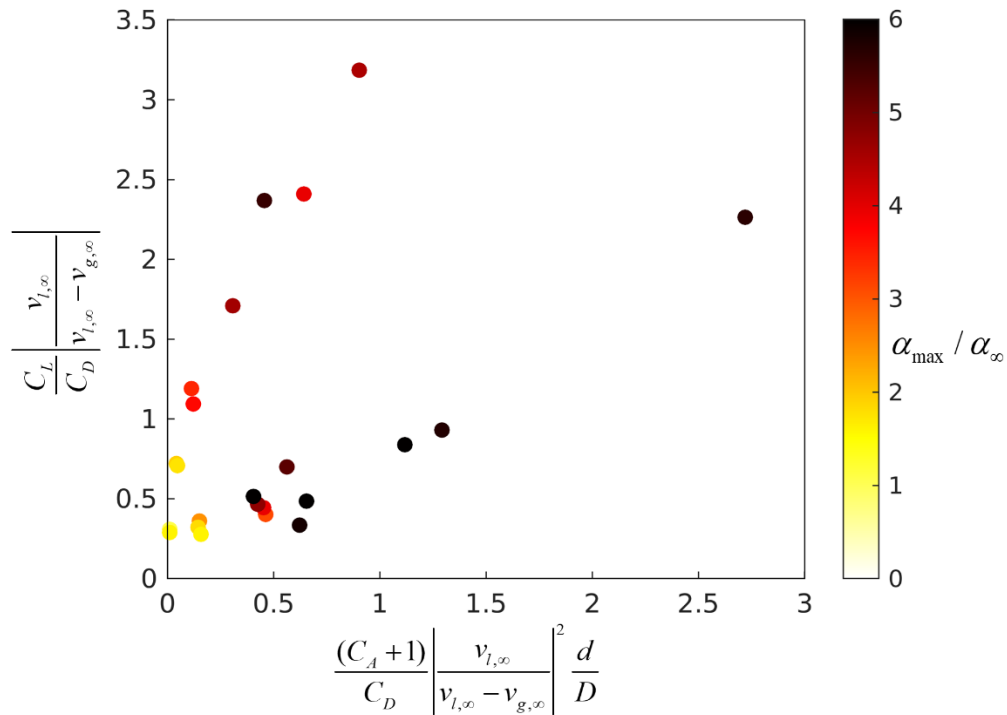


Figure 3-10: Comparison of lift-to-drag ratio to inertia-to-drag ratio and the maximum void fraction ratio in the wake ($0 < y/D < 5$).

This scale analysis approximates the detailed force balance of the previous section with freestream flow parameters. Since only freestream parameters are needed, the resulting comparison of relevant forces can be applied to all of the experimental cases shown in Table 2-1, even those without liquid-phase velocimetry. By analyzing the freestream values, the bubble-

trapping phenomena can be explained by considering the relationship between the inertia-to-drag ratio and the lift-to-drag ratio of a given flow condition.

Figure 3-10 compares the lift-to-drag ratio and inertia-to-drag ratio, where each data point is colored using the maximum detected void fraction ratio for that flow condition within $0 < y/D < 5$. Assuming a threshold of $\alpha/\alpha_\infty = 2.0$ as being indicative of bubble trapping, the figure shows that bubble trapping occurred when the inertia-to-drag ratio was greater than 0.35, regardless of the lift-to-drag ratio. On the other hand, bubble trapping also always occurred when the lift-to-drag ratio was greater than one. Below these two threshold values, bubble trapping only occurred if either of the inertial force or the lift force was sufficient to cause the bubble trapping. Previously, bubble trapping was considered primarily an effect dominated by inertial forces. Sene et al. (1994) characterized the bubble trapping in their horizontal shear layer using the inertia-to-buoyancy ratio and a trapping parameter. Milenković et al. (2007) advanced these parameters by including the effect of bubble diameters and vortex diameters to explain bubble trapping. However, both studies did not capture the importance of the lift forces, especially for bubbles with a small diameter. The current experimental results suggest that both inertial and lift effects, which vary not only with velocities but also cylinder and bubble sizes, must be considered to explain the bubble-trapping phenomena in the near wake of a cylinder.

3.4 Conclusion

The experimental investigation of an upward liquid-gas flow around a cylinder characterized the occurrence of bubble trapping in the near wake behind the cylinder in terms of the inertia-to-drag ratio and the lift-to-drag ratio. Bubble concentration behind the cylinder at different flow parameters was discussed using a calibrated void fraction ratio, which allowed the presentation of local void fraction distributions. In addition, PIV and PTV measurements were used to determine the mean bubble velocities in the near wake to show how bubble motion is altered when bubble trapping occurs. The result concludes that the bubbles were primarily concentrated behind a cylinder at downstream locations of $1.0 < y/D < 3.0$ when certain flow conditions are met. In addition, PSIV was used to analyze the time-averaged liquid trajectories while the air bubbles existed in the system. This phase-resolved velocimetry allowed for a force balance analysis by analyzing the bubble diameter and velocities experienced by the liquid and gas flows.

By introducing two drastically different bubble size distributions, the experiment was able to vary the relative lift and inertial forces acting on the dispersed bubbles in the flow. As a result, a force magnitude analysis showed that bubble trapping occurred when the inertial or lift forces acting on the bubbles were significant compared to their drag force. The inertia-to-drag ratio and lift-to-drag ratio were defined, which relate freestream velocities of the liquid and gas phases, mean bubble diameter, and cylinder diameter. These parameters can be used to predict the conditions that will lead to bubble trapping around a bluff body in a crossflow.

4. Transitional Behavior of the Bubble-Trapping Region and Effects of Bubbles on the Wakes

In the previous chapter, the bubble-trapping parameter was developed to explain the occurrence of the bubble-trapping region in a liquid-gas flow around a cylinder based on the time-averaged liquid and gas velocities. The force balance analysis, which was built using the time-averaged two-phase velocities and bubble diameters, concluded that the relative strength of inertial and lift forces to drag force is the key explanation of the bubble trapping phenomenon. In addition, the transitional behavior of bubble trapping was reported at the Reynolds number of 1,182 in Chapter 2 with a mean bubble diameter of 3.5 mm. In the previous chapter, the bubble trapping region occurred at Reynolds numbers above 2,000 due to the sufficient inertial forces acting on the air bubble. However, the force balance analysis results in Chapter 3 concluded that the lift force could induce the bubble-trapping region despite the low inertial forces at a low Reynolds number. In this chapter, the bubble-trapping phenomenon is investigated at a laminar Reynolds number of 493, to transitional Reynolds numbers of 1,478 and 2,463, to clarify the influence of inertial and lift forces on the bubble-trapping phenomenon. For the verification of the time-averaged evaluation, the time-dependent liquid velocities around the cylinder at $Re = 2,956$ were analyzed in this chapter with and without injecting air bubbles. Due to the time-averaging process, the oscillatory behavior of velocities around the cylinder could potentially affect the results. The purpose of this analysis is to show the influence of bubble trapping on the velocity fluctuations and alternating vortex shedding in the wake.

Table 4-1: Experimental flow conditions.

	Re	j_g [m/s]	d [mm]
Time-Averaged (Steady PSIV)	493	0.18	3.2 ± 1.5
	1,478	0.18	3.2 ± 1.2
	2,463	0.18	2.9 ± 1.0
Time-Dependent (Transient PSIV)	2,956	-	-
	2,956	0.06	2.6 ± 1.0

4.1 Method

The experimental flow conditions for this chapter are shown in Table 4-1. The liquid Reynolds number varied from 493 to 2,463 to cover the range of transitional two-phase wakes around the cylinder, which exhibited the bubble-trapping region. The air injection occurred at $j_g = 0.18$ m/s; the mean bubble diameter varied from 2.9 mm to 3.2mm. In addition, a single-phase flow experiment was conducted without injecting air bubbles at $Re = 2,956$ for the verification of the time-averaged analysis. For the comparison, the images of the liquid-gas flow at $Re = 2,956$ and $j_g = 0.06$ m/s, discussed in Chapter 3, were also analyzed for the transient PSIV. As used in Chapter 3, the neutrally-buoyant flow tracers were injected throughout the experimental flow conditions; the high-speed images were collected at 2,000 fps.

The transitional flow conditions for the bubble trapping region were reported in Chapter 3 where the bubble trapping may occur at a Reynolds number smaller than 2,000. However, the previous chapter could not explain the cause of the transitional behavior. The previous result hinted that the lift forces on air bubbles caused the bubble trapping even if the inertial forces were small. In this chapter, the forces acting on air bubbles at a transitional Reynolds number from 493 to 2,463 is reported. For this experiment, the upward liquid-gas channel with a high-speed camera was used, as discussed in Chapter 2. For the phase-resolved force balance analysis, the high-speed camera measured the movement of the air bubbles and the flow tracers, as discussed in Chapter 3.1. In addition, the image acquisition and processing procedures for this time-averaged analysis on the two-phase images at $Re = 493, 1,478, \text{ and } 2,463$ are identical to the one from Chapter 3.1.

For the time-dependent analysis at $Re = 2,956$, bigger investigation windows were used. During the transient PSIV analysis, the first pass used a grid of 128 pixels by 128 pixels with 50% window overlap. Following the first pass analysis, the transient PSIV analysis used a grid of

64 pixels by 64 pixels with 50 % window overlap as the second pass. The single-phase case data collected at $Re = 2,956$ had a sufficient number of flow tracers, even for the small investigation windows used in the time-averaged PSIV analysis. However, the two-phase high-speed images at $Re = 2,956$, which were collected for Chapter 3, at $Re = 2,956$, resulted in poor signal-to-noise ratios in some investigation windows due to the existence of bubbles for the two-phase images. The smaller window size which was used for the ensemble correlation of the time-averaged analysis was too small for the transient PSIV analysis. The transient analysis results are available in Chapter 4.3.2.

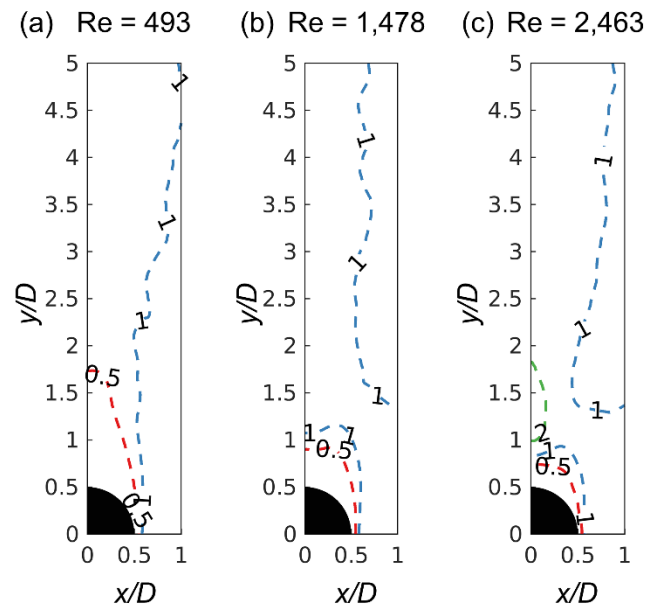


Figure 4-1: Contour plots of the void fraction ratio behind the cylinder at $j_g = 0.36$ m/s (a) $Re = 493$ (b) $Re = 1,478$, and (c) $Re = 2,463$ (d) $Re = 2,069$.

4.2 Result

4.2.1 Void Fraction Ratio

The void fraction ratio (α/α_∞) resulting from the injection of air bubbles at Reynolds numbers of $Re = 493, 1,478,$ and $2,463$ is shown in Figure 4-1. Similar to the previous results in Chapter 3.2, the liquid-phase region ($\alpha/\alpha_\infty < 0.5$) occurred throughout the range of Reynolds numbers. The length of the liquid-phase region decreased, from $L_f = 1.25$ to 0.25 , as the Reynolds number increased from 493 to $2,463$. In addition, the bubble-trapping region ($\alpha/\alpha_\infty > 2.0$) was observed at $Re = 2,463$, which confirms the previous experimental investigation in Chapter 3 that the bubble-trapping region generally occurs for $Re > 2,000$ (Figure 4-1(c)) for this cylinder and bubble size. The bubble-trapping region was not observed at $Re = 1,478$; however, the length of the liquid-phase region appears to be significantly restricted (Figure 4-1(b)), which is characteristic of the onset of bubble-trapping. The shape of the liquid-phase region at $Re = 1,478$ is similar to the one at $Re = 2,463$ and similar to those presented in Chapter 3 in Figure 3-4(d) at $Re = 2,069$ and in Figure 3-4(e) at $Re = 2,956$. The liquid-phase region at $Re = 493$ is formed around the cylinder and slowly tapers towards the centerline before terminating at $y/D = 1.8$ in Figure 4-1(a). The liquid-phase region shown in this figure has the same feature shown in the previous analysis in Figure 3-4(a-c) when the bubble-trapping region did not occur. Even though the bubble-trapping region did not occur at $Re = 1,478$, it is possible that it was in a transition to the occurrence of the bubble-trapping region.

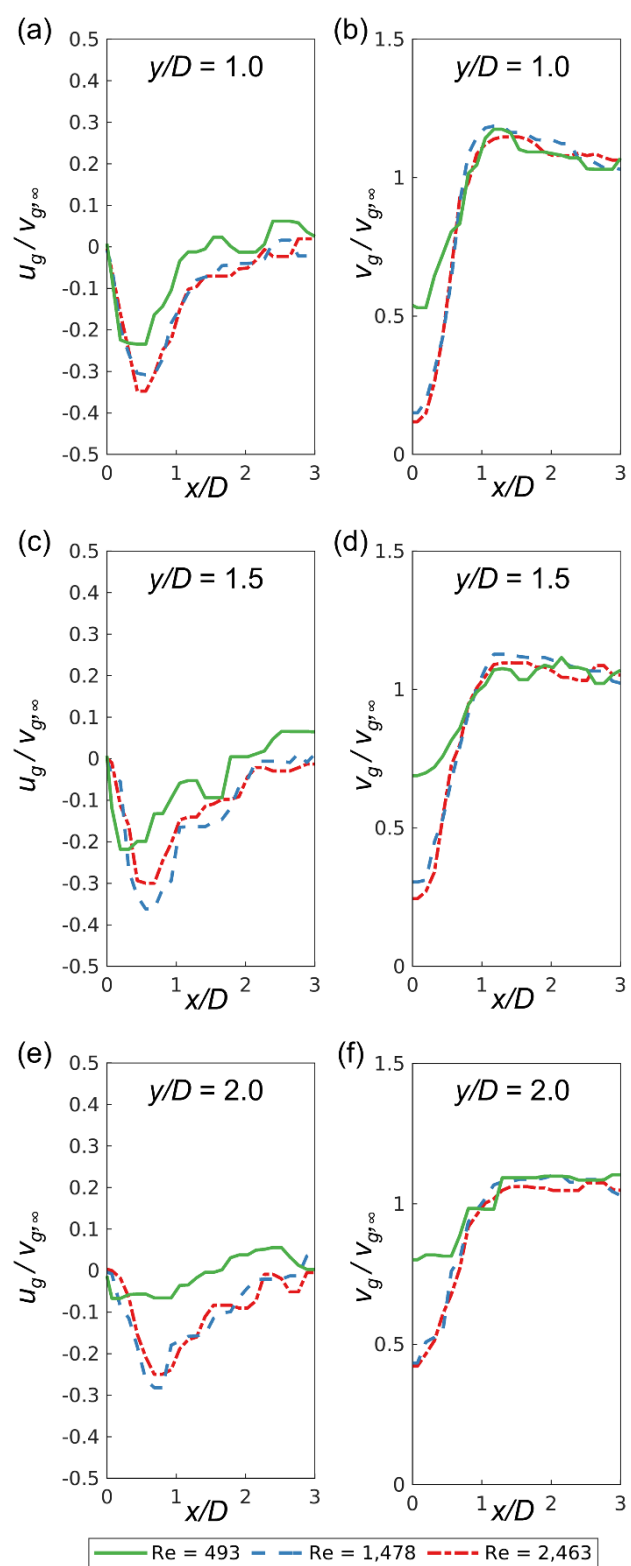


Figure 4-2: Horizontal (left) and vertical (right) velocity ratios for the air bubbles at $y/D = 1.0$ (a-b), $y/D = 1.5$ (c-d), and $y/D = 2.0$ (e-f).

4.2.2 Air Velocities in the Wakes

Horizontal velocity ratio ($u_g/v_{g,\infty}$) and vertical velocity ratio ($v_g/v_{g,\infty}$) for the air bubbles at $y/D = 1.0, 1.5,$ and 2.0 and $0 < x/D < 3$ are available in Figure 4-2. The local horizontal and vertical velocities were divided by the freestream air velocities to calculate the relative reduction of air velocities at the three downstream locations.

As the figure focuses on the right side of the cylinder ($x/D > 0$), a negative horizontal velocity ratio indicates the air bubble movement towards the centerline in Figure 4-2(a,c,e). All of the cases resulted in negative horizontal velocity ratios of $0 < x/D < 1$ at the downstream locations. Regardless of the Reynolds number, the figure suggests that the bubbles moved toward the centerline. However, the relative magnitude of the velocity was much smaller at $Re = 493$. When the Reynolds numbers were greater at 1,478 and 2,463, the patterns of the horizontal velocity ratio were comparable to each other. This suggests that more active horizontal movement of air bubbles occurred at $Re = 1,478$ and 2,463, where their inward bubble velocities peaked at $x/D \approx \pm 0.8$.

The vertical velocities remained in the positive direction, as shown in Figure 4-2(b,d,f) throughout the downstream locations plotted. At all three Reynolds numbers, a significant reduction of vertical bubble velocities occurred. At $Re = 493$, the vertical velocity was reduced by up to 50% of the freestream velocity. However, much more velocity reduction occurred at $Re = 1,478$ and 2,463, up to 90% of the freestream velocity. The most reduction of the vertical velocities occurred at $y/D = 1.0$. As moving further downstream, the reduction of the vertical velocity ratio decreased. However, a significant reduction of vertical velocity still occurred at $Re = 1,478$ and 2,463 throughout the downstream locations.

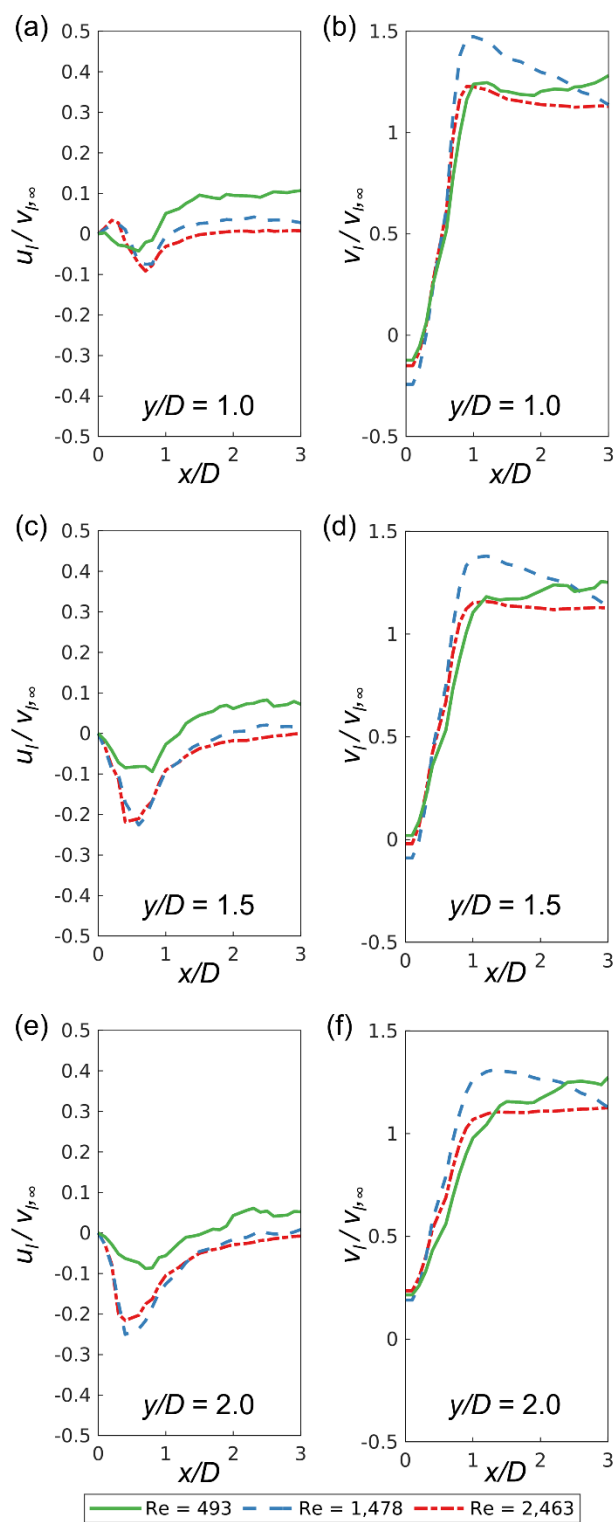


Figure 4-3: Horizontal (left) and vertical (right) velocity ratios for water at $y/D = 1.0$ (a-b), $y/D = 1.5$ (c-d), and $y/D = 2.0$ (e-f).

4.2.3 Liquid Velocities in the Wakes

Horizontal velocity ratio ($u/v_{l,\infty}$) and vertical velocity ratio ($v/v_{l,\infty}$) for the liquid phase at $y/D = 1.0, 1.5,$ and 2.0 and $0 < x/D < 3$ are available in Figure 4-3. Similar to the air velocity ratios, as shown in Figure 4-2, these values in Figure 4-3 represent the relative horizontal and vertical velocities compared to its freestream liquid velocities.

The horizontal velocity ratios for the liquid phase were similar to their freestream values at $y/D = 1.0$, as shown in Figure 4-3(a). The liquid flow moved towards the centerline at 5-10% of its freestream velocity around at $x/D = 0.6-0.7$ when it was close to the cylinder ($y/D = 1.0$). As moving further away downstream, the magnitude of the horizontal velocity ratios increased, as shown in Figure 4-3(a,c,e). At the downstream location of $y/D = 2.0$, the inward horizontal velocity of up to 25% of its freestream velocity was induced. At a low Reynolds number of 493, the horizontal velocity reduction was small. However, significant horizontal velocity was captured at higher Reynolds numbers of 1,478 and 2,463.

The vertical velocity ratios for the liquid phase are shown in Figure 4-3(b,d,f). At $y/D = 1.0$, the ratios of the liquid velocities reveal that there was a downward movement of the liquid phase (Figure 4-3(b)). At $y/D = 1.5$, the ratios of the liquid velocities reached zero, where the liquid phase shall be suspended at the given location in a time-averaged motion. Further downstream location at $y/D = 2.0$, the liquid velocity ratios remained positive but with a greater reduction to their freestream values. It is also noticeable that almost the same amount of vertical velocity reduction occurred throughout the downstream locations with various Reynolds numbers.

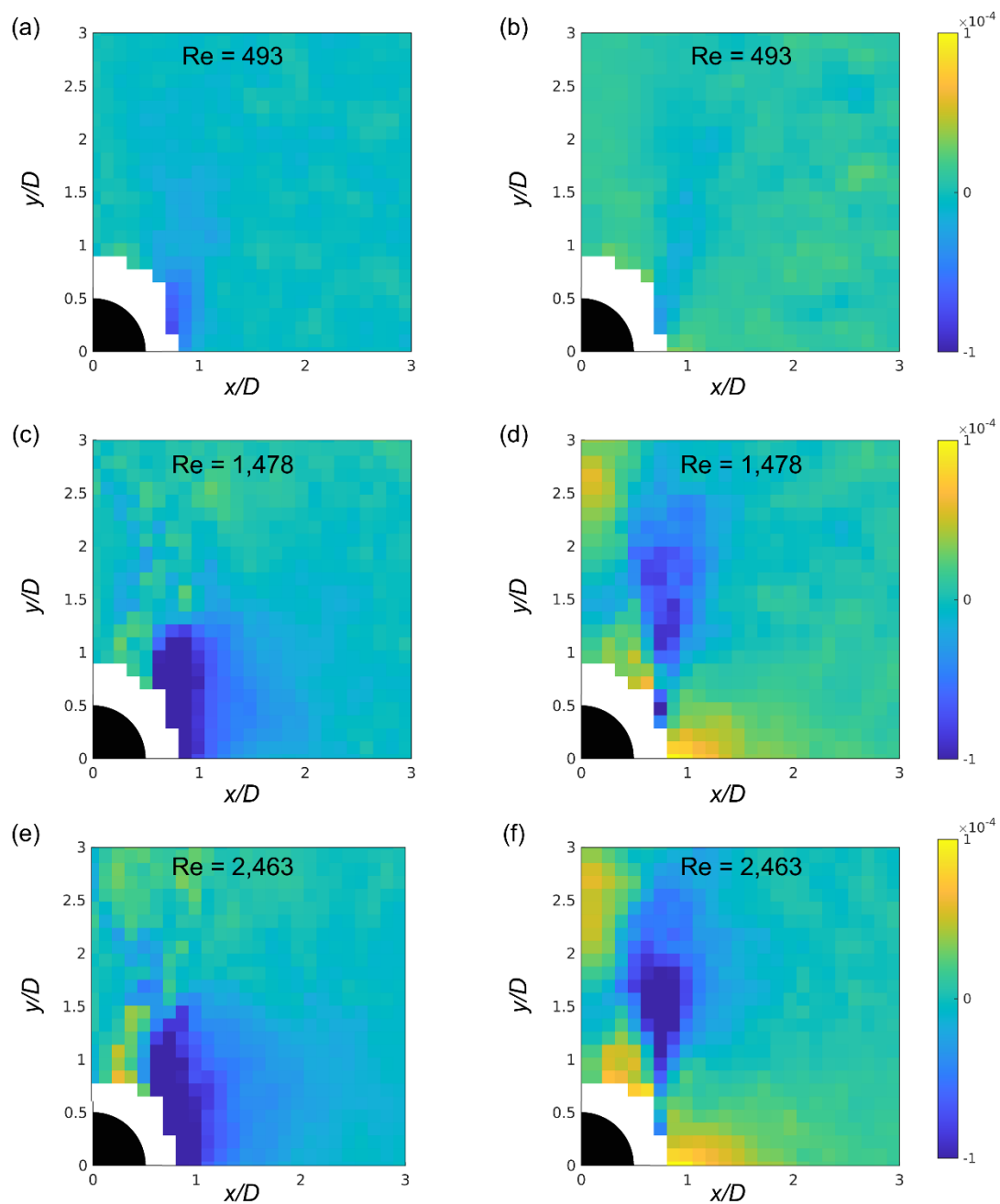


Figure 4-4: Time-averaged net force acting on bubbles in (a) the horizontal direction at $Re = 493$, (b) the vertical direction at $Re = 493$, (c) the horizontal direction at $Re = 1,478$, (d) the vertical direction at $Re = 1,478$, (e) the horizontal direction at $Re = 2,463$, and (f) the vertical direction at $Re = 2,463$.

4.3 Discussion

4.3.1 Bubble-Trapping Forces

Based on the phase-resolved velocity measurements of liquid and gas phases, the forces acting on the bubbles were calculated using Eq. 3-8. Time-averaged net horizontal and vertical forces acting on the bubbles are represented as color maps in Figure 4-4. At the Reynolds number of 493, the color maps show that net forces were not enough to attract bubbles towards the centerline of $x/D = 0$ in Figure 4-4(a,b). There was a small amount of net horizontal force near the cylinder ($x/D = 0.7-0.8$ and $y/D = 0.2-0.6$); however, the intensity of the color map in Figure 4-4(a) is not as strong as other color maps such as Figure 4-4(c,e).

The strong horizontal net force towards the cylinder was observed for $Re = 1,478$ and $Re = 2,463$ in Figure 4-4(c) and Figure 4-4(e). Even though some data points are not available due to a lack of observed bubble movement around the cylinder, the two figures suggest that there was a strong inward net force in the horizontal direction throughout the region of $0.6 < x/D < 1.0$ and $0 < y/D < 1.25$. Similarly, the strong vertical net force in the downward direction was observed for $Re = 1,478$ and $Re = 2,463$ in Figure 4-4(d) and Figure 4-4(f). Even though the intensity of the vertical net force at $Re = 1,478$ is slightly weaker than the force at $Re = 2,463$, the region of strong vertical net force in the downward direction locates at $0.5 < x/D < 1.2$ and $1.0 < y/D < 2.5$ for both cases in Figure 4-4(d) and Figure 4-4(f). This analysis reconfirms that the bubble-trapping force is acting in two locations based on the vertical and horizontal components, as stated in Chapter 3.3. In addition, this experimental result reveals that the bubble-trapping did not occur at $Re = 493$ due to a lack of bubble-trapping forces acting on the bubbles.

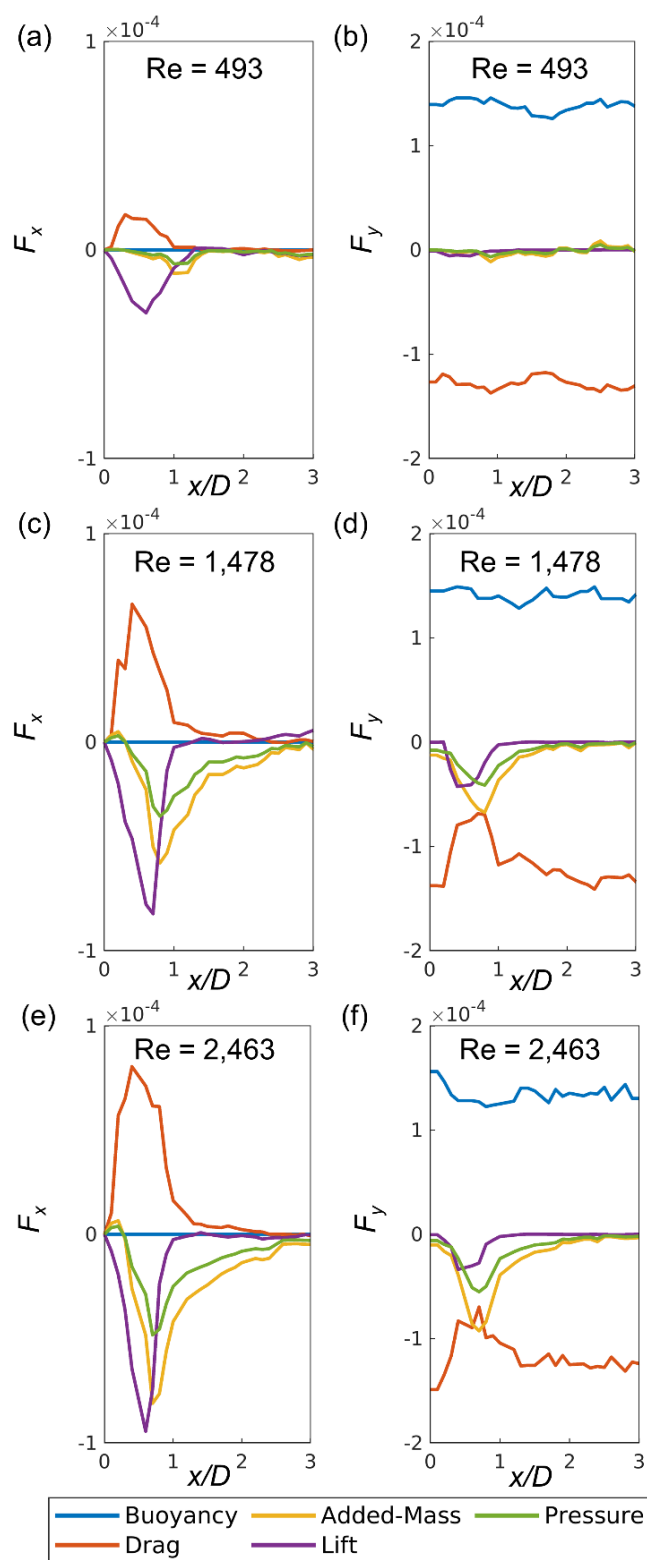


Figure 4-5: Time-averaged force balance on air bubbles behind a cylinder: (a,c,e) in the x direction at $y/D = 1.0$ and (b,d,f) in the y direction at $y/D = 1.5$.

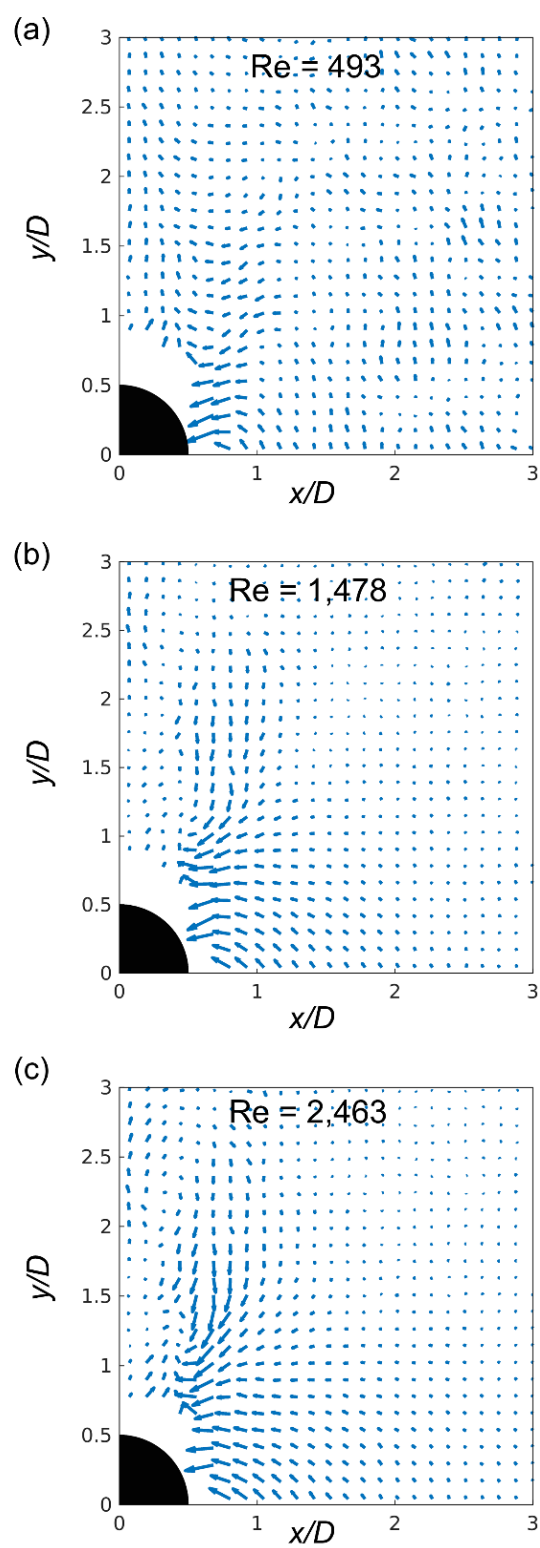


Figure 4-6: Vector plots of the time-averaged net force acting on bubbles at (a) $Re = 493$, (b) $Re = 1,478$, and (c) $Re = 2,463$. (Note, the magnitude of the vectors is scaled independently)

Based on the time-averaged net force calculation in Figure 4-4, the net horizontal force's peak locations were at $y/D \approx 1.0$ and the net vertical force at $y/D \approx 1.5$. For understanding the components of the forces acting on the bubble at the peak locations, the details of time-average horizontal forces at $y/D = 1.0$ and vertical forces at $y/D = 1.5$ at the Reynolds number of 493, 1,478, and 2,463 are shown in Figure 4.5.

At $Re = 493$, there was a small amount of net horizontal force toward the centerline near the cylinder (Figure 4-4(a)). This is because there was a small amount of lift force acting on the bubble in the wakes, as shown in Figure 4-5(a). Even though the drag force acted against the lift force, the lift force could induce a marginal net horizontal force at $x/D = 0.7$. However, there were no other acting forces in this case. At a downstream location of $y/D = 1.5$, the buoyancy force and the drag force were balanced out in the vertical direction, which resulted in almost net zero force (Figure 4-5(d)). Despite the act of the lift force in the horizontal direction, the magnitude was not sufficient to cause the bubble-trapping region at $Re = 493$.

When the Reynolds number was increased to 1,478 or 2,463, there was noticeable strength of lift forces and inertial (added-mass and pressure-gradient) forces acting in the negative direction in horizontal and vertical directions (Figure 4-5(b,c,e,f)). Even though the horizontal and vertical forces act on the different regions, as shown in Figure 4-4, their coordination forms the bubble-trapping force towards the centerline. In the horizontal direction, the details of the forces revealed that the lift force is the strongest bubble-trapping force at $x/D = 0.7$ and $y/D = 1.0$. Followed by the lift force, the added-mass force, and the pressure-gradient force act as the bubble-trapping force in the horizontal direction. Their peak location is slightly away from the centerline of $x/D = 0.8$ compared to the lift force. Closer to the centerline ($0.5 < x/D < 0.7$), the lift force dominates the bubble-trapping in the horizontal direction. Slightly away from the centerline ($0.8 < x/D < 1.0$), the added-mass and pressure-gradient forces are the dominants for the bubble-trapping force in the horizontal direction. In the vertical direction, the details of the forces also revealed that lift,

added-mass, and pressure-gradient forces contributed to trapping the bubbles. However, the figure unveiled that lift force took a much smaller role in trapping the bubble in the downward direction. Instead, the added-mass and pressure-gradient forces dominated the bubble-trapping in the downward direction. Comparing Figure 4-5(e) and Figure 4-5(f), the inertial forces (added-mass and pressure-gradient forces) increased as the Reynolds number increased from 1,478 to 2,463. As the bulk fluid had greater inertia force, greater inertial forces contributed to the bubble trapping in the vertical direction. This detailed analysis confirms that both lift and inertial forces are important for the bubble-trapping phenomenon around a cylinder. The lift force takes an important role in the horizontal direction near the cylinder ($0.5 < x/D < 0.7$). At the same time, the inertial forces are important in the horizontal and vertical directions, slightly away from the cylinder ($0.8 < x/D < 1.0$).

Vector plots of the time-average net force are shown in Figure 4-6. The magnitude of the vectors was adjusted based on the maximum net force of individual cases. Consequently, this figure should not be used to compare the magnitude of forces across different Reynolds numbers. Instead, this figure provides valuable information about the direction of the net forces on bubbles in each case. In the region of $0.5 < x/D < 1.0$ and $0 < y/D < 1.0$, the vector plot suggests that there was horizontal net force towards the centerline throughout the range of Reynolds number. On the other hand, in the region of $0.5 < x/D < 1.0$ and $1.0 < y/D < 2.5$, the vector plot reveals a downward net force appeared as the Reynolds number was greater than 1,478. From here, it is believed that the bubble trapping occurs in two steps: (i) net force towards the centerline in the region of $0.5 < x/D < 1.0$ and $0 < y/D < 1.0$ and (ii) downward net force in the region of $0.5 < x/D < 1.0$ and $1.0 < y/D < 2.5$.

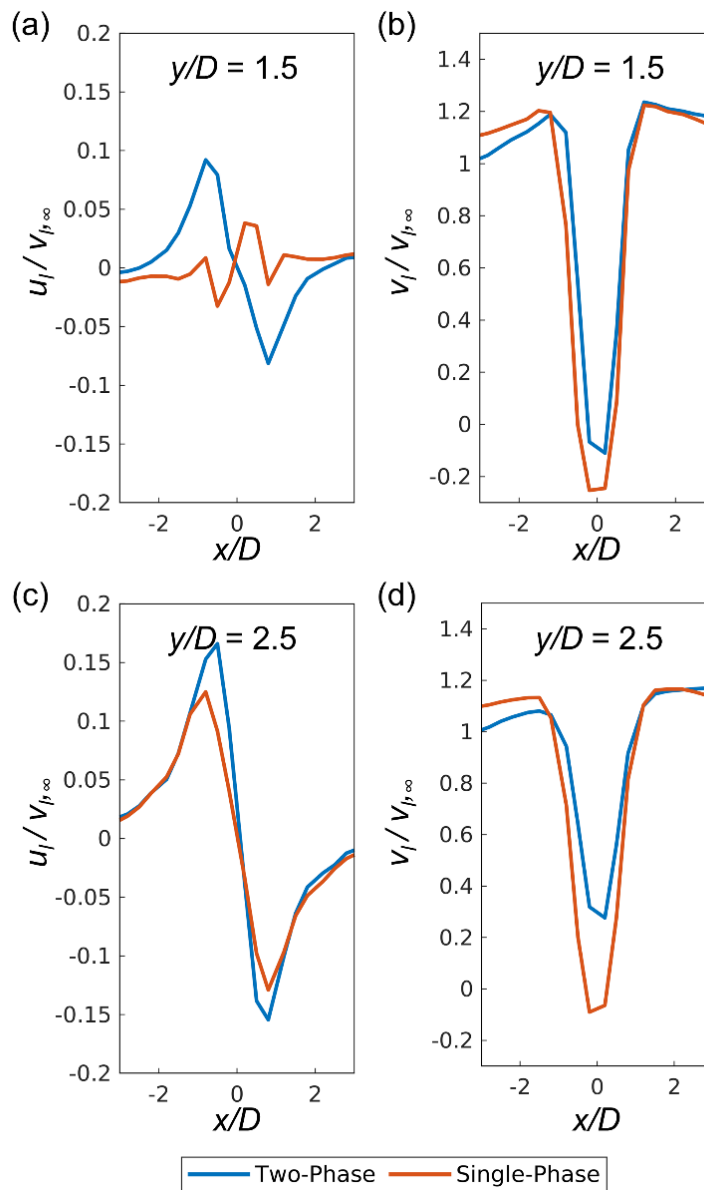


Figure 4-7: Horizontal (left) and vertical (right) mean liquid velocity ratios at $y/D = 1.5$ (a-b) and $y/D = 2.5$ (c-d) for the two-phase and single-phase crossflows at $Re = 2,956$.

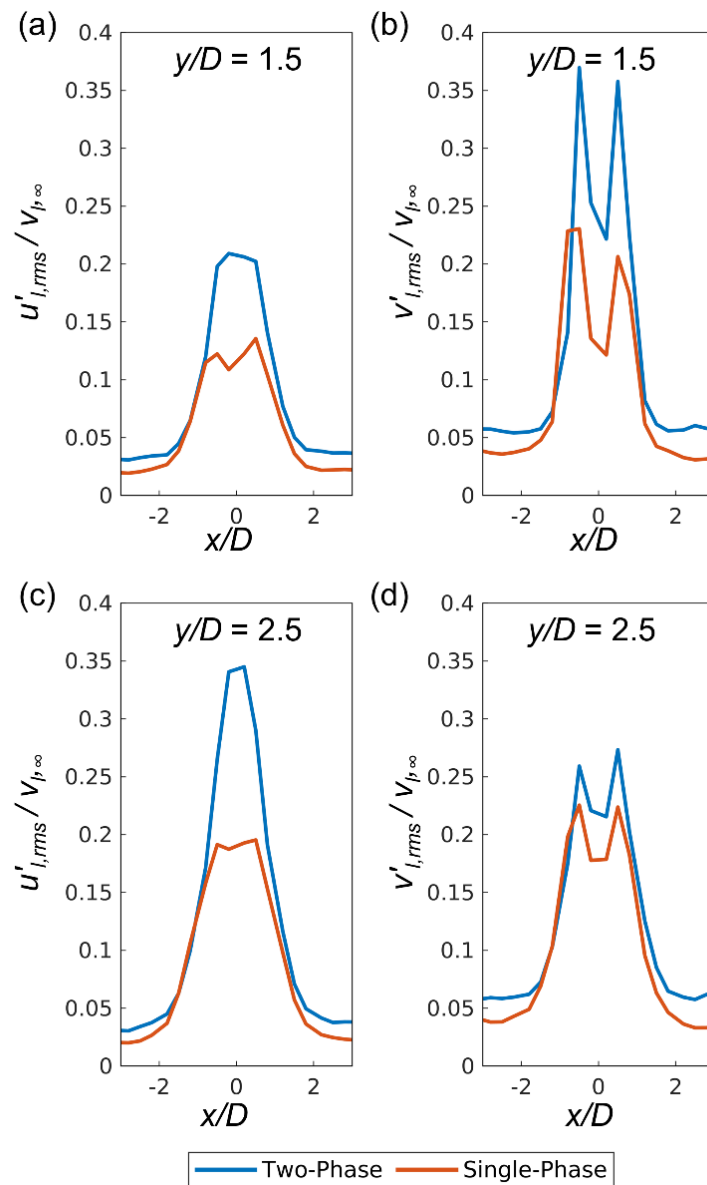


Figure 4-8: Horizontal (left) and vertical (right) fluctuating liquid velocity ratios at $y/D = 1.5$ (a-b) and $y/D = 2.5$ (c-d) for the two-phase and single-phase crossflows at $Re = 2,956$.

4.3.2 Effects of Bubbles on the Wakes

Using Reynolds decomposition [86], the liquid velocities were decomposed into mean and fluctuations as $u = u_l + u'_{l,rms}$ and $v = v_l + v'_{l,rms}$, where u represents horizontal liquid velocity and v represents the vertical liquid velocity. Figure 4-7 shows the ratio between mean horizontal and vertical liquid velocity, u_l and v_l , to the freestream liquid velocity, $v_{l,\infty}$, at the downstream locations of $y/D = 1.5$ and $y/D = 2.5$ for the two-phase crossflow and the single-phase crossflow. At the downstream location of $y/D = 1.5$, the single-phase crossflow did not observe a significant variation of mean velocity in the horizontal direction (Figure 4-7(a)). However, the same plot shows that the liquid flow in the two-phase flow observed positive mean velocity ratios from $x/D = -1.5$ to $x/D = 0$ and negative mean velocity ratios from $x/D = 0$ to $x/D = 1.5$. Comparing the vertical liquid velocity ratios at $y/D = 1.5$, the liquid flow had similar mean behavior in the vertical direction regardless of the injection of the air bubble (Figure 4-7(b)). Further downstream at $y/D = 2.5$, it became more apparent that the horizontal liquid movement became more substantial when the air bubbles were injected (Figure 4-7(c)). However, the vertical liquid velocity ratios suggest that the liquid flow faced less velocity reduction in the vertical direction when the bubbles were injected (Figure 4-7(d)). For both cases of the two-phase and single-phase crossflows, the liquid flow in the wakes around the cylinder moved towards the centerline, $x/D = 0$. By injecting air bubbles, the horizontal liquid movement was enhanced in the wakes. On the other hand, the air bubbles induced faster vertical liquid velocities in the wakes. However, the vertical liquid velocity in the wakes was still slower than the freestream velocity.

The liquid velocity fluctuations from the Reynolds decomposition are represented in Figure 4-8 as the ratio between fluctuating velocities, $u'_{l,rms}$ and $v'_{l,rms}$, and freestream liquid velocity, $v_{l,\infty}$. At the downstream location of $y/D = 1.5$, the vertical fluctuations were greater than

the horizontal fluctuations for both two-phase and single-phase crossflows (Figure 4-8(a-b)). In addition, the velocity fluctuations in both directions were more significant when the two-phase mixture was injected. At the downstream location of $y/D = 2.5$, the velocity fluctuations of the single-phase flow were similar in horizontal and vertical directions from (Figure 4-8(c-d)). By injecting air bubbles, a greater fluctuating liquid velocity in the horizontal direction occurred at $y/D = 2.5$; a greater fluctuating liquid velocity in the vertical direction occurred at $y/D = 1.5$. In addition, the figure suggests that the fluctuating velocity is symmetric along the centerline ($x/D = 0$). Even though the wakes could be formed with a periodic oscillation at $Re = 2,956$, the current analysis contains high-speed images with sufficient time duration to capture oscillatory behavior and conclude time-averaged results, as discussed in Chapter 3.

In addition, the comparison of the liquid velocities of the two-phase and single-phase crossflows revealed that the bubbles had possibly induced additional movement and disturbance in the wakes around the cylinder. The maximum horizontal velocity ratio increased with bubble injection (Figure 4-7(a,c)). In addition, the horizontal velocity fluctuation increased compared to its freestream velocity in both horizontal and vertical directions as the bubbles were injected, indicating greater mixing and momentum transfer occurred within the wakes (Figure 4-8). However, the vertical velocity ratio was decreased when the bubble was injected (Figure 4-7(b,d)). A potential answer to this behavior is the buoyancy-induced movement of air bubbles. The air bubbles have buoyancy force, always acting on the vertical direction. As the air bubbles move upward due to the buoyancy force, their movement may have diminished the downward liquid movement in the wakes. Even though the less liquid velocity reduction in the vertical direction inside the wakes occurred from injecting air bubbles, the high-speed images and the time-averaged result from Chapter 2 observed that the bubble-trapping region exists at $Re = 2,946$. Based on a previous high-speed visualization report at $Re = 2,946$, air bubbles with a mean

diameter of 3-4 mm were held up in the bubble-trapping region ($1.0 < y/D < 3.0$) for about 0.12 s [87].

4.4 Conclusion

This experimental investigation of liquid-gas flow around a cylinder at a transitional Reynolds number confirmed that the lift force and inertial forces take important roles in the bubble-trapping region. Based on the void fraction ratio analysis, the bubble-trapping region in the near wake behind the cylinder was observed at $Re = 2,463$. Even though the void fraction ratio was not sufficient to detect the bubble-trapping region at $Re = 1,478$, the shape of the liquid-phase region indicated that the wakes were in transition to induce the bubble-trapping region. As expected, at a low Reynolds number of $Re = 493$, there was no bubble-trapping region due to low inertial and lift forces.

The force balance analysis revealed that the transitional behavior of the bubble-trapping region is related to the lift force acting on the bubbles. In the previous literature reviewed in Chapter 1.3, the inertial force seemed to be the only bubble-trapping force that caused the bubble accumulation in a two-phase crossflow. With the current investigation at a range of transitional Reynolds numbers from $Re = 493$ to $Re = 2,463$, it was discovered that the lift force acting on bubbles was equally important in explaining the bubble-trapping phenomenon. While the inertial forces were significant for both the horizontal and vertical movement of bubbles, the lift force was important in the horizontal direction. In addition, the peak location of the forces differed based on the direction of the force. Analysis of both the inertial and lift forces are needed to explain the bubble-trapping phenomenon.

The transient analysis of the liquid velocities of the single-phase or two-phase crossflows revealed that the oscillatory behavior of wakes around the cylinder did not bias the time-averaged results and the force balance analysis. With the injection of air bubbles, the transient analysis revealed that the mean liquid velocities and the fluctuating liquid velocities increased in both

horizontal and vertical directions. The bubble-trapping phenomenon could have triggered more significant mixing and momentum transfer in the wakes around the cylinder.

5. Conclusions and Recommendations

This experimental research investigated two-phase wakes generated from an upward liquid-gas flow around a cylinder. This investigation started with an interest in the wakes generated from a two-phase heat exchanger and their influence on heat transfer performance. As commonly used in pin-fin heat exchangers, a circular cylinder configuration was chosen for the experiment. The experimental facility was designed to conduct flow visualization with a high-speed camera and track air bubbles and liquid flows. By illuminating the water channel from the back, the high-speed camera could capture the shape of the air bubbles. In addition, the camera could capture the movement of liquid flow by injecting the neutrally-buoyant flow tracers. With the rigorous imaging process algorithm, the time-averaged and phase-resolved flow trajectories could be calculated by applying Particle Tracking Velocimetry, Particle Image Velocimetry, and Particle Shadow Image Velocimetry.

Firstly, the two-phase wakes were characterized by time-averaged patterns of void distribution. The void fraction measurements from the set of images could determine the local augmentation or decrement of void concentration behind the cylinder. The results from the time-averaged images revealed that the two-phase wakes consisted of a liquid-phase region and a bubble-trapping region. The liquid-phase region was located right behind the cylinder, where the time-averaged void fraction was small compared to the freestream void fraction. The liquid-phase region was observed throughout the range of experimental conditions. However, their length decreased significantly as the Reynolds number increased. Unlike the liquid-phase region, the bubble-trapping region, where the local time-averaged void fraction was much greater than its freestream void fraction, was only observed at a certain flow condition. Usually, the bubble-trapping region occurred when the Reynolds number based on a cylinder diameter was greater than 2,000.

Secondly, the time-averaged force balance was developed to explain the occurrence of the bubble-trapping region. The force balance equation, derived from understanding the forces acting on the bubbles, consisted of buoyancy, drag, added-mass, pressure-gradient, and lift forces. For solving the equation, it needed phase-resolved velocities and bubble diameter information. The image processing algorithms allowed the calculation of the needed values: liquid velocities, bubble velocities, and bubble diameters. The force balance model revealed that the bubble-trapping region occurred when the added-mass, pressure-gradient, and lift forces were strong. The current model concluded that the lift force, in addition to the already-identified inertial force, is important in explaining the bubble-trapping region. A bubble trapping parameter was determined by simplifying the force balance model, which allows the prediction of the occurrence of bubble trapping based on the bubble size compared to the cylinder size in addition to the flow velocity.

In addition, further investigation of the bubble-trapping region discovered that the bubble-trapping forces act in two stages. Near the cylinder, there were areas of strong inward horizontal forces acting on the air bubbles around the cylinder. Further downstream, away from the center of the cylinder, there were areas of strong downward forces that acted on the air bubbles. In many cases, the inertial and lift forces were equally important when the bubble-trapping occurred. However, the inertial forces had stronger effects on the area of the strong downward forces. This explained why the bubble-trapping occurred at a transitional range of Reynolds number when the inertial force itself was not strong, but the combined forces were strong enough to accumulate the bubbles in the cylinder wake.

This research on the bubble-trapping region of two-phase wakes around a cylinder highlights the importance of the added-mass, pressure-gradient, and lift forces on the trapping phenomenon. The force balance model and the trapping parameter developed also explain why the bubbles are attracted towards the centerline and held at the wakes momentarily. However, future improvements can be made from the experimental effort. The current research was

restricted to two distinct ranges of bubble diameters, mainly in bubble mean diameter of 3.0 – 3.5 mm or 0.5 – 0.6 mm, and one diameter of a circular cylinder (9.5 mm). The force balance model and the trapping parameter should be verified at an intermediate mean bubble diameter, *e.g.*, 1 mm, and a fine mean bubble diameter, *e.g.*, 0.1-0.3 mm. In addition, it is recommended to conduct investigations with various cylinder diameters, *e.g.*, 20 mm. These variations will provide a better understanding of the bubble-trapping forces at various experimental conditions and improve the current model. Also, these configurations are closer to the tube diameters used in the two-phase heat exchangers and the bubble diameters generated from the subcooled boiling flow. These variations will enlighten the effects of relative bubble size on a cylinder diameter which were not discussed in the current model.

In addition, the present investigation occurred from a relatively macroscopic viewpoint. The high-speed images were processed to calculate the time-averaged velocities for the two phases while ignoring individual bubble movement variations. The current model lacks the ability to analyze an individual bubble movement; however, the time-averaged force balance equation could explain the overall cause of the bubble-trapping region. Also, the camera had a relatively large field of view which restricted the resolution of the velocity fields. The force balance analysis revealed the areas where the peak bubble-trapping forces exist. Adjustment in camera location and magnification can improve the velocity field resolution and provide more detailed movement of air bubbles in the wakes around the cylinder. In the current report, the wall lubrication force is neglected partly due to the limitations on the image magnification. Bubble coalescence or breakup rarely happened during the experiments; the interaction among the air bubbles in the wakes may have influenced the occurrence of the bubble-trapping region. By limiting the field of view near the wall, the lubrication force can be calculated; then, its influence on the formation of the liquid-phase region could be explained. In addition, the current outcome assumes the bubbly flow with a low void fraction. As the higher amount of bubble concentration

would increase the frequency of the bubble interaction, the lubrication force and other aspects, such as bubble coalescence, breakage rates, and bubble-induced turbulence, may not be neglected.

Another improvement that can be made is a more accurate void fraction measurement. The void fraction was calculated from the correlation of the shadow fraction measurement. Due to the uncertainties of experimental measurement, the actual void fraction values could be different from the void fraction calculation. Instead, direct measurement of the local void fraction is possible by installing conductance probes or optical fiber probes. Also, it could provide the ability to further investigate the effects of void fraction and air superficial velocities. As the void fraction and air superficial velocities increase, the two-phase flow characteristics may change, which may result in different behavior in the liquid-phase and bubble-trapping regions.

Lastly, it could be interesting if the characteristics of two-phase wakes could be observed on a two-phase heat exchanger design. The effects of active heat transfer and heat exchanger geometry may alter the bubble-trapping behavior. Unlike the adiabatic two-phase crossflow, where the air bubbles were already mixed with the liquid flow, the vapor bubbles would be generated from the surface of a heat exchanger structure. In this case, the bubble formation and departure processes need to be considered where surface tension, buoyancy, and drag forces take essential roles. The critical condition for bubble departure would be when the buoyancy and drag forces are more significant than the surface tension. Even though the current force balance analysis on the bubble-trapping behavior does not emphasize its importance, the effects of the buoyancy force need to be included. The bubble injection or nucleation on the bluff body surface would alter the bubble dynamics in the wakes and the behavior of the bubble-trapping phenomenon. Further investigations of the liquid-gas crossflow are recommended by replacing the circular cylinder in the water channel facility with a cylinder with bubble injection holes or a

cylindrical sparger to improve the current analysis and clarify the importance of the buoyancy force.

Bibliography

- [1] Kandlikar, S. G., 1990, "A General Correlation for Saturated Two-Phase Flow Boiling Heat Transfer Inside Horizontal and Vertical Tubes," *J. Heat Transfer*, **112**(1), pp. 219–228.
- [2] Zhang, W., Hibiki, T., and Mishima, K., 2004, "Correlation for Flow Boiling Heat Transfer in Mini-Channels," *Int. J. Heat Mass Transf.*, **47**(26), pp. 5749–5763.
- [3] Bergman, T. L., Incropera, F. P., Lavine, A. S., and DeWitt, D. P., 2011, *Fundamentals of Heat and Mass Transfer*, Wiley.
- [4] Kleinstreuer, C., 2003, *Two-Phase Flow: Theory and Applications*, Taylor & Francis, New York, NY.
- [5] Drew, D. A., 1983, "Mathematical Modeling of Two-Phase Flow," *Annu. Rev. Fluid Mech.*, **15**(1), pp. 261–291.
- [6] Serizawa, A., and Kataoka, I., 1990, "Turbulence Suppression in Bubbly Two-Phase Flow," *Nucl. Eng. Des.*, **122**(1–3), pp. 1–16.
- [7] Ishii, M., and Hibiki, T., 2011, *Thermo-Fluid Dynamics of Two-Phase Flow*, Springer New York, New York, NY.
- [8] Nukiyama, S., 1966, "The Maximum and Minimum Values of the Heat Q Transmitted from Metal to Boiling Water under Atmospheric Pressure," *Int. J. Heat Mass Transf.*, **9**(12), pp. 1419–1433.
- [9] Khushnood, S., Khan, Z. M., Malik, M. A., Koreshi, Z. U., and Khan, M. A., 2004, "A Review of Heat Exchanger Tube Bundle Vibrations in Two-Phase Cross-Flow," *Nucl. Eng. Des.*, **230**(1–3), pp. 233–251.

- [10] Ribatski, G., and Thome, J. R., 2007, "Two-Phase Flow and Heat Transfer across Horizontal Tube Bundles-A Review," *Heat Transf. Eng.*, **28**(6), pp. 508–524.
- [11] Thome, J. R., 2004, "Boiling in Microchannels: A Review of Experiment and Theory," *Int. J. Heat Fluid Flow*, **25**(2), pp. 128–139.
- [12] Wambsganss, M. ., Jendrzeczyk, J. ., and France, D. ., 1991, "Two-Phase Flow Patterns and Transitions in a Small, Horizontal, Rectangular Channel," *Int. J. Multiph. Flow*, **17**(3), pp. 327–342.
- [13] Guo, D., Wei, J. J., and Zhang, Y. H., 2011, "Enhanced Flow Boiling Heat Transfer with Jet Impingement on Micro-Pin-Finned Surfaces," *Appl. Therm. Eng.*, **31**(11–12), pp. 2042–2051.
- [14] Qiu, L., Dubey, S., Choo, F. H., and Duan, F., 2015, "Recent Developments of Jet Impingement Nucleate Boiling," *Int. J. Heat Mass Transf.*, **89**, pp. 42–58.
- [15] Rau, M. J., Garimella, S. V., Dede, E. M., and Joshi, S. N., 2015, "Boiling Heat Transfer From an Array of Round Jets With Hybrid Surface Enhancements," *J. Heat Transfer*, **137**(7).
- [16] Shah, R. K., and Sekulic, D. P., 2003, *Fundamentals of Heat Exchanger Design*, John Wiley & Sons, Nashville, TN.
- [17] Coutanceau, M., and Defaye, J.-R., 1991, "Circular Cylinder Wake Configurations: A Flow Visualization Survey," *Appl. Mech. Rev.*, **44**(6), pp. 255–305.
- [18] Blevins, R. D., 2001, *Flow-Induced Vibration*, Krieger Publishing Company, Malaba, FL.
- [19] Zdravkovich, M. M., 1997, *Flow Around Circular Cylinders Volume 1: Fundamentals*, Oxford University Press, Oxford.

- [20] Cimbala, J. M., Nagib, H. M., and Roshko, A., 1988, "Large Structure in the Far Wakes of Two-Dimensional Bluff Bodies," *J. Fluid Mech.*, **190**(1988), pp. 265–298.
- [21] Roshko, A., 1961, "Experiments on the Flow Past a Circular Cylinder at Very High Reynolds Number," *J. Fluid Mech.*, **10**(3), pp. 345–356.
- [22] Lin, J.-C., Towfighi, J., and Rockwell, D., 1995, "Instantaneous Structure of the Near-Wake of a Circular Cylinder: On the Effect of Reynolds Number," *J. Fluids Struct.*, **9**(4), pp. 409–418.
- [23] Norberg, C., 1993, "Pressure Forces on a Circular Cylinder in Cross Flow," *Bluff-Body Wakes, Dynamics and Instabilities*, Springer Berlin Heidelberg, Berlin, Heidelberg, pp. 275–278.
- [24] Prasad, A., and Williamson, C. H. K., 1997, "Three-Dimensional Effects in Turbulent Bluff-Body Wakes," *J. Fluid Mech.*, **343**, pp. 235–265.
- [25] Nakamura, H., and Igarashi, T., 2004, "Unsteady Heat Transfer from a Circular Cylinder for Reynolds Numbers from 3000 to 15,000," *Int. J. Heat Fluid Flow*, **25**(5), pp. 741–748.
- [26] Scholten, J. W., and Murray, D. B., 1998, "Unsteady Heat Transfer and Velocity of a Cylinder in Cross Flow—I. Low Freestream Turbulence," *Int. J. Heat Mass Transf.*, **41**(10), pp. 1139–1148.
- [27] Norberg, C., 1994, "An Experimental Investigation of the Flow around a Circular Cylinder: Influence of Aspect Ratio," *J. Fluid Mech.*, **258**, pp. 287–316.
- [28] Ma, X., Karamanos, G. S., and Karniadakis, G. E., 2000, "Dynamics and Low-Dimensionality of a Turbulent near Wake," *J. Fluid Mech.*, **410**, pp. 29–65.

- [29] Inoue, A., Kozawa, Y., Yokosawa, M., and Aoki, S., 1986, "Studies on Two-Phase Cross Flow. Part I: Flow Characteristics around a Cylinder," *Int. J. Multiph. Flow*, **12**(2), pp. 149–167.
- [30] Magnaudet, J., and Eames, I., 2000, "The Motion of High-Reynolds-Number Bubbles in Inhomogeneous Flows," *Annu. Rev. Fluid Mech.*, **32**(1), pp. 659–708.
- [31] Salibindla, A. K. R., Masuk, A. U. M., Tan, S., and Ni, R., 2020, "Lift and Drag Coefficients of Deformable Bubbles in Intense Turbulence Determined from Bubble Rise Velocity," *J. Fluid Mech.*, **894**, p. A20.
- [32] Milenković, R. Ž., Sigg, B., and Yadigaroglu, G., 2007, "Bubble Clustering and Trapping in Large Vortices. Part 2: Time-Dependent Trapping Conditions," *Int. J. Multiph. Flow*, **33**(10), pp. 1111–1125.
- [33] Sugiyama, K., Takagi, S., and Matsumoto, Y., 2001, "Three-Dimensional Numerical Analysis of Bubbly Flow around a Circular Cylinder.," *JSME Int. J. Ser. B*, **44**(3), pp. 319–327.
- [34] Lee, J., and Park, H., 2020, "Bubble Dynamics and Bubble-Induced Agitation in the Homogeneous Bubble-Swarm Past a Circular Cylinder at Small to Moderate Void Fractions," *Phys. Rev. Fluids*, **5**(5), p. 54304.
- [35] Yokosawa, M., Kozawa, Y., Inoue, A., and Aoki, S., 1986, "Studies on Two-Phase Cross Flow. Part II: Transition Reynolds Number and Drag Coefficient," *Int. J. Multiph. Flow*, **12**(2), pp. 169–184.
- [36] Yokosawa, M., Kozawa, Y., Inoue, A., and Aoki, S., 1986, "Studies on Two-Phase Cross Flow. Part III: Characteristics of Unsteady Flow Behavior," *Int. J. Multiph. Flow*, **12**(2), pp. 185–202.
- [37] Hulin, J. P., Fierfort, C., and Coudol, R., 1982, "Experimental Study of Vortex Emission behind Bluff Obstacles in a Gas Liquid Vertical Two-Phase Flow," *Int. J. Multiph. Flow*, **8**(5), pp. 475–490.

- [38] Joo, Y., and Dhir, V. K., 1994, "An Experimental Study of Drag on a Single Tube and on a Tube in an Array under Two-Phase Cross Flow," *Int. J. Multiph. Flow*, **20**(6), pp. 1009–1019.
- [39] Kim, N., Kim, H., and Park, H., 2015, "An Experimental Study on the Effects of Rough Hydrophobic Surfaces on the Flow around a Circular Cylinder," *Phys. Fluids*, **27**(8), p. 085113.
- [40] Stewart, C. W., and Crowe, C. T., 1993, "Bubble Dispersion in Free Shear Flows," *Int. J. Multiph. Flow*, **19**(3), pp. 501–507.
- [41] Balachandar, S., and Eaton, J. K., 2010, "Turbulent Dispersed Multiphase Flow," *Annu. Rev. Fluid Mech.*, **42**(1), pp. 111–133.
- [42] Homann, H., and Bec, J., 2015, "Concentrations of Inertial Particles in the Turbulent Wake of an Immobile Sphere," *Phys. Fluids*, **27**(5), p. 053301.
- [43] Sato, S., Vincent, J. H., and Pui, D. Y. P., 1996, "Dispersion of Large Particles in the near Wake of a Disc in a Turbulent Free Stream," *J. Aerosol Sci.*, **27**(4), pp. 559–573.
- [44] Lance, M., and Bataille, J., 1991, "Turbulence in the Liquid Phase of a Uniform Bubbly Air–Water Flow," *J. Fluid Mech.*, **222**(1), p. 95.
- [45] Druzhinin, O. A., and Elghobashi, S., 1998, "Direct Numerical Simulations of Bubble-Laden Turbulent Flows Using the Two-Fluid Formulation," *Phys. Fluids*, **10**(3), pp. 685–697.
- [46] Aliseda, A., and Lasheras, J. C., 2011, "Preferential Concentration and Rise Velocity Reduction of Bubbles Immersed in a Homogeneous and Isotropic Turbulent Flow," *Phys. Fluids*, **23**(9), p. 093301.

- [47] Tio, K.-K., Liñán, A., Lasheras, J. C., and Gañán-Calvo, A. M., 1993, “On the Dynamics of Buoyant and Heavy Particles in a Periodic Stuart Vortex Flow,” *J. Fluid Mech.*, **254**, pp. 671–699.
- [48] Wang, L.-P., and Maxey, M. R., 1993, “The Motion of Microbubbles in a Forced Isotropic and Homogeneous Turbulence,” *Appl. Sci. Res.*, **51**(1–2), pp. 291–296.
- [49] Sene, K. J., Hunt, J. C. R., and Thomas, N. H., 1994, “The Role of Coherent Structures in Bubble Transport by Turbulent Shear Flows,” *J. Fluid Mech.*, **259**, pp. 219–240.
- [50] Auton, T. R., 1983, “The Dynamics of Bubbles, Drops and Particles in Motion in Liquid,” University of Cambridge.
- [51] Auton, T. R., Hunt, J. C. R., and Prud’Homme, M., 1988, “The Force Exerted on a Body in Inviscid Unsteady Non-Uniform Rotational Flow,” *J. Fluid Mech.*, **197**, pp. 241–257.
- [52] Kim, D., and Rau, M. J., 2020, “Two-Phase Wakes in Adiabatic Liquid-Gas Flow Around a Cylinder,” *Volume 2: Fluid Mechanics; Multiphase Flows*, American Society of Mechanical Engineers.
- [53] Kim, D., and Rau, M. J., 2022, “Characterization of Two-Phase Wakes in an Upward Adiabatic Liquid-Gas Flow around a Cylinder,” *Manuscr. Prep.*
- [54] Cheong, W. J., and Carr, P. W., 1987, “The Surface Tension of Mixtures of Methanol, Acetonitrile, Tetrahydrofuran, Isopropanol, Tertiary Butanol and Dimethyl-Sulfoxide with Water at 25°C,” *J. Liq. Chromatogr.*, **10**(4), pp. 561–581.
- [55] Pettigrew, M. J., Zhang, C., Mureithi, N. W., and Pamfil, D., 2005, “Detailed Flow and Force Measurements in a Rotated Triangular Tube Bundle Subjected to Two-Phase Cross-Flow,” *J. Fluids Struct.*, **20**(4), pp. 567–575.

- [56] Situ, R., Hibiki, T., Ishii, M., and Mori, M., 2005, "Bubble Lift-off Size in Forced Convective Subcooled Boiling Flow," *Int. J. Heat Mass Transf.*, **48**(25–26), pp. 5536–5548.
- [57] Murai, Y., Sasaki, T., Ishikawa, M. A., and Yamamoto, F., 2005, "Bubble-Driven Convection around Cylinders Confined in a Channel," *J. Fluids Eng. Trans. ASME*, **127**(1), pp. 117–123.
- [58] Murai, Y., Matsumoto, Y., and Yamamoto, F., 2001, "Three-Dimensional Measurement of Void Fraction in a Bubble Plume Using Statistic Stereoscopic Image Processing," *Exp. Fluids*, **30**(1), pp. 11–21.
- [59] Belden, J., Ravela, S., Truscott, T. T., and Techet, A. H., 2012, "Three-Dimensional Bubble Field Resolution Using Synthetic Aperture Imaging: Application to a Plunging Jet," *Exp. Fluids*, **53**(3), pp. 839–861.
- [60] Kitagawa, A., Sugiyama, K., and Murai, Y., 2004, "Experimental Detection of Bubble–Bubble Interactions in a Wall-Sliding Bubble Swarm," *Int. J. Multiph. Flow*, **30**(10), pp. 1213–1234.
- [61] Otsu, N., 1979, "A Threshold Selection Method from Gray-Level Histograms," *IEEE Trans. Syst. Man. Cybern.*, **9**(1), pp. 62–66.
- [62] Kim, D., and Rau, M. J., 2022, "A Phase-Resolved Force Analysis of Bubble Trapping behind Cylinders in Liquid-Gas Flows," *Manuscr. Prep.*
- [63] Lau, Y. M., Deen, N. G., and Kuipers, J. A. M., 2013, "Development of an Image Measurement Technique for Size Distribution in Dense Bubbly Flows," *Chem. Eng. Sci.*, **94**, pp. 20–29.
- [64] Meyer, F., 1994, "Topographic Distance and Watershed Lines," *Signal Processing*, **38**(1), pp. 113–125.

- [65] Soille, P., 2004, *Morphological Image Analysis*, Springer Berlin Heidelberg, Berlin, Heidelberg.
- [66] Vlachos, P. P., 2015, "PRANA PIV/PTV Codes" [Online]. Available: <https://github.com/pvlachos/prana>.
- [67] Cardwell, N. D., Vlachos, P. P., and Thole, K. A., 2011, "A Multi-Parametric Particle-Pairing Algorithm for Particle Tracking in Single and Multiphase Flows," *Meas. Sci. Technol.*, **22**(10), p. 105406.
- [68] Westerweel, J., Dabiri, D., and Gharib, M., 1997, "The Effect of a Discrete Window Offset on the Accuracy of Cross-Correlation Analysis of Digital PIV Recordings," *Exp. Fluids*, **23**(1), pp. 20–28.
- [69] Meinhart, C. D., Wereley, S. T., and Santiago, J. G., 2000, "A PIV Algorithm for Estimating Time-Averaged Velocity Fields," *J. Fluids Eng.*, **122**(2), pp. 285–289.
- [70] Estevadeordal, J., and Goss, L., 2005, "PIV with LED: Particle Shadow Velocimetry (PSV) Technique," *43rd AIAA Aerospace Sciences Meeting and Exhibit*, American Institute of Aeronautics and Astronautics, Reston, Virginia.
- [71] Khodaparast, S., Borhani, N., Tagliabue, G., and Thome, J. R., 2013, "A Micro Particle Shadow Velocimetry (MPSV) Technique to Measure Flows in Microchannels," *Exp. Fluids*, **54**(2), p. 1474.
- [72] Hessenkemper, H., and Ziegenhein, T., 2018, "Particle Shadow Velocimetry (PSV) in Bubbly Flows," *Int. J. Multiph. Flow*, **106**, pp. 268–279.
- [73] Estevadeordal, J., and Goss, L., 2005, "An Investigation Of Particle-Shadow Velocimetry (PSV) For Transonic-Flow Applications," *35th AIAA Fluid Dynamics Conference and Exhibit*, American Institute of Aeronautics and Astronautics, Reston, Virginia.

- [74] Deen, N. G., Westerweel, J., and Delnoij, E., 2002, “Two-Phase PIV in Bubbly Flows: Status and Trends,” *Chem. Eng. Technol.*, **25**(1), p. 97.
- [75] Keyvani, A., and Strom, K., 2013, “A Fully-Automated Image Processing Technique to Improve Measurement of Suspended Particles and Floccs by Removing out-of-Focus Objects,” *Comput. Geosci.*, **52**, pp. 189–198.
- [76] Milenković, R. Ž., Sigg, B., and Yadigaroglu, G., 2007, “Bubble Clustering and Trapping in Large Vortices. Part 1: Triggered Bubbly Jets Investigated by Phase-Averaging,” *Int. J. Multiph. Flow*, **33**(10), pp. 1088–1110.
- [77] Sridhar, G., and Katz, J., 1995, “Drag and Lift Forces on Microscopic Bubbles Entrained by a Vortex,” *Phys. Fluids*, **7**(2), pp. 389–399.
- [78] Clift, R., Grace, J. R., and Weber, M. E., 1978, *Bubbles, Drops, and Particles*, Academic Press.
- [79] Maxey, M. R., 1983, “Equation of Motion for a Small Rigid Sphere in a Nonuniform Flow,” *Phys. Fluids*, **26**(4), p. 883.
- [80] Yan, X., Jia, Y., Wang, L., and Cao, Y., 2017, “Drag Coefficient Fluctuation Prediction of a Single Bubble Rising in Water,” *Chem. Eng. J.*, **316**, pp. 553–562.
- [81] Chen, W., and Zhang, L., 2021, “Effects of Interphase Forces on Multiphase Flow and Bubble Distribution in Continuous Casting Strands,” *Metall. Mater. Trans. B*, **52**(1), pp. 528–547.
- [82] Lubchenko, N., Magolan, B., Sugrue, R., and Baglietto, E., 2018, “A More Fundamental Wall Lubrication Force from Turbulent Dispersion Regularization for Multiphase CFD Applications,” *Int. J. Multiph. Flow*, **98**, pp. 36–44.

- [83] Yan, P., Jin, H., He, G., Guo, X., Ma, L., Yang, S., and Zhang, R., 2019, “CFD Simulation of Hydrodynamics in a High-Pressure Bubble Column Using Three Optimized Drag Models of Bubble Swarm,” *Chem. Eng. Sci.*, **199**, pp. 137–155.
- [84] Antal, S. P., Lahey, R. T., and Flaherty, J. E., 1991, “Analysis of Phase Distribution in Fully Developed Laminar Bubbly Two-Phase Flow,” *Int. J. Multiph. Flow*, **17**(5), pp. 635–652.
- [85] Khan, I., Wang, M., Zhang, Y., Tian, W., Su, G., and Qiu, S., 2020, “Two-Phase Bubbly Flow Simulation Using CFD Method: A Review of Models for Interfacial Forces,” *Prog. Nucl. Energy*, **125**, p. 103360.
- [86] Alfonsi, G., 2009, “Reynolds-Averaged Navier–Stokes Equations for Turbulence Modeling,” *Appl. Mech. Rev.*, **62**(4).
- [87] Kim, D., and Rau, M., 2022, “High-Speed Visualization of Bubble Trapping Wakes in Liquid-Gas Flow Around a Cylinder,” *J. Fluids Eng.*, **144**(4).

VITA

Dohwan Kim was born in Changwon, South Korea. He attended the University of California, San Diego, and earned a Bachelor of Science in Mechanical Engineering with a *cum laude* honor in 2017. During his undergraduate program, he served as an undergraduate project advisor for Global TIES of UC San Diego in 2016 and 2017.

Upon the completion of his undergraduate study, he pursued a Doctor of Philosophy in Mechanical Engineering at the Pennsylvania State University. During his Ph.D. program, he studied experimental two-phase flow mechanics and heat transfer. He also earned ASME Fluids Engineering Division Graduate Student Scholarship in 2020 and 2021. He completed his doctoral program in December 2022.